PHOTO-ACTIVE AND REDOX-ACTIVE METAL-ORGANIC FRAMEWORKS FOR SOLAR ENERGY UTILIZATION

Caleb A. Kent

A dissertation submitted to the faculty of the University of North Carolina at Chapel Hill in partial fulfillment of the requirements for the degree of Doctor of Philosophy in the Department of Chemistry.

Chapel Hill
2012

Approved by:

Dr. Wenbin Lin

Dr. Thomas J. Meyer

Dr. John M. Papanikolas

Dr. Cynthia K. Schauer

Dr. Wei You

ABSTRACT

CALEB A. KENT: Photo-Active and Redox-Active Metal-Organic Frameworks for Solar Energy Utilization
(Under the direction of Wenbin Lin and Thomas J. Meyer)

Isomorphous metal-organic frameworks (MOFs) based on photo-active Ru(II) or Os(II) polypyridal complex building blocks with characteristic strong visible light absorption, and long-lived, high-energy excited states were designed and synthesized to study the classic Ru to Os energy transfer process for applications in light-harvesting with supramolecular assemblies. The crystalline nature of MOFs allows for determination of the distances between metal centers by X-ray diffraction. The Os doping level was systematically varied to experimentally determine relative rates of energy migration.

Several structures demonstrated rapid excited state energy transfer and nano/microscale MOFs were synthesized for light harvesting experiments. Suspensions of the particles were quenched by both oxidative and reductive electron transfer reagents at the crystal-solution interface. In a remarkable case, greater than 98% steady-state emission quenching is observed by energy migration over hundreds of nanometers and interfacial electron-transfer. A quantitative Stern-Volmer analysis was developed to distinguish between static and dynamic quenching mechanisms and determine the rates of electron transfer.

The light harvesting characteristics of the MOFs allow them to be utilized as highly responsive sensors by an amplified quenching mechanism with the highest triplet excited state amplification in the literature. Strong noncovalent interactions between the MOF

microcrystal surface and cationic quencher molecules coupled with rapid energy transfer through the MOF microcrystal facilitates amplified quenching with an enhancement of 7000-fold in the Stern-Völmer quenching constant compared to a model complex.

Additional work has investigated a surprising ligand based singlet-triplet equilibrium in the stable complex $[Ru(bpy)_2(phendione)]^{2+}$. A singlet ground state is observed in low temperature SQUID experiments while a thermally populated triplet is observable at room temperature in acetonitrile as confirmed by variable temperature NMR and EPR experiments. DFT calculations confirm that the lowest energy triplet is ligand based and the energy gap can be tuned by substituent effects of the bpy ligands.

Incorporation of photo-active Ru polypyridal complexes into MOFs has led to a new class of materials that show promise in light harvesting and amplified quenching. Future work will attempt to exploit the antenna like behavior of these materials for use in photocatalytic systems and by integration into photovoltaic devices.

DEDICATION

To my wife for her support and patience during this process. We did this together.

ACKNOWLEDGEMENTS

To my labmates past and present for the interactions that we have had and everything I have learned from you. In particular, Javier Concepcion and Kyle Brennaman have gone well beyond what I could have asked for in helping me over the past 5 years. Thank you.

To my advisors who have enabled me to perform this research. I am grateful for the significant resources you have trusted to me and how you have challenged me to think creatively while being scientifically rigorous. Thank you for creating an environment that has made it possible for me to excel.

TABLE OF CONTENTS

Page

LIST OF TABLES

LIST OF FIGURES

LIST OF ABBREVIATIONS AND SYMBOLS

1	[(**L1**$_{\mathbf{Ru}}$)Zn]•2DMF•4H_2O
2	[(**L2**$_{\mathbf{Ru}}$-H_2)Zn]•3H_2O
3	[(**L3**$_{\mathbf{Ru}}$)$_2Zn_5$•(μ-OH)•(HCO_2)•DMF•2H_2O]•6H_2O
1-Os	[(**L1**$_{\mathbf{Os}}$)Zn]•2DMF•4H_2O
2-Os	[(**L2**$_{\mathbf{Os}}$-H_2)Zn]•3H_2O
3-Os	[(**L3**$_{\mathbf{Os}}$)$_2Zn_5$•(μ-OH)•(HCO_2)•DMF•2H_2O]•6H_2O
4a	[(**L4**$_{\mathbf{Ru}}$)$_2$NaAl(oxalate)$_3$]
4a-Os	[(**L4**$_{\mathbf{Os}}$)$_2$NaAl(oxalate)$_3$]
4b	[(**L4**$_{\mathbf{Ru}}$)$_2Zn_2$(oxalate)$_3$]
4b-Os	[(**L4**$_{\mathbf{Os}}$)$_2Zn_2$(oxalate)$_3$]
a.u.	arbitrary units
bpy	2,2’-bipyridine
BQ	1,4-benzoquinone
ca.	calculated
d	doublet
deeb	4,4’-COOEtbpy
DEF	diethylformamide
DI	deionized water
dmb	4,4’-dimethylbpy
DMF	dimethylformamide
DMSO	dimethyl sulfoxide
EtOH	ethanol

ICP	inductively coupled plasma
Ka	association constant
Kd	dynamic quenching rate constant
Ks	static quenching rate constant
$L1_{Os}$	$[Os(4,4'\text{-}CO_2H\text{-}bpy)_2bpy](PF_6)_2$
$L1_{Ru}$	$[Ru(4,4'\text{-}CO_2H\text{-}bpy)_2bpy](PF_6)_2$
$L2_{Os}$	$Os(4,4'\text{-}CO_2H\text{-}bpy)_2CN_2$
$L2_{Ru}$	$Ru(4,4'\text{-}CO_2H\text{-}bpy)_2CN_2$
$L3_{Os}$	$Os(5,5'\text{-}CO_2H\text{-}bpy)_2CN_2$
$L3_{Ru}$	$Ru(5,5'\text{-}CO_2H\text{-}bpy)_2CN_2$
$L4_{Os}$	$[Os(bpy)_3](PF_6)_2$
$L4_{Ru}$	$[Ru(bpy)_3](PF_6)_2$
m	multiplet
MeCN	acetonitrile
MeOH	methanol
MLCT	metal to ligand charge transfer
MOFs	metal-organic frameworks
MS	mass spectrometry
NMR	nuclear magnetic resonance
OES	optical emission spectrometry
pd	1,10-phenanthroline-5,6-dione
PXRD	powder x-ray diffraction
s	singlet

SEM	scanning electron microscope
t	triplet
TBAH	tetrabutylammonium hexafluorophosphate
TGA	thermogravimetric analysis
THAH	tetrahexylammonium hexafluorophosphate
TMAH	tetramethylammonium hexafluorophosphate
tmb	4,4’,5,5’-tetramethylbpy
TMBD	N,N,N’,N’ tetramethylbenzidine
v/v	volume to volume ratio
XRD	x-ray diffraction
γ	fraction of excited states to reach the MOF surface
τ	lifetime

CHAPTER 1

SYNTHESIS AND CHARACTERIZATION OF PHOTO-ACTIVE AND REDOX-ACTIVE METAL-ORGANIC FRAMEWORKS

1.1 Light Harvesting for Solar Fuels

Chemists have long been interested in developing artificial photosynthetic systems for harvesting and converting sunlight into chemical energy.[1-7] Photosynthesis integrates peripheral, but highly efficient, membrane-bound antenna systems with reaction centers where high yield light-to-redox equivalent conversion is utilized to drive chemical reactions,[8, 9] notably water oxidation in Photosystem II[10] and CO_2 reduction in Photosystem I.[11] The light-harvesting antenna of an artificial photosynthetic device must efficiently collect diffuse sunlight and transport the energy to catalytic centers for solar fuels production. The pigment-protein complexes in nature set a high standard by delivering energy from greater than 95% of the absorbed photons to the reaction center although the overall photon energy to fuel efficiency is much lower. [12]

An analogous goal in artificial photosynthesis is integration of light absorption and redox catalysis for solar fuels production.[13] Efficient artificial light-harvesting systems have been actively pursued, including dendrimers,[14] supramolecular structures based on porphyrins, phthalocyanines, perylenebisimides, polypyridyl metal complexes,[15] lanthanide coordination polymers,[16] and bridged semiconducting nanoparticles.[17] Self-assembled supramolecular systems are particularly promising because of ease of fabrication and the

ability to control macroscopic order through non-covalent interactions. Promising results have been obtained on efficient harvesting of photons to give high-energy, redox-separated states with efficient redox separation and transport achieved to a limited degree.[5] Energy flow from polypyridyl-based metal-to-ligand charge transfer (MLCT) excited states of Ru(II) to Os(II) has provided a useful probe for understanding energy transfer dynamics in ligand-bridged complexes and hydrogen bonded supramolecular assemblies,[18] functionalized polymers,[19] rigid media,[20, 21] crystalline molecular solids,[22, 23] and across semi-conductor interfaces.[9]

1.2 Photo-Active MOFs

The chemistry of metal-organic frameworks (MOFs) has evolved rapidly in recent years.[24-27] Metal-organic frameworks have recently emerged as a new class of hybrid materials that can be constructed from a variety of functional building blocks.[28-31] Most MOF research has focused on storage and separation of small gaseous molecules by taking advantage of their high microporosities.[32-39] However, numerous recent reports, many of them from the Lin group, have demonstrated that active functional elements can be incorporated into MOFs to create hybrid materials with a range of applications in chemical sensing,[40-43] catalysis,[44-47] biomedical imaging,[48, 49] and drug delivery.[50, 51] Photo-active MOFs have been designed for nonlinear optics,[52] luminescence molecular sensing,[53-55] and bio-imaging.[56] The ability to fine-tune molecular building blocks in MOFs makes them an ideal model system for studying energy transfer dynamics in the ordered solid state. Compared to the energy transfer systems that have been examined earlier, well-defined MOF structures can simplify data analysis, allowing the delineation of structure/property

relationships to provide important insights into optimizing energy migration and transfer efficiency in artificial light-harvesting systems.

We are interested in utilizing MOFs as active structures for light absorption and excited state applications in energy conversion with the ultimate goal of achieving artificial photosynthesis by taking advantage of their ability to absorb light broadly in the visible via metal-to-ligand charge transfer excitations. With their well-defined, repeating structures, functionalized MOFs present an opportunity to design and study dimensionally controlled antenna structures. Importantly, by studying energy transfer dynamics in the isomorphous MOFs with mixed Ru and Os building blocks, we demonstrate the existence of facile inter-site and long-range energy migration in these structurally defined and strongly bonded crystalline solids.

These antenna characteristics can be exploited and coupled to excited state reactivity for efficiently sensitizing interfacial electron transfer and ultimately, photocatalytic redox reactions. Herein we report successful implementation of this strategy and the first examples of oxidative and reductive interfacial electron transfer quenching of MOF microcrystals. We demonstrate that Ru(II)-bpy based MOF microcrystals are highly efficient light-harvesting structures due to their high visible absorptivities, facile intra-crystal site-to-site energy migration to the MOF surface, and efficient electron transfer quenching at the MOF/solution interface. Furthermore, this phenomenon can be exploited in sensing applications when cationic redox quenchers are introduced because of strong non-covalent interactions with the MOF microcrystal surface. Analytes can be detected in the tens of nanomolar concentration range and an amplification factor of up to 7000-fold has been observed compared to a model complex.

1.3 Synthesis and Characterization of Metal Complexes and MOFs

1.3.1 Synthesis and Characterization of Metal Complexes

The metal complexes utilized as building blocks for MOF crystal growth are shown in Figure 1-1. These Ru(II) and Os(II) polypyridal complexes were chosen because their favorable characteristics of low energy visible light absorption, long-lived excited states, and redox active components. In most cases the complexes contain carboxylic acid linking groups for crystal growth. The complexes were linked together through zinc carboxylate bonds to form both 2-dimensional and 3-dimensional MOFs. The cyano functional groups of **L2** and **L3** also served as a linking moiety. The photophysical properties of the self-assembled crystals are largely dictated by the properties of the individual complexes, however the protonation state of the carboxylate groups have a large influence on the emission energy and therefore direct comparisons between solution measurements and within a Zn MOF are not perfect. In general, the emission energy of the MOF is slightly higher than the corresponding protonated complex in solution which is in part a result of the absence of solvent reorganizational energy in the solid-state.

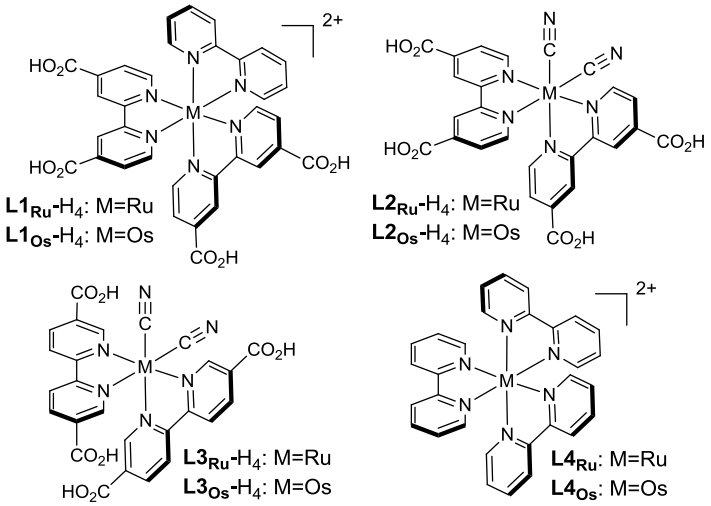

Figure 1-1. Structure of Ru or Os polypyridal complexes incorporated into metal-organic frameworks.

L4 is significantly different than the other building blocks because it does not have any linking functional groups for self-assembly. Instead an anionic framework is formed with oxalate and Zn or with a combination of Na and Al. This anionic framework achieves charge balance by incorporation of the dication **L4** within the pores.

Table 1-1. Absorbance, emission, and lifetime data on Ru complexes and MOFs in degassed solvents at 23°C ± 2°C.

	Absorbance λmax (nm)	Emission λmax (nm)	Lifetime (ns)	Solvent
1	470	635	610	MeCN
[**L1$_{Ru}$-H$_4$**]$(PF_6)_2$)*	477	655	1015	MeOH
2	435	630	1100	MeCN
L2$_{Ru}$-H$_4$[57]	530	733	190	DMF
3	450	655	150	MeCN
L3$_{Ru}$-H$_4$[57]	578	-	<21	DMF
4a NaAl	-	568	1305	EtOH
4b Zn	-	573	760	EtOH
L4$_{Ru}$[58]	451	620	855	MeCN

Table 1-2. Absorbance, emission, and lifetime data on Os complexes and MOFs in degassed solvent at 23°C ± 2°C.

	Absorbance λmax (nm)	Emission λmax (nm)	lifetime (ns)	solvent
1-Os	445	765	15	MeCN
[**L1$_{Os}$-H$_4$**]$(PF_6)_2$)	443	790	41	MeOH
2-Os	450	770	30	MeCN
L2$_{Os}$-H$_4$[59]	500	840	-	MeOH
3-Os	464	774	4	MeCN
4a-Os	-	703	53	EtOH
4b-Os	-	707	50	EtOH
L4$_{Os}$[60]	480	723	20	MeCN

In general, the Ru and Os complexes were synthesized by allowing $M((CO_2Et)_2$-bpy$)_2Cl_2$ to react with 2,2′-bipyridine or KCN followed by acid-catalyzed hydrolysis and anion exchange. A detailed description of the synthetic procedures can be found in section 1.5.1. Brief descriptions of these syntheses are shown below.

$Ru(4,4'\text{-}CO_2Et\text{-}bpy)_2Cl_2$ was prepared by reacting two equivalents of $4,4'\text{-}CO_2Et\text{-}bpy$ with $Ru(cyclo\text{-}octadiene)Cl_2$ polymer in *o*-dichlorobenzene for two hours at 160 ˚C with 89% yield. $Ru(4,4'\text{-}CO_2Et\text{-}bpy)_2Cl_2$ and 1.2 equivalents of bpy were refluxed in H_2O:EtOH (1:1 v/v) for 8 hours to give $[Ru(4,4'\text{-}CO_2Et\text{-}bpy)_2bpy](PF_6)_2$ with a 66% yield. $Os(4,4'\text{-}CO_2Et\text{-}bpy)_2Cl_2$ was synthesized in 76% yield by refluxing $OsCl_6](NH_4)_2$ and two equivalents of $4,4'\text{-}CO_2Et\text{-}bpy$ in ethylene glycol for one hour at 200 ˚C. $[Os(4,4'\text{-}CO_2H\text{-}bpy)_2bpy](PF_6)_2$ ($[\mathbf{L1_{Os}}\text{-}H_4](PF_6)_2$) was synthesized in 45% yield by refluxing $Os(4,4'\text{-}CO_2Et\text{-}bpy)_2Cl_2$ and 1.2 equivalents of bpy in H_2O:EtOH (1:1 v/v) for three days followed by acid hydrolysis.

$Ru(4,4'\text{-}CO_2H\text{-}bpy)_2CN_2$ (**L2**$_{\mathbf{Ru}}$-H_4) Was prepared in 72% yield by refuxing $Ru(4,4'\text{-}CO_2Et\text{-}bpy)_2Cl_2$ with 50 equivalents of KCN in H_2O for 12 hours. $Os(4,4'\text{-}CO_2H\text{-}bpy)_2(CN)_2$ (**L2**$_{\mathbf{Os}}$-H_4) was similarly prepared in 68% yield by refluxing $Os(4,4'\text{-}CO_2Et\text{-}bpy)_2Cl_2$ with 50 equivalents of KCN in H_2O for 12 hours.

$Ru(5,5'\text{-}CO_2Et\text{-}bpy)_2Cl_2$ was prepared by reacting two equivalents of $5,5'\text{-}CO_2Et\text{-}bpy$ with the $Ru(cyclo\text{-}octadiene)Cl_2$ polymer in *o*-dichlorobenzene for one hour at 160 °C with 58% yield. $Ru(5,5'\text{-}CO_2H\text{-}bpy)_2CN_2$ (**L3**$_{\mathbf{Ru}}$-H_4) was synthesized in 68% yield by refluxing $Ru(5,5'\text{-}CO_2Et\text{-}bpy)_2Cl_2$ with 50 equivalents KCN in H_2O for 12 hours. $Os(5,5'\text{-}CO_2Et\text{-}bpy)_2Cl_2$ was synthesized in 77% yield by refluxing $(NH_4)_2[OsCl_6]$ and two equivalents of $5,5'\text{-}CO_2Et\text{-}bpy$ in ethylene glycol for one hour. $Os(5,5'\text{-}CO_2Et\text{-}bpy)_2Cl_2$ was then refluxed with 50 equivalents KCN in H_2O for 12 hours to afford $Os(5,5'\text{-}CO_2H\text{-}bpy)_2CN_2$ (**L3**$_{\mathbf{Os}}$-H_4) in 78% yield.

1.3.2 Synthesis and Characterization of MOFs

All of the MOFs were synthesized under solvothermal conditions. Their syntheses are only briefly described below. The detailed procedures are provided in section 1.5.2.

1.3.2.1 Synthesis and Characterization of MOF-1

[$\mathbf{L1_{Ru}}$Zn]•2DMF•4H_2O, **1,** was prepared by the addition of $\mathbf{L1_{Ru}}$-H_4 and $Zn(NO_3)_2$ in a solvent mixture of DMF and H_2O. Bright red crystals were obtained after heating the mixture at 90˚C for three days at a 30% yield. Os-doped **1** and **1-Os** was prepared in the same manner as described above with a variable amount of added $\mathbf{L1_{Os}}$-H_4 in similar yields.

1 crystallizes in the monoclinic space group $P2_1/c$, with one **L1** ligand, one Zn atom, two DMF and four H_2O molecules in the asymmetric unit. The Zn center adopts a tetrahedral geometry by coordinating to four oxygen atoms of four carboxylate groups of the **L1** ligand, forming a 2D bilayer structure. The distance between the two Ru planes within the bilayer is 10.2 Å, while the distance between Zn planes is 6.8 Å. The resulting 2D layers pack along the *a* axis with the close distance of 4.0 Å between Ru planes of adjacent bilayers.

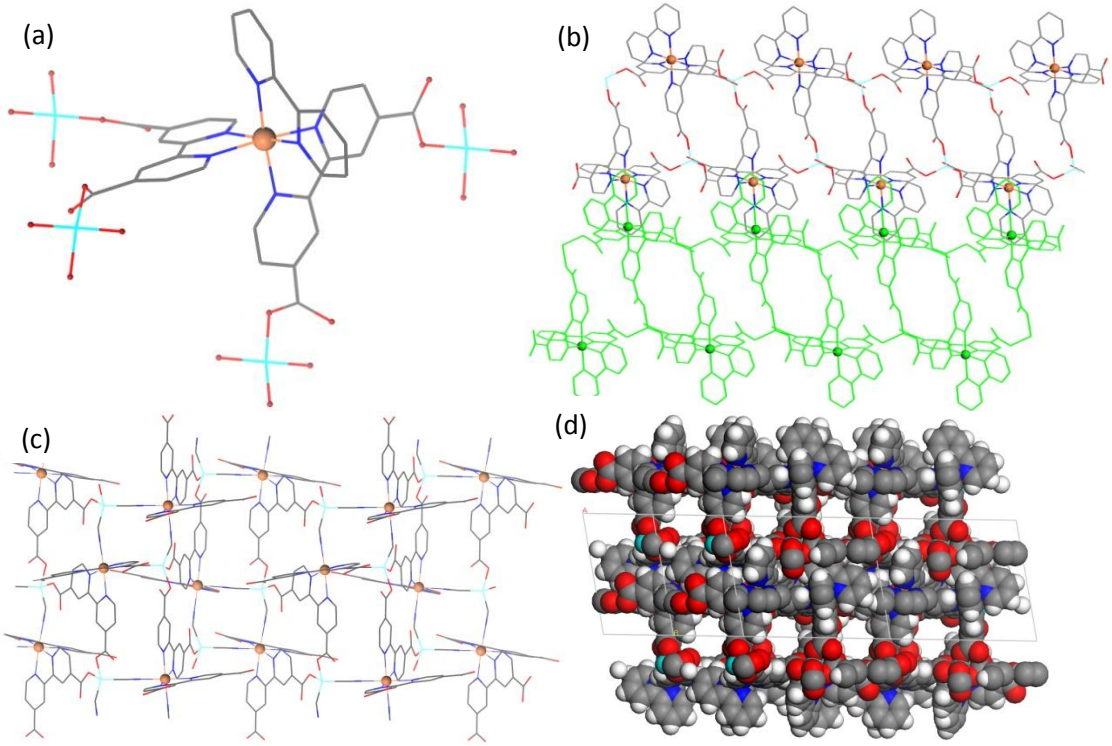

Figure 1-2. Crystal structure of **1**. (a) Wireframe model showing the connectivity of $\mathbf{L1_{Ru}}$ and Zn centers. (b) A side view of a 2D bilayer along the b axis. (c) A top view of the 2D bilayer structure along the a axis. (d) A spacefilling model of 2D bilayers along the b axis.

Table 1-3. Crystallographic data for **1**.

Compound	**1**	**1** (after SQUEEZE)
Empirical formula	$C_{40}H_{20}N_8O_{14}RuZn$	$C_{34}H_{20}N_6O_8RuZn$
Formula weight	1003.08	807.00
Temperature (K)	223	223
Wavelength (Å)	1.54178	1.54178
Crystal system	Monoclinic	Monoclinic
Space group	$P2_1/c$	$P2_1/c$
Unit cell dimensions	a = 14.5979(10) b = 13.6986(11) c = 21.6725(16) β = 103.250(6)	a = 14.5979(10) b = 13.6986(11) c = 21.6725(16) β = 103.250(6)
Volume ($Å^3$)	4218.5(5)	4218.5(5)
Z	4	4
Density (calcd. g/cm^3)	1.579	1.271
Absorption coeff. (mm^{-1})	4.271	4.014
F(000)	2008	1616
Crystal size (mm)	0.12×0.10×0.05	0.12×0.10×0.05
Crystal color & shape	red block	red block
θ range data collection	3.85 – 42.00	3.85 – 42.00
Limiting indices	-12< *h* <12 -8< *k* <11 -15< *l* <18	-12< *h* <12 -8< *k* <11 -15< *l* <18
Reflections collected	6720	6720
Independent reflections	2574[R_{int} =0.0515]	2754 [R_{int}= 0.0520]
Refinement method	Full-matrix least-square on F^2	Full-matrix least-square on F^2
Data/restraints/parameters	2754/37/550	2754/439/441
Goodness-of-fit on F^2	1.083	1.085
Final R indices [$I>2\sigma(I)$][a,b]	R1 = 0.0802 wR2 = 0.2164	R1 = 0.0624 wR2 = 0.1558
R indices (all data)	R1 = 0.1074 wR2 = 0.2401	R1 = 0.0813 wR2 = 0.1634

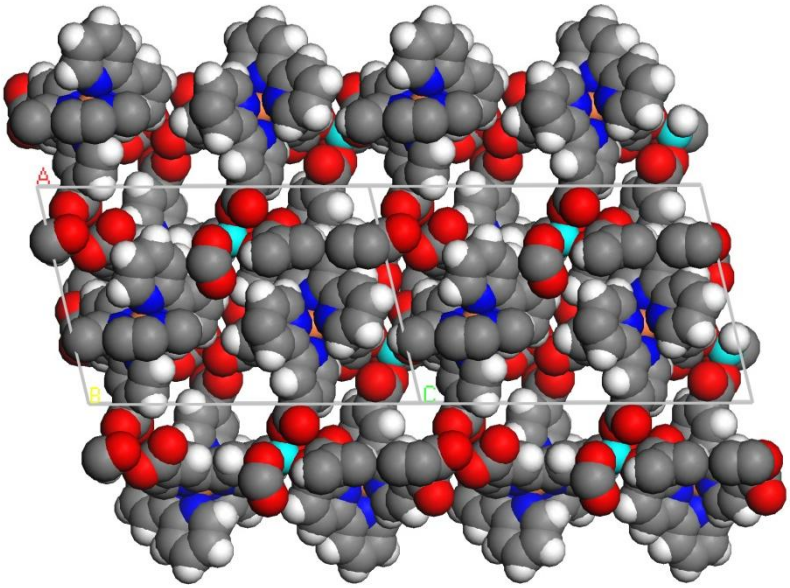

Figure 1-3. Space-filling model of **1** as viewed along the *b* axis. The solvent molecules were removed for clarity.

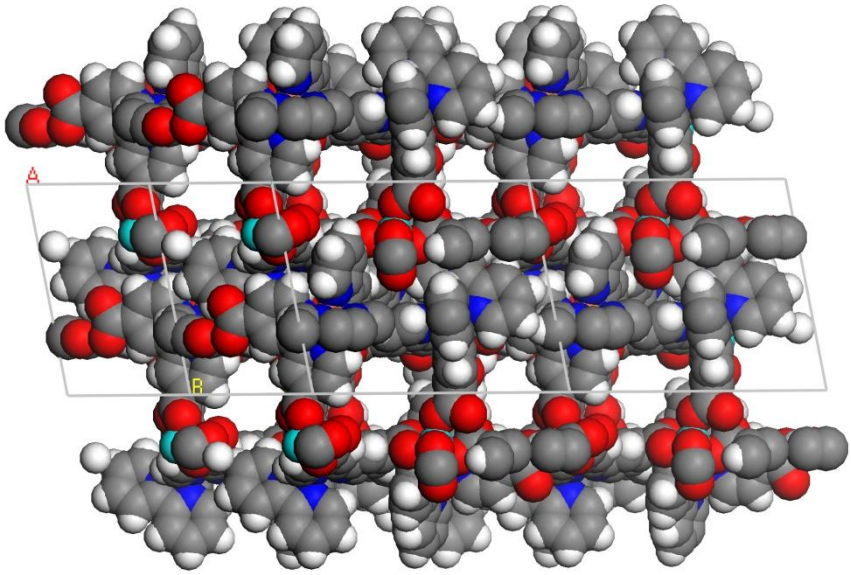

Figure 1-4. Space-filling model of **1** as viewed perpendicular to the (1 -1 0) plane. The solvent molecules were removed for clarity.

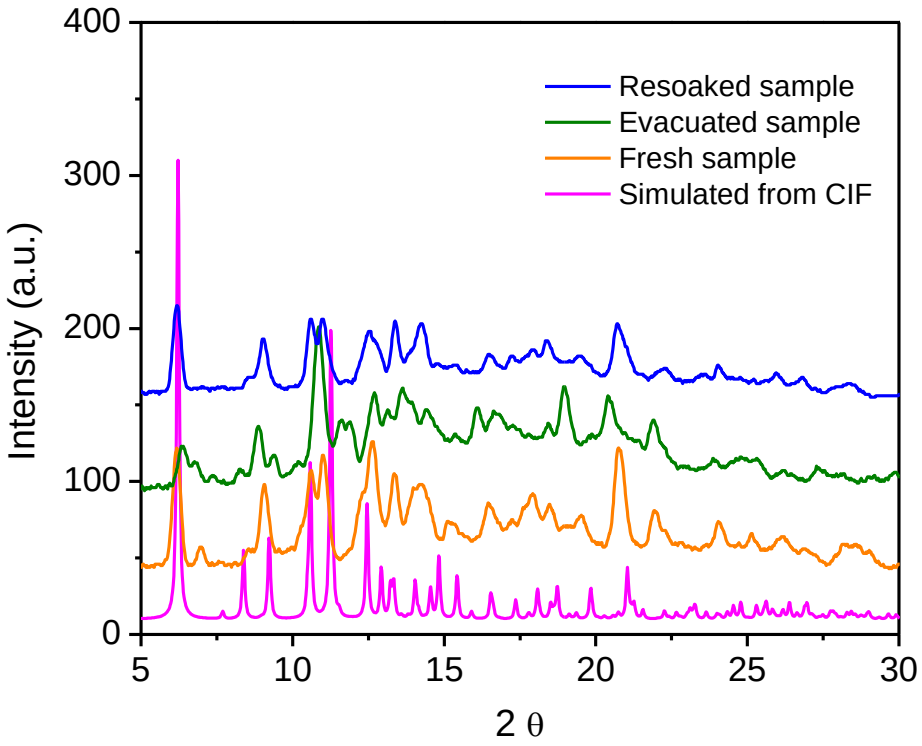

Figure 1-5. PXRD patterns of **1**. From bottom to top: simulated PXRD pattern from single crystal structure, experimental PXRD from fresh crystal, from evacuated sample, and from the evacuated sample that was re-soaked in the DMF/H_2O mixture.

The PXRD patterns of **1** show that the removal of solvent leads to a distortion of the crystal lattice but upon re-soaking the crystal in solvent the PXRD returns to the original state. The emission lifetime is very sensitive to the crystallinity of the particle with the lifetime decreasing as defect sites are introduced. Even low concentrations of defects can have a large impact because of excited state migration. The average lifetime of **1** was determined to be 140 ns when the sample was vacuum evacuated to remove all oxygen and solvent. The average lifetime increased to 610 ns when microcrystals of **1** were measured as a suspension in degassed MeCN. This suggests that the solvent in the pores is necessary to retain crystallinity and a long emission lifetime.

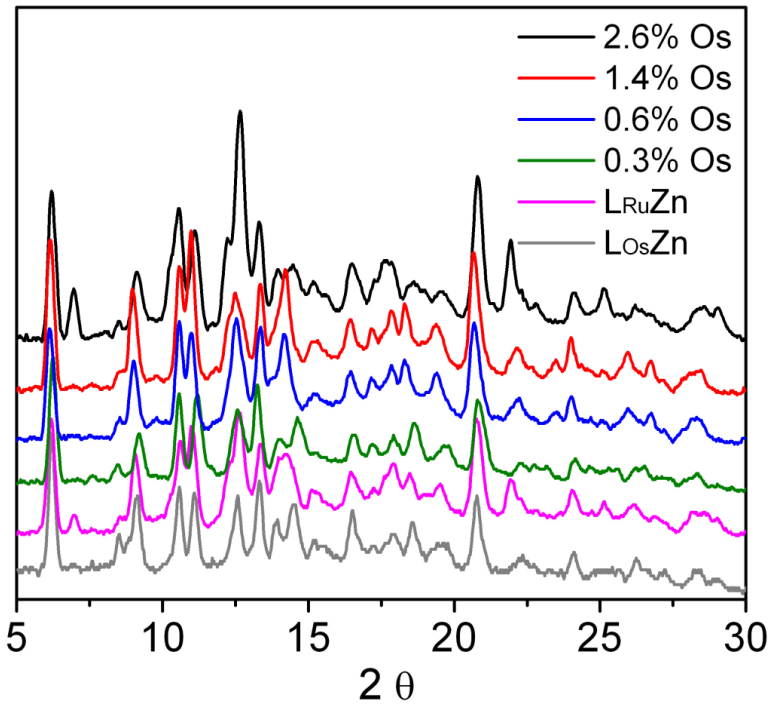

Figure 1-6. PXRD patterns showing the isostructural nature of **1**, Os-doped **1**, and **1-Os** MOFs. The crystal structure of **1** is unchanged with different Os doping levels.

Table 1-4. Determination of Os-doping levels in Os-doped **1** by ICP-OES.

[**L1**$_{Os}$-H$_4$](PF$_6$)$_2$ (μg) added to 1 mg of [**L1**$_{Ru}$-H$_4$](PF$_6$)$_2$	Calcd. mol% Os	Os Conc (ppb)	Ru Conc (ppb)	Observ. mol% Os
2	0.2	18.63	589.83 (diluted 5x)	0.3
5	0.5	25.86	476.64 (diluted 5x)	0.6
10	0.9	12.01	444.7	1.4
20	1.8	22.94	459.14	2.6

Variable amounts of [**L1**$_{Os}$-H$_4$](PF$_6$)$_2$ were added to 1 mg of [**L1**$_{Ru}$-H$_4$](PF$_6$)$_2$ to make solutions in DMF and water, which were used to grow bulk crystals of Os-doped **1**. The Ru to Os ratios were determined using ICP-OES. The samples with 2 and 5 μg of added [**L1**$_{Os}$-H$_4$](PF$_6$)$_2$ were measured for Os and then diluted 5 times to ensure that Ru concentration was within the range of the standard. The Ru and Os concentrations for the samples with 10 and 20 μg [**L1**$_{Os}$-H$_4$](PF$_6$)$_2$ could be determined from the same solution.

It is desirable to control the MOF particle size for applications in light harvesting and a synthesis was developed to make microscale crystals of **1**. The role of crystal size will be

examined in chapter 3. Microcrystals of **1** were prepared via microwave synthesis at 70 ^{o}C in a CEM MARS 5 microwave by the addition of **L1$_{Ru}$**-H_4 and $Zn(NO_3)_2$ in a solvent mixture of DMF and H_2O at a 60% yield. Os-doped **1** and **1-Os** microcrystals were prepared in the same manner as described above with a variable amount of added **L1$_{Os}$**-H_4 in similar yields. The particle morphology was retained as the Os content was altered as shown below by SEM. The TGA of **1-Os** showed increased weight loss as a result of the formation of volatile OsO_4.

Table 1-5. Os content in doped **1** microcrystals.

Sample	**L1$_{Ru}$**-H_4	**L1$_{Os}$**-H_4	Expected mol% Os	Experimental mol% Os
1	3.0 mg	0	0 %	0%
2	3.0 mg	0.003 mg	0.1 %	0.11 %
3	3.0 mg	0.006 mg	0.2 %	0.17 %
4	3.0 mg	0.015 mg	0.5 %	0.32 %
5	3.0 mg	0.03 mg	0.9 %	0.61 %
6	3.0 mg	0.06 mg	1.8 %	1.29 %
7	0	3.0 mg	100 %	100%

All of the microcrystal preparations contained 8.0 mg of $Zn(NO_3)_2$, 8.0 mL of DMF, and 3.0 mL of H_2O.

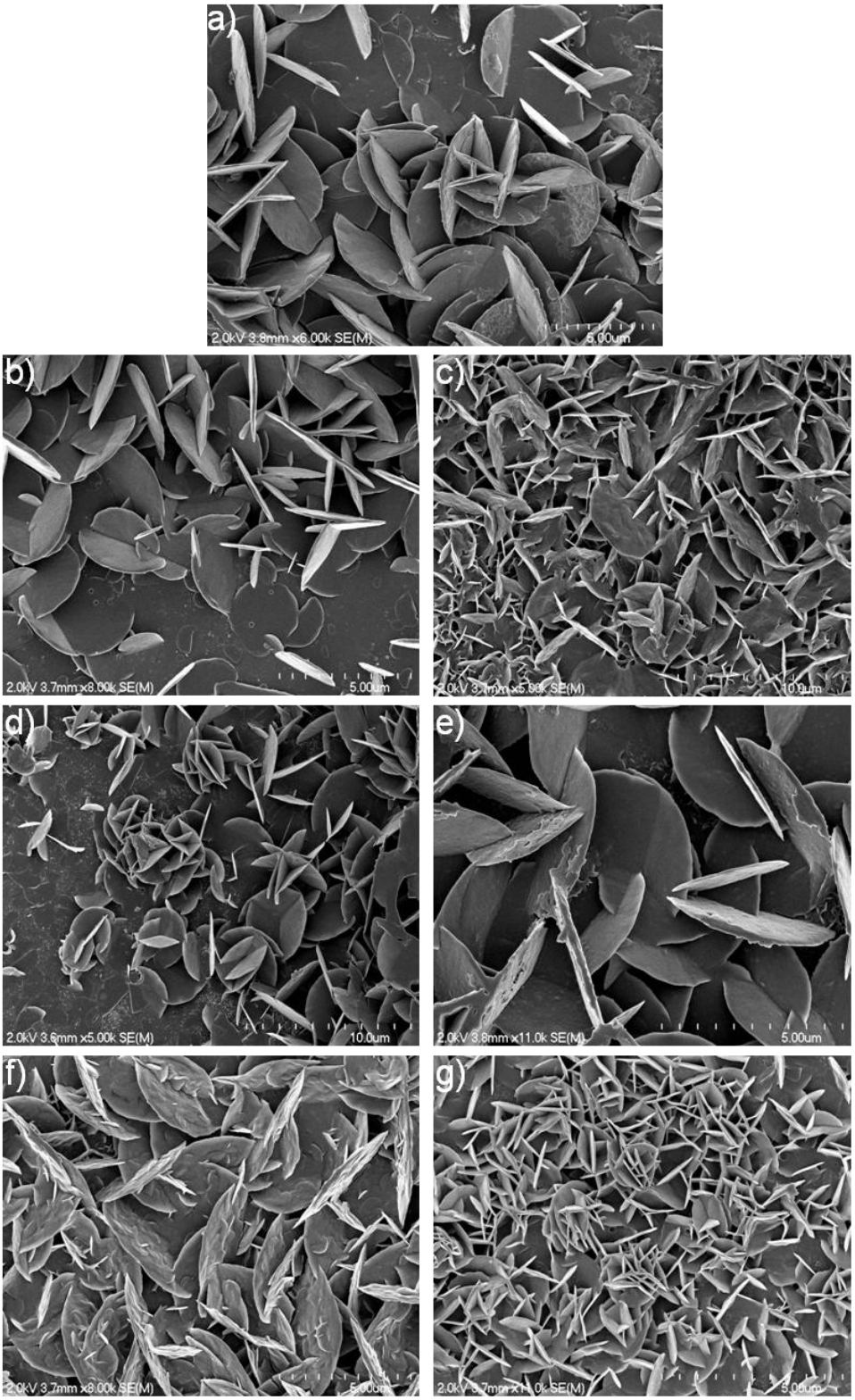

Figure 1-7. SEM images of **1** microcrystals with various Os doping levels: (a), 0.0 wt% Os; (b), 0.11% wt Os; (c), 0.17 wt% Os; (d), 0.32 wt% Os; (e), 0.61 wt% Os; (f), 1.29 wt% Os; (g), 100 wt% Os.

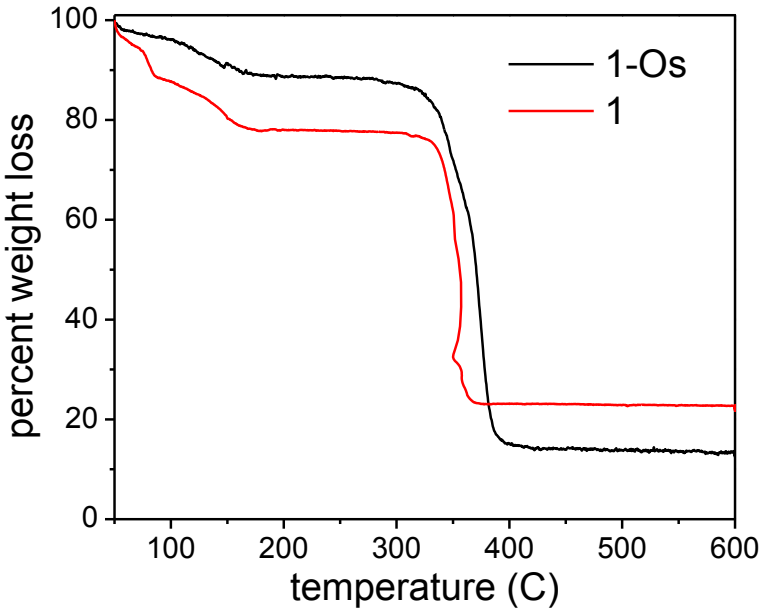

Figure 1-8. TGA of **1** and **1-Os** MOFs (where M = Ru or Os). The theoretical weight loss for **1** (79.1%) agrees well with the experimentally determined value (77.8%). The weight loss for **1-Os** (86.7%) is much higher than expected because volatile OsO_4 was produced during the TGA experiment.

The solution phase absorption and emission spectra of the monomer compounds are shown in Figures 1-9 and 1-10. The spectra for the Ru(II) and Os(II) monomers both show the singlet metal-to-ligand (MLCT) absorption bands between 400-500 nm, whereas the Os(II) complex shows the broad absorption between 600-750 nm that corresponds to direct excitation to the triplet state. The emission from the Os(II) monomer peaks at 800 nm and is significantly less intense than the Ru(II) emission. Lifetime measurements are consistent with measurements performed on similar Ru(II) and Os(II) polypyridyl systems.

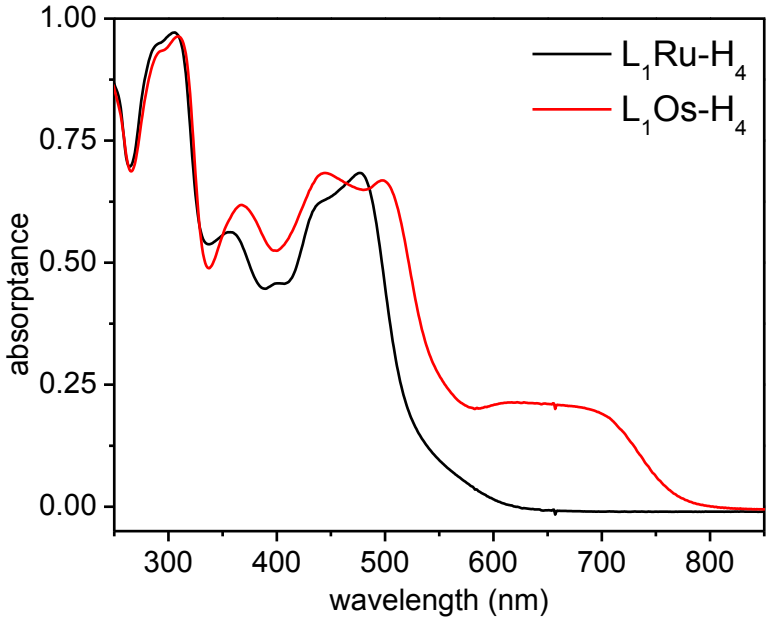

Figure 1-9. Solution absorptance of [$\mathbf{L1_{Ru}}$-H_4]$(PF_6)_2$, and [$\mathbf{L1_{Os}}$-H_4]$(PF_6)_2$ in methanol.

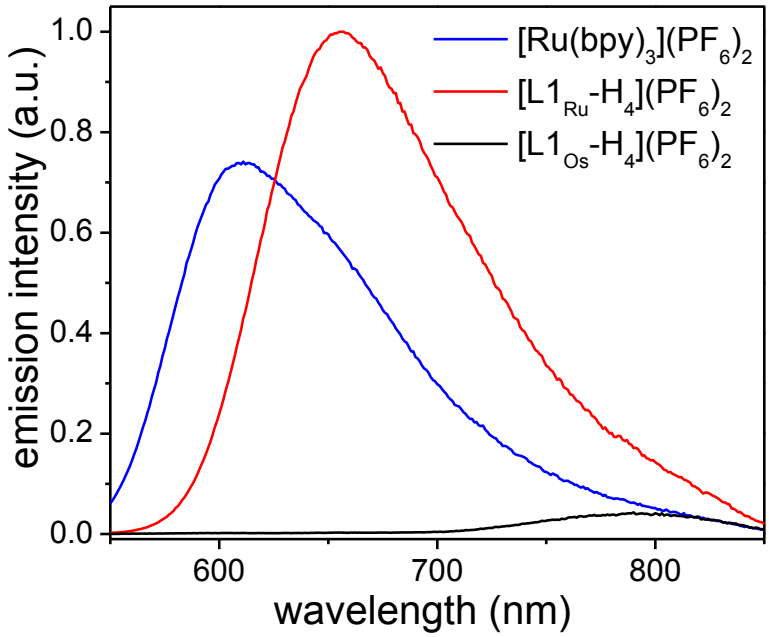

Figure 1-10. Solution steady-state emission of $[Ru(bpy)_3](PF_6)_2$, ([$\mathbf{L1_{Ru}}$-H_4]$(PF_6)_2$), and ([$\mathbf{L1_{Os}}$-H_4]$(PF_6)_2$) in methanol.

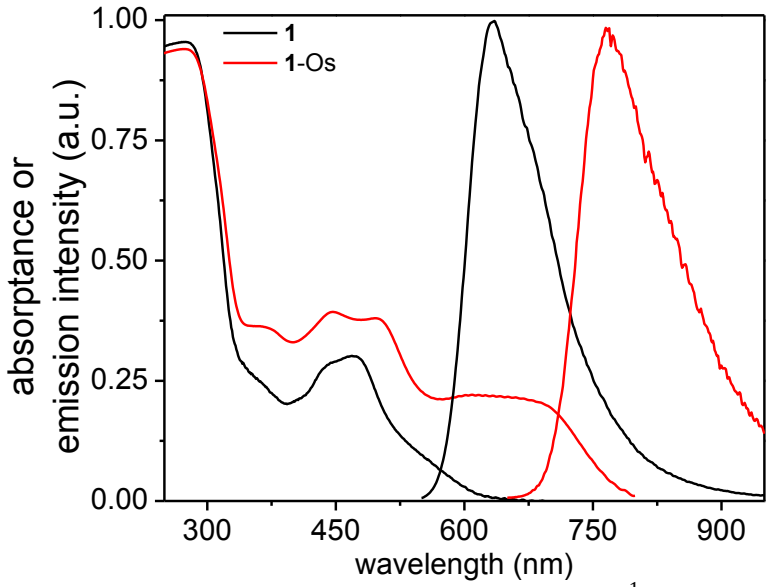

Figure 1-11. Solid State absorptance of **1** and **1-Os** MOFs. A ^{1}MLCT absorption band is observed between 400-600 nm for **1**. **1-Os** also has a ^{1}MLCT absorption from 400-600 and a broad ^{3}MLCT absorption out to 800 nm because of strong spin-orbit coupling.

1.3.2.2 Synthesis and Characterization of MOF-2

2 was prepared by the addition of $\mathbf{L2_{Ru}}$-H_4 and $Zn(NO_3)_2$ in a solvent mixture of DEF and H_2O. Large, bright orange crystals of **2** were obtained after heating the mixture at 75°C for three days with a 70% yield. Microcrystals of **2** were obtained in a similar yield after heating the mixture at 85°C for one day. Os doped **2** and **2**-Os samples were prepared in the same manner as described above with a variable amount of added $\mathbf{L2_{Os}}$-H_4 in similar yields.

[($\mathbf{L2_{Ru}}$-H_2)Zn]•$3H_2O$, **2**, crystallizes in the orthorhombic space group Pbcn, with one $\mathbf{L2_{Ru}}$-H_2 ligand and one zinc atom in the asymmetric unit. With a tetrahedral geometry, the Zn center is coordinated by two oxygen atoms from the deprotonated carboxylate groups of the $\mathbf{L2_{Ru}}$-H_2 ligand and two nitrogens from the bridging cyano groups forming a 2D bilayer structure. Packed along b axis, the 2D layers have a closest distance of 6.6 Å between bpy planes of adjacent layers. The shortest distance between two Ru centers within bilayers is 6.8 Å and 11.9 Å for Ru centers between bilayers.

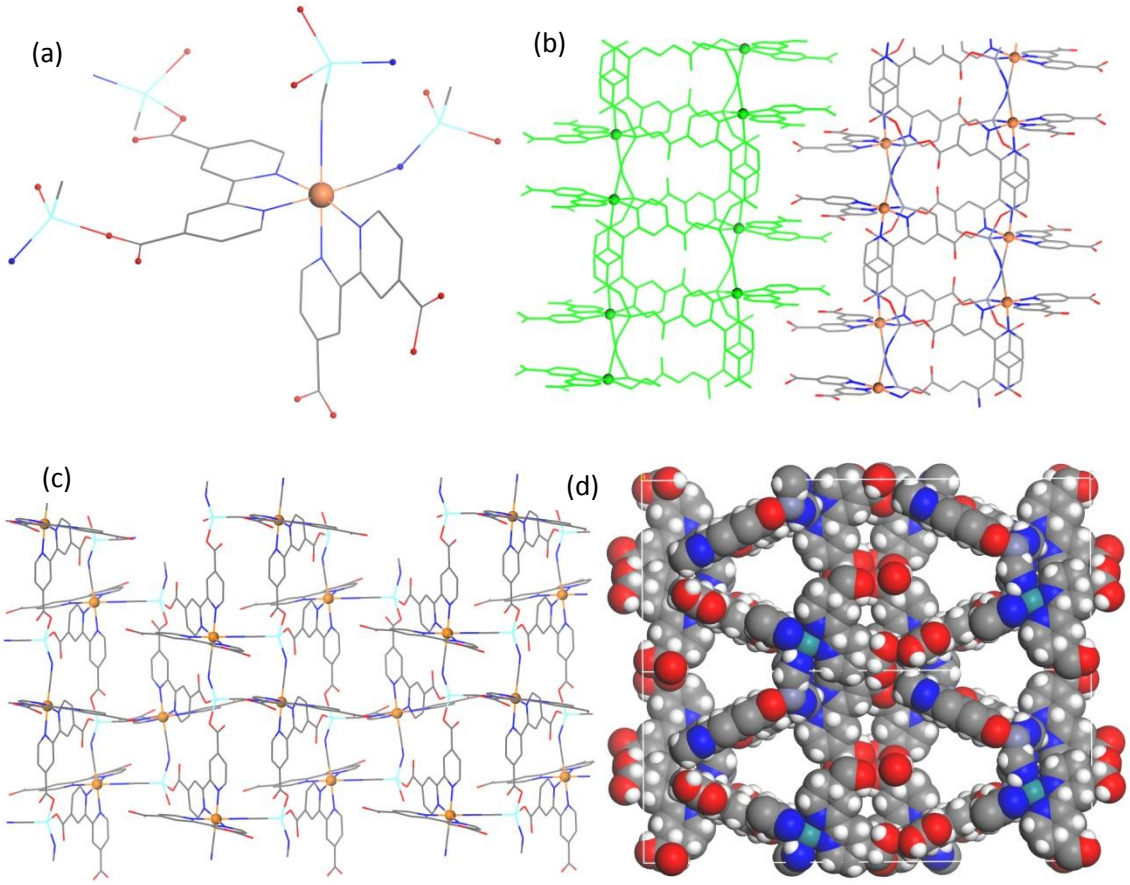

Figure 1-12. Crystal structure of **2**. (a) Wireframe model showing the connectivity of $\mathbf{L2}_{Ru}$ and Zn centers. (b) A side view of a 2D bilayer along the a axis. (c) A top view of the 2D bilayer structure along the b axis. (d) A spacefilling model of 2D bilayers along the c axis.

Table 1-6. Os content in doped **2** microcrystals.

Sample	$\mathbf{L2_{Ru}}$-$\mathbf{H_4}$	$\mathbf{L2_{Os}}$-$\mathbf{H_4}$	Expected mol% Os	Experimental mol% Os
1	5.0 mg	0	0 %	0%
2	5.0 mg	0.005 mg	0.1 %	0.12%
3	5.0 mg	0.01 mg	0.2 %	0.23%
4	5.0 mg	0.025 mg	0.4 %	0.50%
5	5.0 mg	0.05 mg	0.9 %	1.04%
6	5.0 mg	0.1 mg	1.7 %	1.98%
7	0	5.0 mg	100 %	100 %

All Os doped **2** microcrystal preparations contained 5.0 mg of $Zn(NO_3)_2$, 1.25 mL of DEF, 0.5 mL of H_2O, and 65 µL of 3M HCl.

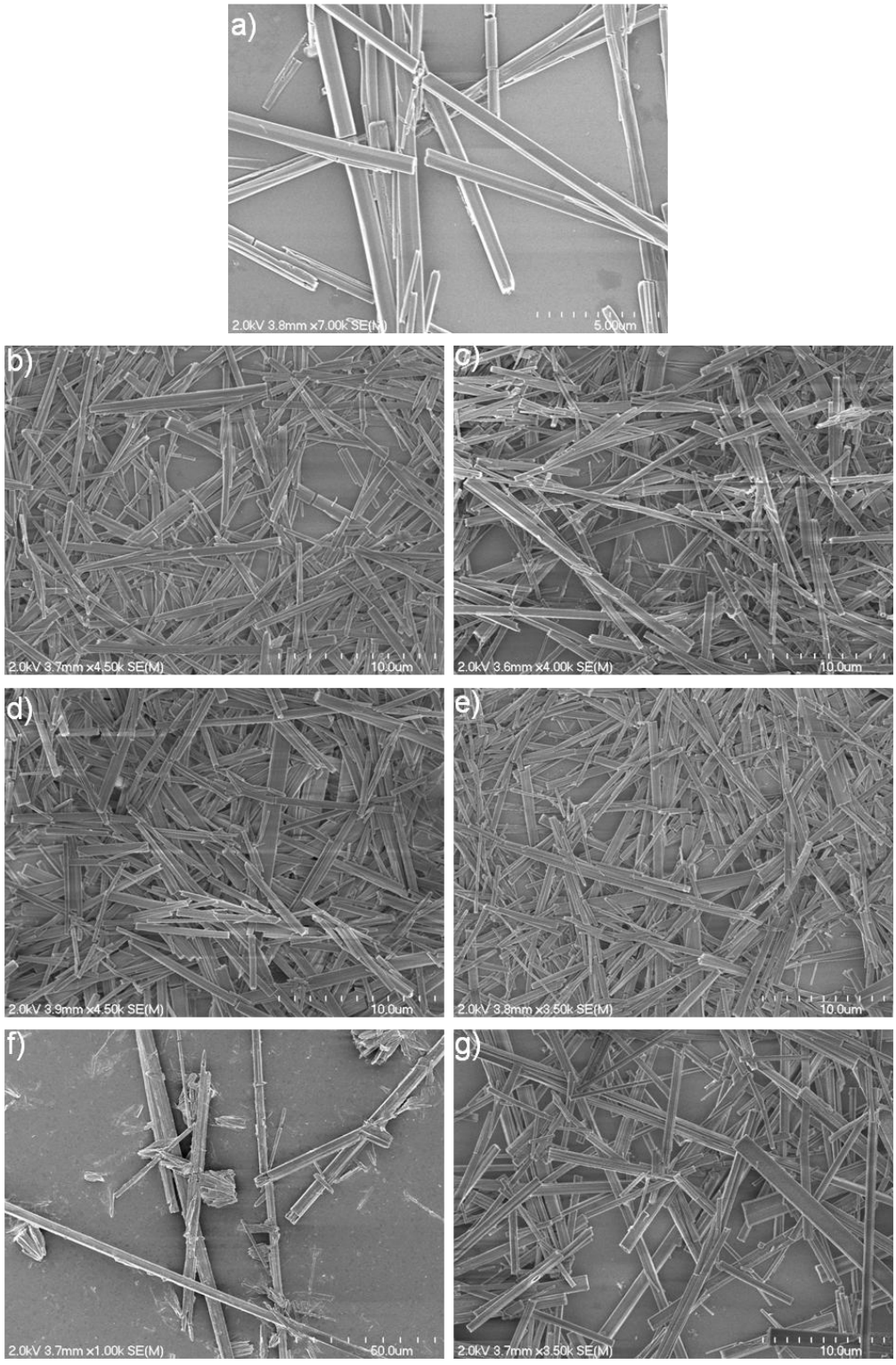

Figure 1-13. SEM images of **2** microcrystals with various Os doping levels: (a), 0.0 wt% Os; (b), 0.12 wt% Os; (c), 0.23 wt% Os; (d), 0.50 wt% Os; (e), 1.04 wt% Os; (f), 1.98 wt%Os; (g), 100 wt% Os.

Table 1-7. Crystallographic data of **2**.

Compound	**2**
Empirical formula	C26 H12 N6 O8Ru Zn
Formula weight	702.86
Temperature (K)	200
Wavelength (Å)	1.54178
Crystal system	Orthorhombic
Space group	Pbcn
Unit cell dimensions	a = 17.0829(4) b = 40.0431(7) c = 13.3183(3) α = 90 β = 90 γ = 90
Volume ($Å^3$)	9110.4(3)
Z	8
Density (calc. g/cm^3)	1.025
Absorption coeff.$(mm^-)^1$)	3.653
F(000)	2784
Crystal size (mm)	0.30 x 0.03 x 0.03
Crystal color & shape	red block
θ range data collection	2.21 to 54.99
Limiting indices	-11< *h* <18 -42< *k* <42 -14< *l* <13
Reflections collected	20186
Independent reflections	5681 [R(int) = 0.0964]
Refinement method	Full-matrix least-square on F^2
Data/restraints/parameters	5681 / 0 / 379
Goodness-of-fit on F^2	0.739
Final R indices $[I>2\sigma(I)]^{a,}$	R1 = 0.0509 wR2 = 0.1239
R indices (all data)	R1 = 0.0840 wR2 = 0.1400

[a] $R(F) = \Sigma||F_o| - |F_c||/\Sigma|F_o|$. [b] $R_W(F^2) = [\Sigma\{w(F_o^2 - F_c^2)^2\}/\Sigma\{w(F_o^2)^2\}]^{0.5}$; $w^{-1} = \sigma^2(F_o^2) + (aP)^2 + bP$, where $P = [F_o^2 + 2F_c^2]/3$ and *a* and *b* are constants adjusted by the program.

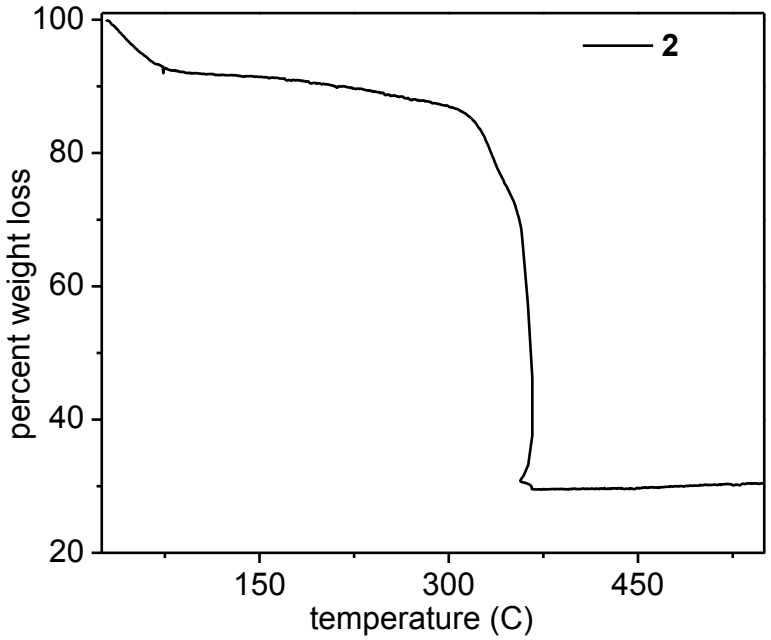

Figure 1-14. Thermogravimetric analysis of **2**.

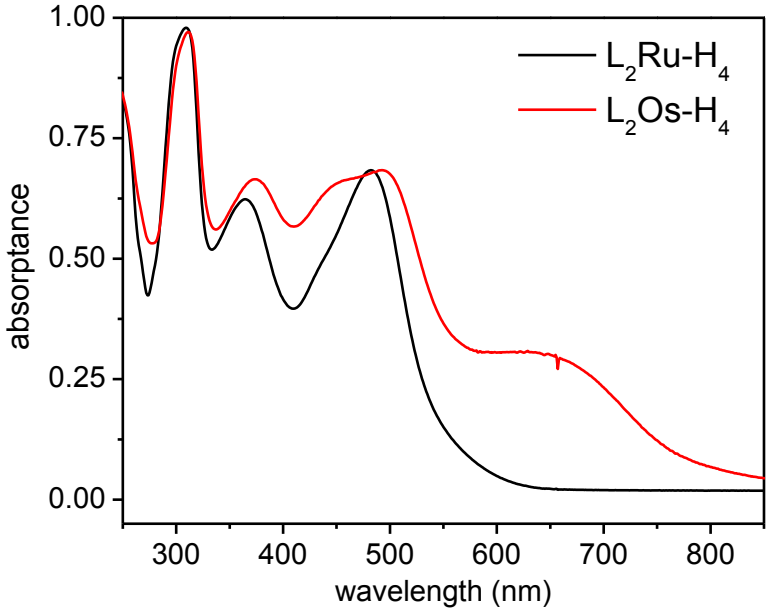

Figure 1-15. Solid state absorptance of $\mathbf{L2_{Ru}}$-H_4 and $\mathbf{L2_{Os}}$-H_4.

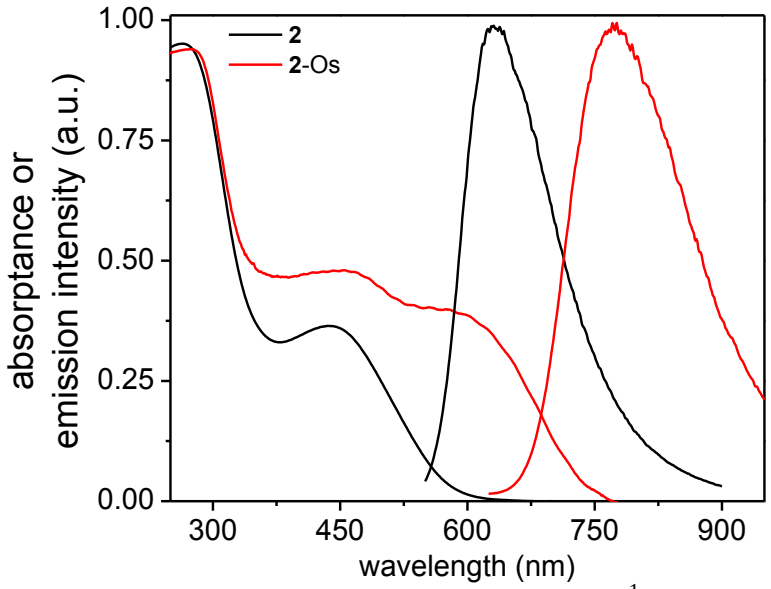

Figure 1-16. Solid State absorptance of **2** and **2-Os** MOFs. A ^{1}MLCT absorption band is observed between 375-600 nm for **2**. **2-Os** also has a ^{1}MLCT absorption from 375-600 nm and a broad ^{3}MLCT absorption out to 750 nm because of strong spin-orbit coupling.

1.3.2.3 Synthesis and Characterization of MOF-3

$[Zn_5(\mathbf{L3_{Ru}})_2\bullet(\mu\text{-}OH)\bullet(HCO_2)\bullet DMF\bullet 2H_2O]\bullet 6H_2O$, **3**, was prepared by the addition of $\mathbf{L3_{Ru}}$-H_4, $Zn(NO_3)_2$, and formic acid in a solvent mixture of DMF and H_2O. Red microscale crystals were obtained after heating the mixture at 80°C for 5 days with a 20% yield. **3-Os** and Os doped **3** were prepared in the same manner as described above with a variable amount of added $\mathbf{L3_{Os}}$-H_4 in similar yields.

Single-crystal X-ray structure determination of **3** revealed a three-dimensional (3D) framework that crystallizes in the monoclinic space group P2/n. In each asymmetric unit, there are two **L3** ligands, five zinc atoms, four bridging cyano groups with the carbon atom coordinating to Ru and the nitrogen atom coordinating to Zn, two H_2O and one DMF molecules coordinating to Zn centers, one bridging hydroxide group and one formate group to give the formula of $[Zn_5(\mathbf{L3})_2\bullet(\mu\text{-}OH)\bullet(HCO_2)\bullet DMF\bullet 2H_2O]\bullet 6H_2O$. There are two crystallographically distinct four-metal centered cores in which Ru and Zn are bridged by cyano groups. They have a dihedral angle of 9.3^{o} between the two planes formed by the two

crystallographically different cores and a dihedral angle of 35.4° between the two crystallographically identical cores. **3** has the open channels of 4.4×3.5 Å running along the *c* axis. PLATON[34] calculations indicated a void volume of 3376.2 Å^3 (38.8 % of the unit cell volume of 8768.4 Å^3), which is consistent with the thermogravimetric analysis result.

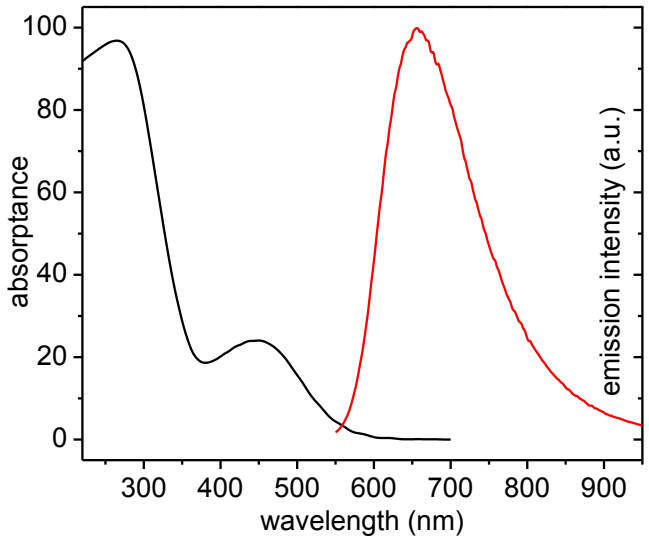

Figure 1-17. Absorptance and emission of **3**.

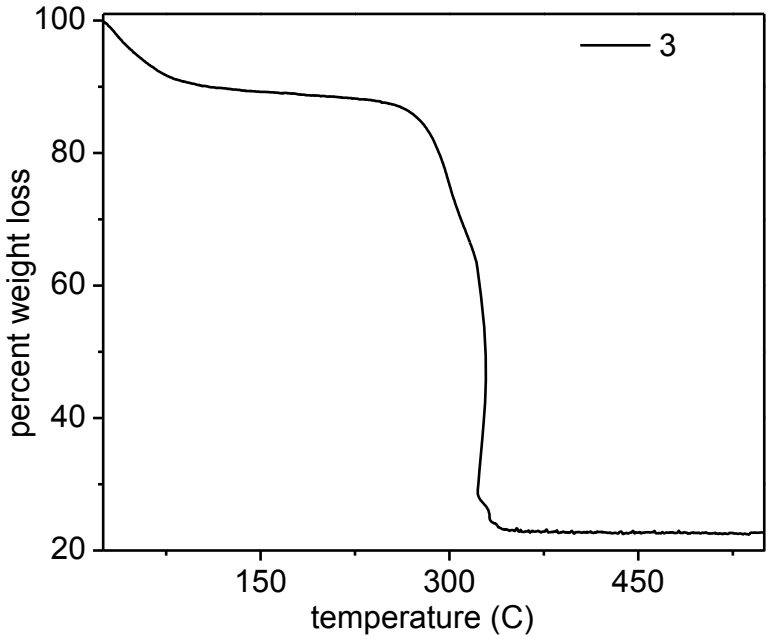

Figure 1-18. Thermogravimetric analysis of MOF-**3**.

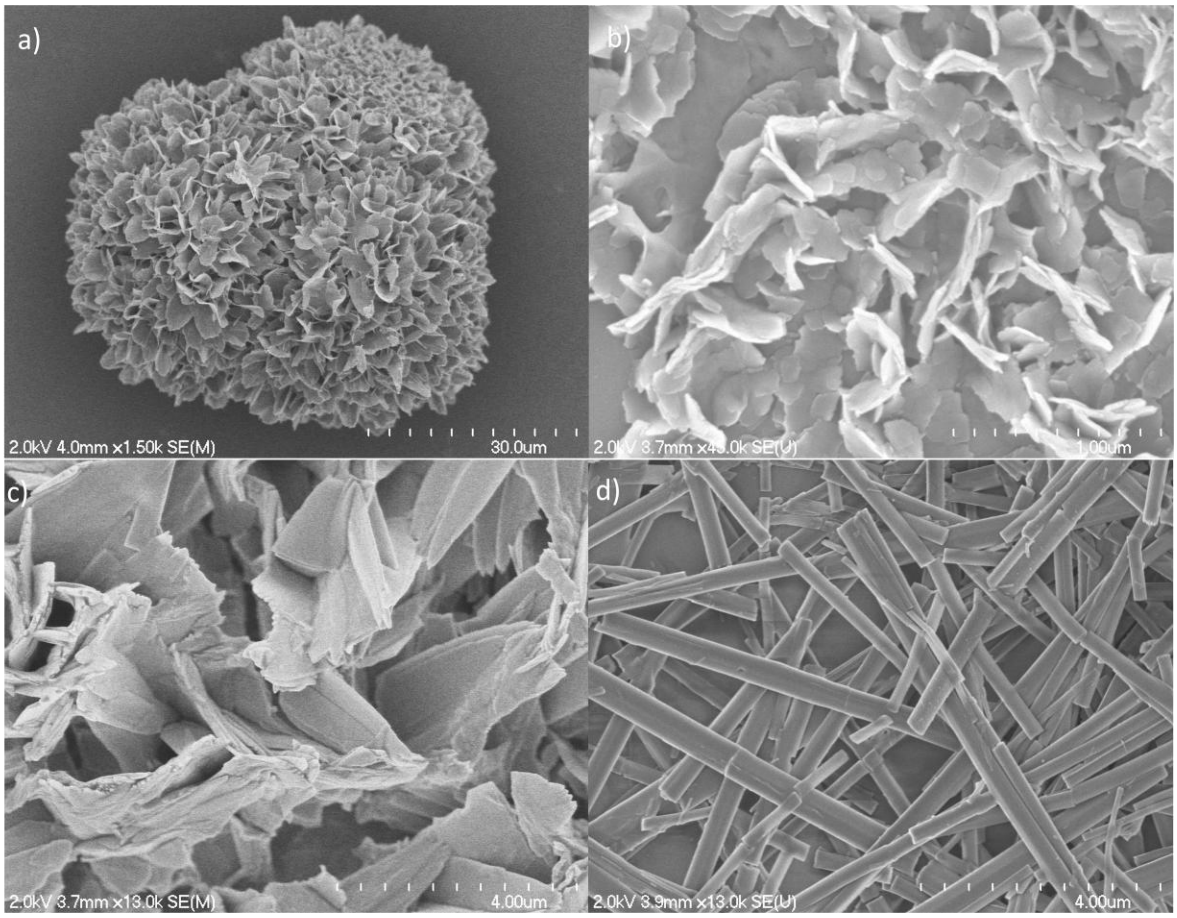

Figure 1-19. Scanning Electron Micrographs of a-c) **3** and d) **2**.

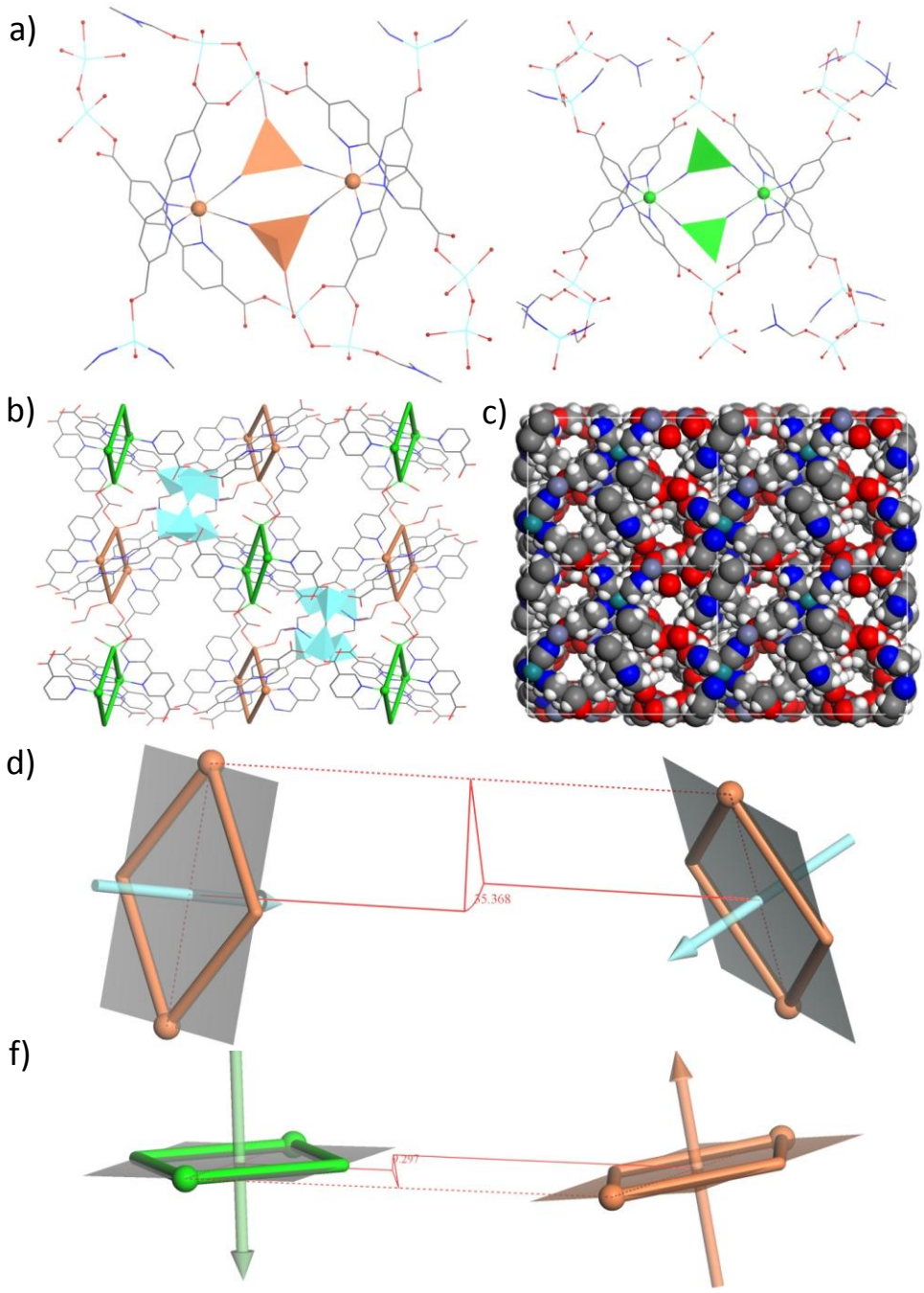

Figure 1-20. Structure of **3**. a) Connectivity patterns around the two crystallographically distinct 4-metal centered cores. The four coordinated zinc center was simplified as tetrahedral. Oxygen: red; Carbon: gray; Nitrogen: blue; Zinc: cyan; Ruthenium: orange and green. b) 3D view of **3** as viewed down the b axis (the 4-metal centered core was simplified as rectangle with different colors, and the ZnO_4 was simplified as terahedra). c) Space filling models of **3** as viewed down the c and b axis, showing the largest open channel in **3** with a dimension of 4.4×3.5 Å. Diheral angles between the two crystallographically identical (d) and distinct (e) 4-metal centered cores.

Table 1-8. Crystallographic data of **3**.

Compound	**3**
Empirical formula	$C_{56}H_{24}N_{13}O_{22.50}Ru_2Zn_5$
Formula weight	1767.87
Temperature (K)	223
Wavelength (Å)	1.54178
Crystal system	Monoclinic
Space group	P2/n
Unit cell dimensions	a = 21.1293(11) b = 16.4835(10) c = 24.9690(15) α = 90 β = 92.760(3) γ = 90
Volume ($Å^3$)	8686.2(9)
Z	4
Density (calcd. g/cm^3)	1.352
Absorption coeff. (mm^{-1})	4.816
F(000)	3476
Crystal size (mm)	0.10 x 0.05 x 0.02
Crystal color & shape	red block
θ range data collection	2.68 to 66.54
Limiting indices	-24< *h* <24 0< *k* <18 0< *l* <29
Reflections collected	14711
Independent reflections	14711 [R(int) = 0.0000]
Refinement method	Full-matrix least-square on F^2
Data/restraints/parameters	14711/380/787
Goodness-of-fit on F^2	0.896
Final R indices [I>2σ(I)][a,b]	R1 = 0.0856 wR2 = 0.1957
R indices (all data)	R1 = 0.1486 wR2 = 0.2145

[a] $R(F) = \Sigma||F_o| - |F_c||/\Sigma|F_o|$. [b] $R_W(F^2) = [\Sigma\{w(F_o^2 - F_c^2)^2\}/\Sigma\{w(F_o^2)^2\}]^{0.5}$; $w^{-1} = \sigma^2(F_o^2) + (aP)^2 + bP$, where $P = [F_o^2 + 2F_c^2]/3$ and *a* and *b* are constants adjusted by the program.

1.3.2.4 Synthesis and Characterization of MOF-4a and MOF-4b.

Microcrystals of **4a** were prepared via microwave synthesis by the addition of $[Ru(bpy)_3](PF_6)_2$, $NaNO_3$, $Al_2(SO_4)_3$, and oxalic acid in DMF and water with added HCl. The

solution was degassed and heated to 120 ^{o}C for 5 minutes to give a 70% yield. Os-doped **4a** and **4a-**Os microcrystals were prepared in the same manner as described above with a variable amount of added $[Os(bpy)_3](PF_6)_2$ in similar yields. Microcrystals of **4b** were prepared in a similar manner by the addition of $[Ru(bpy)_3](PF_6)_2$, $Zn(NO_3)_2$, and oxalic acid. Os-doped **4b** and **4b-**Os microcrystals were prepared in the same manner as described above with a variable amount of added $[Os(bpy)_3](PF_6)_2$ in similar yields.

$[Zn_2(\mathbf{L4_{Ru}})_2(oxalate)_3]$ (**4b**) crystallizes in the cubic space group $P4_332$, with one **L4** ligand, two Zn atom, and three oxalate molecules in the asymmetric unit. No significant amount of solvent was detected by TGA. The Zn center adopts an octahedral geometry by coordinating side-on to three oxalate molecules, forming a 3D structure. Each **L4** ligand has 6 nearest neighbors at a distance of 9.4 Å between Ru centers. The structure of **4a** has been reported previously and has the same connectivity as **4b** however the two Zn^{2+} atoms are replaced by a Na^{+} and Al^{3+}.[64]

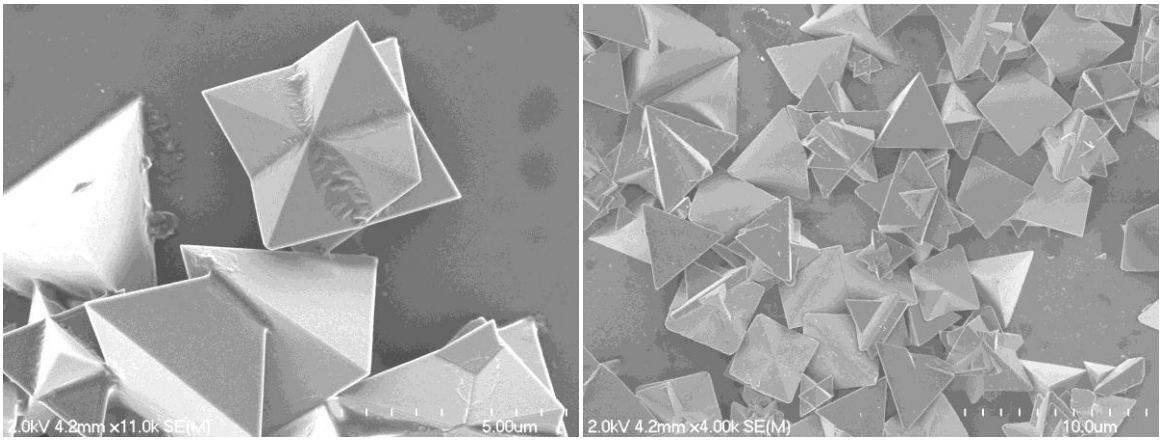

Figure 1-21. Representative SEM images of **4a**.

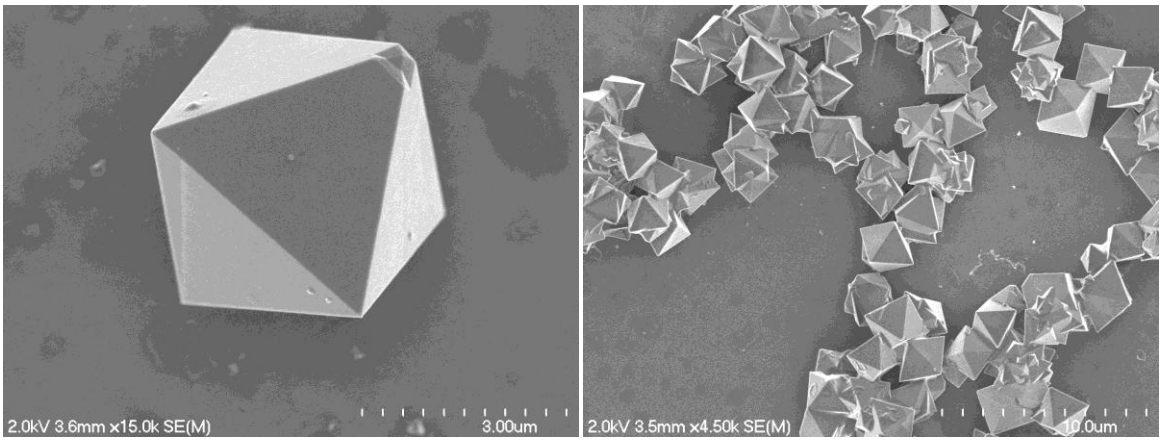

Figure 1-22. Representative SEM images of **4b**.

Table 1-9. Crystallographic data for **4b**.

Compound	**4b**
Empirical formula	C36 H24 N6 O12 Ru Zn2
Formula weight	964.42
Temperature (K)	296(2) K
Wavelength (Å)	1.54178
Crystal system	Cubic
Space group	P4332
Unit cell dimensions	a = 15.398(4) Å
	b = 15.398(4) Å
	c = 15.398(4) Å
	α = 90°
	β = 90°
	γ = 90°
Volume ($Å^3$)	3650.6(16)
Z	4
Density (calcd. g/cm^3)	1.755
Absorption coeff. (mm^{-1})	5.480
F(000)	1928
Crystal size (mm)	0.030×0.030 ×0.030
Crystal color & shape	red
θ range data collection	4.06 to 33.42°
Limiting indices	$-3 \leq h \leq 10$
	$-6 \leq k \leq 10$
	$-8 \leq l \leq 10$
Reflections collected	1040
Independent reflections	224 [R(int) = 0.0698]
Refinement method	Full-matrix least-square on F^2

Data/restraints/parameters	224 / 23 / 45
Goodness-of-fit on F^2	1.582
Final R indices $[I>2\sigma(I)]^{a,b}$	R1 = 0.1291
	wR2 = 0.3418
R indices (all data)	R1 = 0.1543
	wR2 = 0.3687

[a] $R(F) = \Sigma||F_o| - |F_c||/\Sigma|F_o|$. [b] $R_W(F^2) = [\Sigma\{w(F_o^2 - F_c^2)^2\}/\Sigma\{w(F_o^2)^2\}]^{0.5}$; $w^{-1} = \sigma^2(F_o^2) + (aP)^2 + bP$, where $P = [F_o^2 + 2F_c^2]/3$ and a and b are constants adjusted by the program.

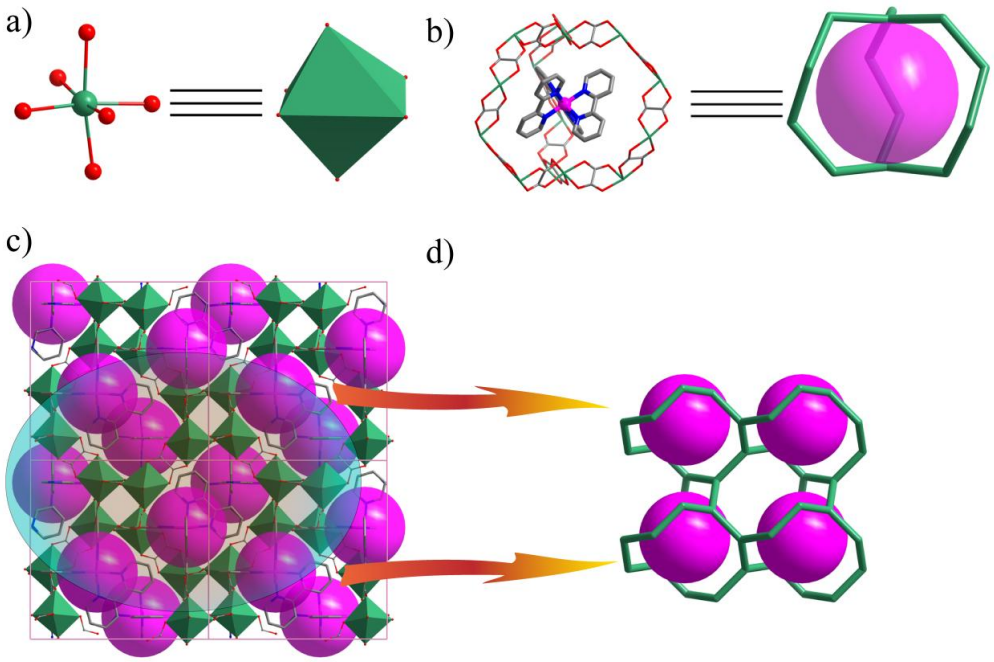

Figure 1-23. a) Schematic representation of octahedral building unit. b) Schematic representation of $Ru(bpy)_3^{2+}$ enclosed in the Zn oxalate cage. c) Packing diagram of **4b** as viewed down the b axis. d) Simplified connectivity of **4b** as viewed down the b axis.

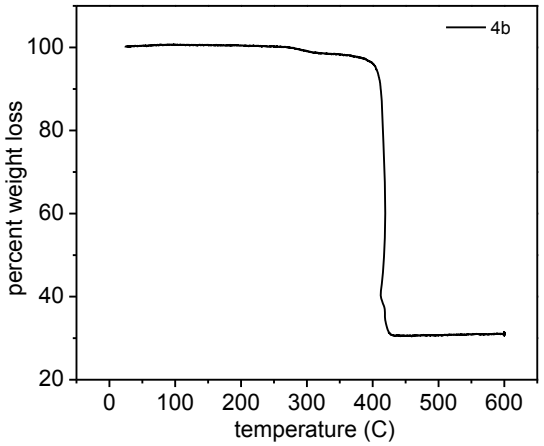

Figure 1-24. TGA of **4b**.

Thermogravimetric analysis of **4b** show little to no weight loss from solvent. The tight packing of the chromophores within the oxalate pores prevents solvent from entering the structure. The rigid environment of the oxalate framework leads to a high energy Ru emission with strong vibronic structure. The chromophores are insulated from solvent and therefore the emission is not broadened as in room temperature solution experiments. In fact, the emission spectral fitting shows similarity to what is observed for $Ru(bpy)_3^{2+}$ in a frozen solution at 77K. The emission of **4a** and **4b** are similar with **4a** having slightly higher emission energy and longer lifetime. These differences are likely a result of the degree of crystallinity in the sample because a small concentration of a trap site has been shown to dramatically quench the excited state. The effects of quenchers within the MOF structure will be examined in more detail in Chapter 2.

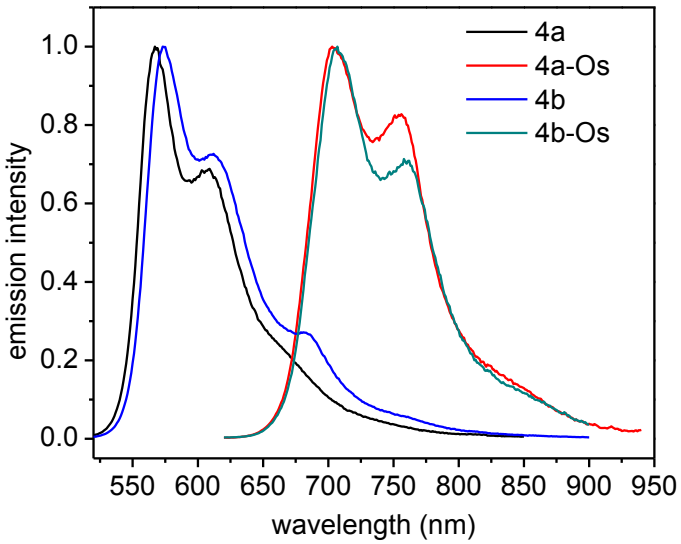

Figure 1-25. Steady-state emission spectra of **4a**, **4b, 4a-Os**, and **4b-Os**.

1.4 Concluding Remarks

A series of crystalline metal-organic frameworks with photo-active and redox-active components have been synthesized and characterized by x-ray diffraction along with other techniques. These materials show promise for many applications in solar energy research by

the self-assembly of metal complex building blocks with high energy, long-lived excited states into crystalline particles with dimensions that facilitate an antenna effect. The next chapters will examine their photophysical properties in more detail to elucidate energy transfer, interfacial electron transfer, and their use in sensing applications.

1.5 Experimental Section

Thermogravimetric analysis (TGA) was performed using a Shimadzu TGA-50 equipped with a platinum pan, and all samples were air-dried and heated at a rate of 3°C per minute in air. Scanning electron microscopy (SEM) images were collected with a Hitachi 4700 FESEM. Powder X-ray diffraction (PXRD) analyses were carried out using a Bruker SMART APEX II diffractometer using Cu radiation. The PXRD patterns were processed with the APEX II package using the phase ID plugin. A Varian 820-MS Inductively Coupled Plasma-Mass Spectrometer was used to determine the mol fraction of Os in the doped MOFs. Samples were introduced via a concentric glass nebulizer with a free aspiration rate of 0.4 mL/min, a Peltier-cooled double-pass glass spray chamber, and a quartz torch. A peristaltic pump carried samples from a SPS3 autosampler (Varian) to the nebulizer. All standards and samples were in 2% HNO_3, prepared with milliQ water.

All crystallographic measurements were made on a Bruker SMART Apex II CCD-based X-ray diffractometer system equipped with Cu–target X-ray tube and operated at 1600 watts. The frames were integrated with the Bruker SAINT© build in APEX II software package using a narrow-frame integration algorithm, which also corrects for the Lorentz and polarization effects. Absorption corrections were applied using SADABS. All of the structures were solved by direct methods and refined to convergence by least squares method on F^2 using the SHELXTL software suit. All non-hydrogen atoms are refined anisotropically.

SQUEEZE subroutine of the PLATON software suit was applied to remove the scattering from the highly disordered solvent molecules. The resulting new HKL4 files were used to further refine the structures.

Absorptance measurements of the MOFs were obtained on a Cary 5000 UV-Vis-NIR spectrophotometer with the specular reflectance accessory using transmission and reflectance measurements. The samples were prepared by dropwise addition of the MOFs onto a glass slide and the solvent was allowed to evaporate. Steady-state and time-resolved emission experiments were performed on an Edinburgh FLSP920 spectrometer in quartz cuvettes with magnetic stirring. The TCSPC measurements were collected using either an EPL-445 or EPL-485 laser with sub-100 ps pulse width.

1.5.1 Synthesis of Metal Complexes

Ru(4,4'-CO_2Et-bpy)$_2$$Cl_2$. Ru(4,4'-$CO_2$Et-bpy)$_2$$Cl_2$ was prepared by reacting two equivalents of 4,4'-CO_2Et-bpy, which was prepared by literature procedure,[61] (465mg, 1.55mmol) with Ru(cyclo-octadiene)Cl_2 polymer (217mg, 0.774 mmol of monomer) in 20 mL of argon degassed *o*-dichlorobenzene for two hours at 160 ˚C. After cooling to room temperature, the solution was precipitated by the addition of ether; the solid was filtered and washed with ether. Yield: 530 mg (89%).

[Ru(4,4'-CO_2H-bpy)$_2$bpy](PF$_6$)$_2$ ([L1$_{Ru}$-H$_4$](PF$_6$)$_2$). Ru(4,4'-CO_2Et-bpy)$_2$$Cl_2$ (490 mg, 0.634 mmol) and 1.2 equivalents of bpy (119 mg, 0.762 mmol) were refluxed under argon in 40 mL of H_2O:EtOH (1:1 v/v) for 8 hours. The complex was precipitated by the addition of 10 mL of saturated aqueous ammonium hexafluorophosphate and then majority of the ethanol was removed by rotovap. This product was filtered and washed with ether to remove excess bpy, then hydrolyzed by reflux under argon in 4M HCl for 12 hours.

Precipitation was achieved by the addition of 10 mL of saturated aqueous ammonium hexafluorophosphate. The product $[Ru(4,4'\text{-}CO_2H\text{-}bpy)_2bpy](PF_6)_2$ was filtered and washed with water to removed excess HCl. Yield: 476 mg (66%). ^{1}H NMR (D_2O with NaOD): 8.82 (s, 4H), 8.49 (d, 2H), 8.01 (t, 2H), 7.85 (t, 4H), 7.72 (d, 2H), 7.62 (m, 4H), 7.32 (t, 2H).[62, 63]

$Os(4,4'\text{-}CO_2Et\text{-}bpy)_2Cl_2$. $[OsCl_6](NH_4)_2$ (300 mg, 0.683 mmol) and two equivalents of 4,4'-CO_2Et-bpy (410 mg, 1.37 mmol) were refluxed in 25 mL of argon degassed ethylene glycol for one hour at 200 ˚C. After cooling, 25 mL of saturated aqueous Na dithionite was added to reduce any remaining Os(III) species. The product was filtered and washed with water and then ether. Yield: 446 mg (76%).[2]

$[Os(4,4'\text{-}CO_2H\text{-}bpy)_2bpy](PF_6)_2$ ($[L1_{Os}\text{-}H_4](PF_6)_2$). $Os(4,4'\text{-}CO_2Et\text{-}bpy)_2Cl_2$ (400 mg, 0.464 mmol) and 1.2 equivalents of bpy (87 mg, 0.56 mmol) were refluxed in 40 mL H_2O:EtOH (1:1 v/v) for three days. Isolation of the product was carried out in the same manner as described for $[Ru(4,4'\text{-}CO_2H\text{-}bpy)_2bpy](PF_6)_2$. Yield: 240 mg (45%). ^{1}H NMR (D_2O with NaOD): 8.77 (s, 4H), 8.44 (d, 2H), 7.80 (t, 2H), 7.74 (d, 2H), 7.71 (d, 2H), 7.57 (d, 2H), 7.48 (m, 4H), 7.21 (t, 2H). MS (ESI): 418.06 m/Z, expected 418.07 m/Z for $L_{Ru}\text{-}H_4$.

$Ru(4,4'\text{-}CO_2H\text{-}bpy)_2CN_2$ ($L2_{Ru}\text{-}H_4$). $Ru(4,4'\text{-}CO_2Et\text{-}bpy)_2Cl_2$ (200 mg, 0.259 mmol) was refluxed with KCN (840 mg, 12.9 mmol) in 25 mL of H_2O for 12 hours. The solution was concentrated and purified on a Sephadex column in order to remove excess KCN. Like fractions were combined and acidified with 1M HCl to precipitate **$L2_{Ru}$**-H_4. Yield: 120 mg (72%). ^{1}H NMR (CD_3CN): 9.45 (d, 2H), 8.70 (s, 2H), 8.62 (s, 2H), 7.91 (d, 2H), 7.58 (d, 2H), 7.47 (d, 2H).

$Os(4,4'\text{-}CO_2H\text{-}bpy)_2CN_2$ ($L2_{Os}\text{-}H_4$). $Os(4,4'\text{-}CO_2Et\text{-}bpy)_2Cl_2$ (190 mg, 0.220 mmol) was refluxed with KCN (750 mg, 11.5 mmol) in 25 mL of H_2O for 12 hours. The solution

was concentrated and purified on a Sephadex column in order to remove excess KCN. Like fractions were combined and acidified with 1M HCl to precipitate **$L2_{Os}$-H_4**. Yield: 110 mg (68%). ^{1}H NMR (DMSO-d_6): 9.81 (d, 2H), 8.92 (s, 2H), 8.84 (s, 2H), 7.97 (d, 2H), 7.62 (d, 2H), 7.55 (d, 2H).

Ru(5,5'-CO_2Et-bpy)$_2Cl_2$. Ru(5,5'-CO_2Et-bpy)$_2Cl_2$ was prepared by reacting two equivalents of 5,5'-CO_2Et-bpy, which was prepared in the same manner as 4,4'-CO_2Et-bpy,[61] (500 mg, 1.66 mmol) with the Ru(cyclo-octadiene)Cl_2 polymer (233 mg, 0.831 mmol of monomer) in 20 mL of argon degassed *o*-dichlorobenzene for one hour at 160 °C. After cooling to room temperature, the solution was precipitated by the addition of ether; the solid was filtered and stirred in H_2O for 4 hours to remove any charged impurities. The solid was filtered and dried with ether. Yield: 372 mg (58%).

Ru(5,5'-CO_2H-bpy)$_2CN_2$ ($L3_{Ru}$-H_4). Ru(5,5'-CO_2Et-bpy)$_2Cl_2$ (350 mg, 0.453 mmol) was refluxed with KCN (1.47 g, 22.6 mmol) in degassed H_2O for 12 hours. During the reaction the ester groups were hydrolyzed. The solution was concentrated and purified on a Sephadex column in order to remove excess KCN. The like fractions were combined and acidified to precipitate **$L3_{Ru}$-H_4**.Yield: 198 mg (68%). ^{1}H NMR (DMSO-d_6): 10.17 (s, 2H), 8.89 (d, 2H), 8.82 (d, 2H), 8.56 (d, 2H), 8.36 (d, 2H), 7.94 (s, 2H).

Os(5,5'-CO_2Et-bpy)$_2Cl_2$. $(NH_4)_2[OsCl_6]$ (300 mg, 0.683 mmol) and two equivalents of 5,5'-CO_2Et-bpy (410 mg, 1.37 mmol) were refluxed in 25 mL of argon-degassed ethylene glycol for one hour at 200 °C. After cooling, 25 mL of saturated aqueous sodium dithionite was added to reduce any remaining Os(III) species. The product was filtered and washed with water and then ether. Yield: 453 mg (77%).

Os(5,5'-CO_2H-bpy)$_2$$CN_2$ ($L3_{Os}$-H_4). Os(5,5'-CO_2Et-bpy)$_2$$Cl_2$ (200 mg, 0.232 mmol) was refluxed with KCN (830 mg, 12.7 mmol) in 25 mL of H_2O for 12 hours. During the reaction the ester groups were hydrolyzed. The solution was concentrated and purified on a Sephadex column in order to remove excess KCN. The like fractions were combined and acidified with 1M HCl to precipitate $L3_{Os}$-H_4.Yield: 133 mg (78%). ^{1}H NMR (DMSO-d_6): 10.26 (s, 2H), 8.86 (d, 2H), 8.77 (d, 2H), 8.28 (d, 2H), 8.18 (d, 2H), 7.91 (s, 2H).

[Ru(bpy)$_3$](PF$_6$)$_2$ ($L4_{Ru}$). [Ru(bpy)$_3$](PF$_6$)$_2$ was made according to literature procedure.[58]

[Os(bpy)$_3$](PF$_6$)$_2$ ($L4_{Os}$). [Os(bpy)$_3$](PF$_6$)$_2$ was made according to literature procedure.[60]

1.5.2 Synthesis of MOFs

[$L1_{Ru}$Zn]•2DMF•4H_2O, **1,** was prepared by the addition 1.0 mg (0.97 μmol) of [Ru(4,4'-CO_2H-bpy)$_2$bpy](PF$_6$)$_2$ ($L1_{Ru}$-H_4) and 1.0 mg (3.4 μmol) of Zn(NO_3)$_2$ in a solvent mixture of 0.3 mL DMF and 0.1 mL H_2O. Bright red crystals were obtained after heating the mixture at 90˚C for three days. Yield: 0.2 mg (30%). Os-doped **1** was prepared in the same manner as described above with a variable amount of added [Os(4,4'-CO_2H-bpy)$_2$bpy](PF$_6$)$_2$ ($L1_{Os}$-H_4), from 0.002 to 0.020 mg, in similar yields.

1-Os was prepared by the addition 1.0 mg (0.89 μmol) of [Os(4,4'-CO_2H-bpy)$_2$bpy](PF$_6$)$_2$ ($L1_{Os}$-H_4)and 1.0 mg (3.4 μmol) of Zn(NO_3)$_2$ in a solvent mixture of 0.3 mL DMF and 0.1 mL H_2O. Dark black crystals were obtained after heating the mixture 90˚C overnight. Yield: 0.4 mg (40%)

Microcrystals of **1** were prepared via microwave synthesis in a CEM MARS 5 by the addition of 3.0 mg (2.9 μmol) of $L1_{Ru}$-H_4 and 8.0 mg (27.2 μmol) of Zn(NO_3)$_2$ in a solvent

mixture of 8.0 mL DMF and 3.0 mL H_2O. The microcrystal growth was done at 70 ^oC with four vessels under rapid stirring and 180 W max power. The temperature was gradually ramped over a period of 10 minutes and then held for 50 minutes to give red-orange microcrystals of **1**. Yield: 1.6 mg (60%).

The Os-doped **1** microcrystals were prepared in the same manner as described above with a variable amount of added $\mathbf{L1_{Os}}$-H_4 (from 0.003 to 0.06 mg) in similar yields. The **1**-Os sample was prepared in the same manner with 3.0 mg (2.7 μmol) of $\mathbf{L1_{Os}}$-H_4 and 8.0 mg (27.2 μmol) of $Zn(NO_3)_2$ in a solvent mixture of 8.0 mL DMF and 3.0 mL H_2O to give black crystals. Yield: 1.8 mg (70%).

2 was prepared by the addition of 5.0 mg (7.8 μmol) of $\mathbf{L2_{Ru}}$-H_4 and 5.0 mg (17 μmol) of $Zn(NO_3)_2$ in a solvent mixture of 1.25 mL DEF and 0.5 mL H_2O with 65 μL of 3M HCl. Large, bright orange crystals of **2** were obtained after heating the mixture at 75°C for three days. Yield: 4.3 mg (70%). Microcrystals of **2** were obtained in a similar yield after heating the mixture at 85°C for one day.

Os doped **2** microcrystals: The Os-doped samples were prepared in the same manner as described above with a variable amount of added $\mathbf{L2_{Os}}$-H_4 (from 0.005 to 0.1 mg) in similar yields. The **2**-Os sample was prepared by the addition of 5.0 mg (6.8 μmol) of $\mathbf{L2_{Os}}$-H_4 and 5.0 mg (17 μmol) of $Zn(NO_3)_2$ in a solvent mixture of 1.25 mL DEF and 0.5 mL H_2O with 65 μL of 3M HCl. Black microcrystals were obtained after heating the mixture at 85°C for one day. Yield: 4.7 mg (80%).

$[Zn_5(\mathbf{L3_{Ru}})_2$•(μ-OH)•$(HCO_2)$•DMF•$2H_2O]$•$6H_2O$, **3**, was prepared in triplicate by the addition of 1.0 mg (1.6 μmol) of $\mathbf{L3_{Ru}}$-H_4 and 1.0 mg (3.4 μmol) of $Zn(NO_3)_2$ in a solvent mixture of 0.3 mL DMF, 0.1 mL H_2O and 3μL of formic acid. Red microscale crystals were

obtained after heating the mixture at 80°C for 5 days. Yield: 0.2 mg (20%) Bulk crystals were obtained under the same conditions without the addition of formic acid and required two weeks for growth.

The Os analog of **3**, **3-Os**, was prepared in triplicate by the addition of 1.0 mg (1.4 μmol) of $\mathbf{L3_{Ru}}$-H_4 and 1.0 mg (3.4 μmol) of $Zn(NO_3)_2$ in a solvent mixture of 0.3 mL DMF, 0.1 mL H_2O, and 3μL of formic acid. Black crystals were obtained after heating the mixture at 80°C for 5 days. Yield: 0.5 mg (40%).

Microcrystals of **4a** were prepared via microwave synthesis in a CEM DISCOVER by the addition of 0.5 mL each of 0.01M $[Ru(bpy)_3](PF_6)_2$ (5 μmol Ru), 0.01 M $NaNO_3$ (5 μmol Na), 0.005 M $Al_2(SO_4)_3$ (5 μmol Al), 0.03 M oxalic acid (15 μmol). The solutions were made in DMF except with $Al_2(SO_4)_3$ which was 1:1 water:DMF. An additional 1.5 mL of water and 1.5 mL of DMF were added along with 15 μL of 3M HCl. The microwave tube was sealed and if denoted as synthesized under air no further treatment was conducted before microwave heating. The samples prepared oxygen free were nitrogen bubble degassed for 30 min and sealed with parafilm before heating. The microcrystal growth was done at 120 ^oC with stirring for 5 minutes and 300 W max power to give orange microcrystals of **4a**. The oxygen free particles were isolated by centrifugation in a glove box and washed 3 times with ethanol. Yield: 3.0 mg (70%).

The Os-doped **4a** microcrystals were prepared in the same manner as described above with a variable amount of added $[Os(bpy)_3](PF_6)_2$ (from 10 to 50 nmol) in similar yields. The **4a**-Os sample was prepared in the same manner with $[Os(bpy)_3](PF_6)_2$ instead of $[Ru(bpy)_3](PF_6)_2$. Yield: 3.2 mg (70%).

Microcrystals of **4b** were prepared in a similar manner by the addition of 0.25 mL each of 0.01M $[Ru(bpy)_3](PF_6)_2$ (2.5 μmol Ru), 0.02 M $Zn(NO_3)_2$ (5 μmol Zn), 0.03 M oxalic acid (7.5 μmol). The solutions were made in DMF and an additional 1.75 mL of water and 2.5 mL of DMF were added along with 30 μL of 3M HCl. The microwave tube was sealed and if denoted as synthesized under air no further treatment was conducted before microwave heating. The samples prepared oxygen free were nitrogen bubble degassed for 30 min and sealed with parafilm before heating. The microcrystal growth was done at 120 ^oC with stirring for 5 minutes and 300 W max power to give orange microcrystals of **4b**. The oxygen free particles were isolated by centrifugation in a glove box and washed 3 times with ethanol. Yield: 3.7 mg (80%).

The Os-doped **4b** microcrystals were prepared in the same manner as described above with a variable amount of added $[Os(bpy)_3](PF_6)_2$ (from 5 to 25 nmol) in similar yields. The **4b-**Os sample was prepared in the same manner with $[Os(bpy)_3](PF_6)_2$ instead of $[Ru(bpy)_3](PF_6)_2$. Yield: 4.1 mg (80%).

1.6 References

1. Law, M.; Greene, L. E.; Johnson, J. C.; Saykally, R.; Yang, P. D., Nanowire dye-sensitized solar cells. *Nature Materials* 2005, 4, 455-459.

2. Concepcion, J. J.; Jurss, J. W.; Brennaman, M. K.; Hoertz, P. G.; Patrocinio, A. O. T.; Murakami Iha, N. Y.; Templeton, J. L.; Meyer, T. J., Making Oxygen with Ruthenium Complexes. *Acc. Chem. Res.* 2009, 42, 1954-1965.

3. Gust, D.; Moore, T. A.; Moore, A. L., Solar Fuels via Artificial Photosynthesis. *Accounts of Chemical Research* 2009, 42, 1890-1898.

4. Morris, A. J.; Meyer, G. J.; Fujita, E., Molecular Approaches to the Photocatalytic Reduction of Carbon Dioxide for Solar Fuels. *Accounts of Chemical Research* 2009, 42, 1983-1994.

5. Wasielewski, M. R., Self-Assembly Strategies for Integrating Light Harvesting and Charge Separation in Artificial Photosynthetic Systems. *Accounts of Chemical Research* 2009, 42, 1910-1921.

6. Youngblood, W. J.; Lee, S. H. A.; Maeda, K.; Mallouk, T. E., Visible Light Water Splitting Using Dye-Sensitized Oxide Semiconductors. *Accounts of Chemical Research* 2009, 42, 1966-1973.

7. Kelzenberg, M. D.; Boettcher, S. W.; Petykiewicz, J. A.; Turner-Evans, D. B.; Putnam, M. C.; Warren, E. L.; Spurgeon, J. M.; Briggs, R. M.; Lewis, N. S.; Atwater, H. A., Enhanced absorption and carrier collection in Si wire arrays for photovoltaic applications. *Nature Materials* 2010, 9, 239-244.

8. Collini, E.; Wong, C. Y.; Wilk, K. E.; Curmi, P. M. G.; Brumer, P.; Scholes, G. D., Coherently wired light-harvesting in photosynthetic marine algae at ambient temperature. *Nature* 2010, 463, 644-U69.

9. Ahn, T. K.; Avenson, T. J.; Ballottari, M.; Cheng, Y. C.; Niyogi, K. K.; Bassi, R.; Fleming, G. R., Architecture of a charge-transfer state regulating light harvesting in a plant antenna protein. *Science* 2008, 320, 794-797.

10. Guskov, A.; Kern, J.; Gabdulkhakov, A.; Broser, M.; Zouni, A.; Saenger, W., Cyanobacterial photosystem II at 2.9-angstrom resolution and the role of quinones, lipids, channels and chloride. *Nature Structural & Molecular Biology* 2009, 16, 334-342.

11. Jordan, P.; Fromme, P.; Witt, H. T.; Klukas, O.; Saenger, W.; Krauss, N., Three-dimensional structure of cyanobacterial photosystem I at 2.5 angstrom resolution. *Nature* 2001, 411, 909-917.

12. Cheng, Y.-C.; Fleming, G. R., Dynamics of light harvesting in photosynthesis. *Annu. Rev. Phys. Chem.* 2009, 60, 241-262.

13. Hammarstrom, L.; Hammes-Schiffer, S., Artificial photosynthesis and solar fuels. *Acc Chem Res* 2009, 42, 1859-60.

14. Wang, J. L.; Yan, J.; Tang, Z. M.; Xiao, Q.; Ma, Y. G.; Pei, J., Gradient shape-persistent pi-conjugated dendrimers for light-harvesting: Synthesis, photophysical properties, and energy funneling. *Journal of the American Chemical Society* 2008, 130, 9952-9962.

15. Kobuke, Y., Artificial light-harvesting systems by use of metal coordination. *European Journal of Inorganic Chemistry* 2006, 2333-2351.

16. Zhang, X. J.; Ballem, M. A.; Ahren, M.; Suska, A.; Bergman, P.; Uvdal, K., Nanoscale Ln(III)-Carboxylate Coordination Polymers (Ln = Gd, Eu, Yb): Temperature-Controlled Guest Encapsulation and Light Harvesting. *Journal of the American Chemical Society* 2010, 132, 10391-10397.

17. Mackowski, S., Hybrid nanostructures for efficient light harvesting. *Journal of Physics-Condensed Matter* 2010, 22.

18. Ward, M. D.; Barigelletti, F., Control of photoinduced energy transfer between metal-polypyridyl luminophores across rigid covalent, flexible covalent, or hydrogen-bonded bridges. *Coord. Chem. Rev.* 2001, 216-217, 127-154.

19. Fleming, C. N.; Maxwell, K. A.; DeSimone, J. M.; Meyer, T. J.; Papanikolas, J. M., Ultrafast excited-state energy migration dynamics in an efficient light-harvesting antenna polymer based on Ru(II) and Os(II) polypyridyl complexes. *J Am Chem Soc* 2001, 123, 10336-47.

20. Fleming, C. N.; Jang, P.; Meyer, T. J.; Papanikolas, J. M., Energy Migration Dynamics in a Ru(II)- and Os(II)-Based Antenna Polymer Embedded in a Disordered, Rigid Medium. *J. Phys. Chem. B* 2004, 108, 2205-2209.

21. Odobel, F.; Massiot, D.; Harrison, B. S.; Schanze, K. S., Photoinduced energy transfer between ruthenium and osmium tris-bipyridine complexes covalently pillared into γ-ZrP. *Langmuir* 2003, 19, 30-39.

22. Tsushima, M.; Ikeda, N.; Yoshimura, A.; Nozaki, K.; Ohno, T., Solid-state photochemistry: energy-transfer and electron-transfer of 3CT in crystals of [OsxRu1-x(bpy)3]X2 (x = 0-0.23). *Coord. Chem. Rev.* 2000, 208, 299-308.

23. Breu, J.; Kratzer, C.; Yersin, H., Crystal Engineering as a Tool for Directed Radiationless Energy Transfer in Layered {Λ-[Ru(bpy)3]Δ-[Os(bpy)3]}(PF6)4. *J. Am. Chem. Soc.* 2000, 122, 2548-2555.

24. Ockwig, N. W.; Delgado-Friedrichs, O.; O'Keeffe, M.; Yaghi, O. M., Reticular chemistry: occurrence and taxonomy of nets and grammar for the design of frameworks. *Acc Chem Res* 2005, 38, 176-82.

25. Bradshaw, D.; Warren, J. E.; Rosseinsky, M. J., Reversible concerted ligand substitution at alternating metal sites in an extended solid. *Science* 2007, 315, 977-80.

26. Evans, O. R.; Lin, W., Crystal engineering of NLO materials based on metal--organic coordination networks. *Acc Chem Res* 2002, 35, 511-22.

27. Moulton, B.; Zaworotko, M. J., From molecules to crystal engineering: supramolecular isomerism and polymorphism in network solids. *Chem Rev* 2001, 101, 1629-58.

28. Rowsell, J. L. C.; Yaghi, O. M., Strategies for hydrogen storage in metal-organic frameworks. *Angew. Chem., Int. Ed.* 2005, 44, 4670-4679.

29. Dinca, M.; Long, J. R., Hydrogen storage in microporous metal-organic frameworks with exposed metal sites. *Angew. Chem., Int. Ed.* 2008, 47, 6766-6779.

30. Wu, C.-D.; Hu, A.; Zhang, L.; Lin, W., A Homochiral Porous Metal-Organic Framework for Highly Enantioselective Heterogeneous Asymmetric Catalysis. *J. Am. Chem. Soc.* 2005, 127, 8940-8941.

31. Lee, J. Y.; Farha, O. K.; Roberts, J.; Scheidt, K. A.; Nguyen, S. B. T.; Hupp, J. T., Metal-organic framework materials as catalysts. *Chem. Soc. Rev.* 2009, 38, 1450-1459.

32. Rowsell, J. L.; Yaghi, O. M., Strategies for hydrogen storage in metal--organic frameworks. *Angew Chem Int Ed Engl* 2005, 44, 4670-9.

33. Kesanli, B.; Cui, Y.; Smith, M. R.; Bittner, E. W.; Bockrath, B. C.; Lin, W. B., Highly interpenetrated metal-organic frameworks for hydrogen storage. *Angew. Chem.-Int. Edit.* 2005, 44, 72-75.

34. Dinca, M.; Long, J. R., Hydrogen storage in microporous metal-organic frameworks with exposed metal sites. *Angew Chem Int Ed Engl* 2008, 47, 6766-79.

35. Zhao, D.; Yuan, D. Q.; Zhou, H. C., The current status of hydrogen storage in metal-organic frameworks. *Energy Environ. Sci.* 2008, 1, 222-235.

36. Rabone, J.; Yue, Y. F.; Chong, S. Y.; Stylianou, K. C.; Bacsa, J.; Bradshaw, D.; Darling, G. R.; Berry, N. G.; Khimyak, Y. Z.; Ganin, A. Y.; Wiper, P.; Claridge, J. B.; Rosseinsky, M. J., An adaptable peptide-based porous material. *Science* 2010, 329, 1053-7.

37. Yang, S.; Lin, X.; Blake, A. J.; Walker, G. S.; Hubberstey, P.; Champness, N. R.; Schroder, M., Cation-induced kinetic trapping and enhanced hydrogen adsorption in a modulated anionic metal-organic framework. *Nat Chem* 2009, 1, 487-93.

38. Matsuda, R.; Kitaura, R.; Kitagawa, S.; Kubota, Y.; Belosludov, R. V.; Kobayashi, T. C.; Sakamoto, H.; Chiba, T.; Takata, M.; Kawazoe, Y.; Mita, Y., Highly controlled acetylene accommodation in a metal-organic microporous material. *Nature* 2005, 436, 238-41.

39. Xiang, S. C.; Zhang, Z.; Zhao, C. G.; Hong, K.; Zhao, X.; Ding, D. R.; Xie, M. H.; Wu, C. D.; Das, M. C.; Gill, R.; Thomas, K. M.; Chen, B., Rationally tuned micropores within enantiopure metal-organic frameworks for highly selective separation of acetylene and ethylene. *Nat Commun* 2011, 2, 204.

40. Chen, B.; Xiang, S.; Qian, G., Metal-organic frameworks with functional pores for recognition of small molecules. *Acc Chem Res* 2010, 43, 1115-24.

41. Pramanik, S.; Zheng, C.; Zhang, X.; Emge, T. J.; Li, J., New Microporous Metal-Organic Framework Demonstrating Unique Selectivity for Detection of High Explosives and Aromatic Compounds. *J Am Chem Soc* 2011.

42. Allendorf, M. D.; Houk, R. J.; Andruszkiewicz, L.; Talin, A. A.; Pikarsky, J.; Choudhury, A.; Gall, K. A.; Hesketh, P. J., Stress-induced chemical detection using flexible metal-organic frameworks. *J Am Chem Soc* 2008, 130, 14404-5.

43. Xie, Z.; Ma, L.; deKrafft, K. E.; Jin, A.; Lin, W., Porous phosphorescent coordination polymers for oxygen sensing. *J Am Chem Soc* 132, 922-3.

44. Wu, C. D.; Hu, A.; Zhang, L.; Lin, W., A homochiral porous metal-organic framework for highly enantioselective heterogeneous asymmetric catalysis. *J Am Chem Soc* 2005, 127, 8940-1.

45. Ma, L.; Abney, C.; Lin, W., Enantioselective catalysis with homochiral metal-organic frameworks. *Chem Soc Rev* 2009, 38, 1248-56.

46. Lee, J.; Farha, O. K.; Roberts, J.; Scheidt, K. A.; Nguyen, S. T.; Hupp, J. T., Metal-organic framework materials as catalysts. *Chem Soc Rev* 2009, 38, 1450-9.

47. Ma, L.; Falkowski, J. M.; Abney, C.; Lin, W., A series of isoreticular chiral metal-organic frameworks as a tunable platform for asymmetric catalysis. *Nat Chem* 2010, 2, 838-46.

48. Lin, W.; Rieter, W. J.; Taylor, K. M., Modular synthesis of functional nanoscale coordination polymers. *Angew Chem Int Ed Engl* 2009, 48, 650-8.

49. deKrafft, K. E.; Xie, Z.; Cao, G.; Tran, S.; Ma, L.; Zhou, O. Z.; Lin, W., Iodinated nanoscale coordination polymers as potential contrast agents for computed tomography. *Angew Chem Int Ed Engl* 2009, 48, 9901-4.

50. Rieter, W. J.; Pott, K. M.; Taylor, K. M.; Lin, W., Nanoscale coordination polymers for platinum-based anticancer drug delivery. *J Am Chem Soc* 2008, 130, 11584-5.

51. Horcajada, P.; Chalati, T.; Serre, C.; Gillet, B.; Sebrie, C.; Baati, T.; Eubank, J. F.; Heurtaux, D.; Clayette, P.; Kreuz, C.; Chang, J. S.; Hwang, Y. K.; Marsaud, V.; Bories, P. N.; Cynober, L.; Gil, S.; Ferey, G.; Couvreur, P.; Gref, R., Porous metal-organic-framework nanoscale carriers as a potential platform for drug delivery and imaging. *Nat Mater* 9, 172-8.

52. Evans, O. R.; Lin, W., Crystal Engineering of NLO Materials Based on Metal-Organic Coordination Networks. *Acc. Chem. Res.* 2002, 35, 511-522.

53. Lan, A.; Li, K.; Wu, H.; Olson, D. H.; Emge, T. J.; Ki, W.; Hong, M.; Li, J., A luminescent microporous metal-organic framework for the fast and reversible detection of high explosives. *Angew. Chem., Int. Ed.* 2009, 48, 2334-2338.

54. Chen, B.; Wang, L.; Xiao, Y.; Fronczek, F. R.; Xue, M.; Cui, Y.; Qian, G., A luminescent metal-organic framework with Lewis basic pyridyl sites for the sensing of metal ions. *Angew. Chem., Int. Ed.* 2009, 48, 500-503.

55. Xie, Z.; Ma, L.; de Krafft, K. E.; Jin, A.; Lin, W., Porous Phosphorescent Coordination Polymers for Oxygen Sensing. *J. Am. Chem. Soc.* 2010, 132, 922-923.

56. Lin, W.; Rieter, J. W.; Taylor, K. M. L., Modular synthesis of functional nanoscale coordination polymers. *Angew. Chem., Int. Ed.* 2009, 48, 650-658.

57. Argazzi, R.; Bignozzi, C. A.; Heimer, T. A.; Castellano, F. N.; Meyer, G. J., Enhanced Spectral Sensitivity from Ruthenium(II) Polypyridyl Based Photovoltaic Devices. *Inorg. Chem.* 1994, 33, 5741-9.

58. Caspar, J. V.; Meyer, T. J., PHOTOCHEMISTRY OF RU(BPY)32+ - SOLVENT EFFECTS. *Journal of the American Chemical Society* 1983, 105, 5583-5590.

59. Sauve, G.; Cass, M. E.; Doig, S. J.; Lauermann, I.; Pomykal, K.; Lewis, N. S., High quantum yield sensitization of nanocrystalline titanium dioxide photoelectrodes with cis-dicyanobis(4,4 '-dicarboxy-2,2 '-bipyridine)osmium(II) ortris(4,4 '-dicarboxy-2,2 '-bipyridine)osmium(II) complexes. *Journal of Physical Chemistry B* 2000, 104, 3488-3491.

60. Kober, E. M.; Sullivan, B. P.; Dressick, W. J.; Caspar, J. V.; Meyer, T. J., HIGHLY LUMINESCENT POLYPYRIDYL COMPLEXES OF OSMIUM(II). *Journal of the American Chemical Society* 1980, 102, 7383-7385.

61. Hoertz, P. G.; Staniszewski, A.; Marton, A.; Higgins, G. T.; Incarvito, C. D.; Rheingold, A. L.; Meyer, G. J., Toward exceeding the Shockley-Queisser limit: Photoinduced interfacial charge transfer processes that store energy in excess of the equilibrated excited state. *Journal of the American Chemical Society* 2006, 128, 8234-8245.

62. Nazeeruddin, M. K.; Kalyanasundaram, K., Acid-base behavior in the ground and excited states of ruthenium(II) complexes containing tetraimines or dicarboxybipyridines as protonatable ligands. *Inorg. Chem.* 1989, 28, 4251-9.

63. Kober, E. M.; Caspar, J. V.; Sullivan, B. P.; Meyer, T. J., Synthetic routes to new polypyridyl complexes of osmium(II). *Inorg. Chem.* 1988, 27, 4587-98.

64. von Arx, M. E.; Burattini, E.; Hauser, A.; van Pieterson, L.; Pellaux, R.; Decurtins, S., Luminescence and energy transfer of Ru(bpy)(3) (2+), Cr(ox)(3) (3-), and Os(bpy)(3) (2+) in three-dimensional oxalato-networks. *Journal of Physical Chemistry A* 2000, 104, 883-893.

Chapter 2

ENERGY TRANSFER DYNAMICS IN METAL-ORGANIC FRAMEWORKS

2.1 Energy Transfer Dynamics in MOF-1

The photophysical properties of crystalline $Ru(bpy)_3^{2+}$ has been previously studied to elucidate its electronic structure and emission mechansism.[1-4] Ru to Os energy transfer has been studied in simple molecular crystals with a variety of counter ions and different structures and has demonstrated Ru to Ru hopping rates as fast as 125 ps.[5-8] MOFs provide a unique scaffold to self assemble chromophores in close proximity, near the shortest distance allowed by Van der Waals forces, and also provide increased stability which enables multiple applications that are not feasible with molecular crystals.

Os-doped **1** was the first MOF to demonstrate Ru to Os energy transfer characteristics and will be examined in detail in this chapter. Additional MOF structures have been made with varying degrees of energy transfer quenching efficiencies with the largest being the oxalate systems with $Ru(bpy)_3^{2+}$ trapped inside the anionic framework. A brief description of the theoretical work will also be included that examines the role of dimensionality in energy transfer.

Diffuse reflectance UV-Vis measurements showed a broad MLCT absorption band between 400-600 nm for **1** consistent with λ_{max} = 473 nm for [$\mathbf{L1_{Ru}}$-H_4]$(PF_6)_2$in MeOH. **1**-Os exhibits a broad ^{1}MLCT absorption band between 400-650 nm and an absorption band at 710 nm of ~1/3 the absorptivity arising from the partly spin-allowed "S→T" absorption to

^{3}MLCT with enhanced intensity due to spin-orbit coupling at Os(III) ($\xi(Os^{III}) \sim 3000\ cm^{-1}$). The normalized, uncorrected steady state emission spectra for both **1** and **1**-Os are shown in Figure 2-1b. As expected, the **1**-Os is significantly less emissive due to enhanced nonradiative decay resulting from the decreased energy gap and higher spin-orbit coupling.[9]

All MOF samples were washed with ethanol, vacuum degassed, and flame-sealed into capillary tubes under nitrogen. It was determined that the removal of solvent had a large negative influence of the photophysical properties of the material as a result of crystal deformation. Later experiments were performed on suspensions of crystals in either acetonitrile or ethanol. Lifetimes are reported as averages of values collected at a series of locations in multiple crystals. Variations in lifetimes of ~ 20% were observed between different locations and different crystals.

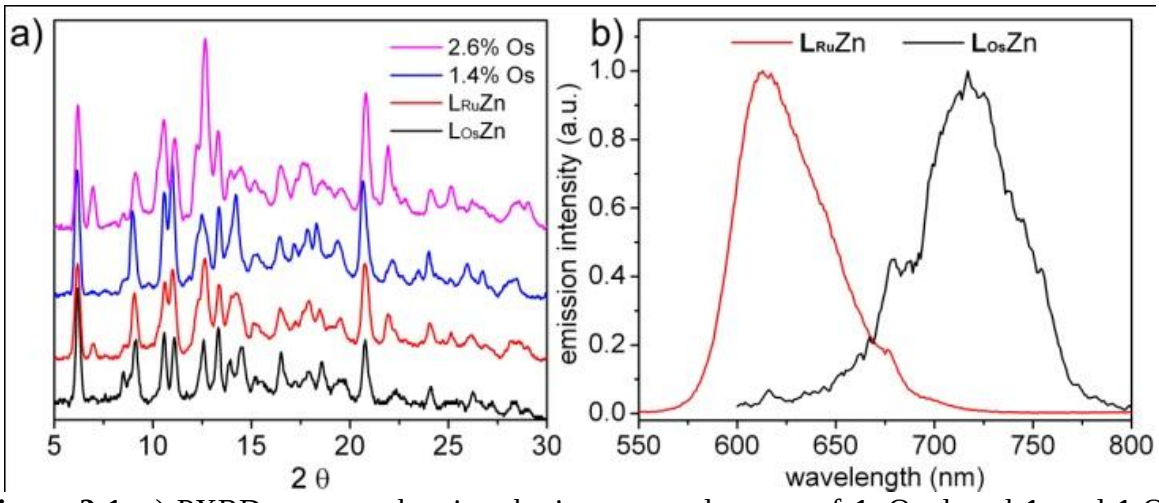

Figure 2-1. a) PXRD patterns showing the isostructural nature of **1**, Os-doped **1**, and **1**-Os MOFs. b) Uncorrected normalized steady-state emission spectra of the **1** and **1**-Os.

In Figure 2-2a are shown emission transients for **1** (620 nm) and **1**-Os (710 nm) MOFs. The decay profiles for the Ru and Os MOFs as well as for the mixed Ru/Os MOFs at varying Os-doping levels were non-exponential and could be satisfactorily fit to biexponential kinetics. The components of the fit are shown in section 2.5.

$$f(t) = Ae^{-(t/\tau_1)} + Be^{-(t/\tau_2)} \qquad \textbf{(eq 2-1)}$$

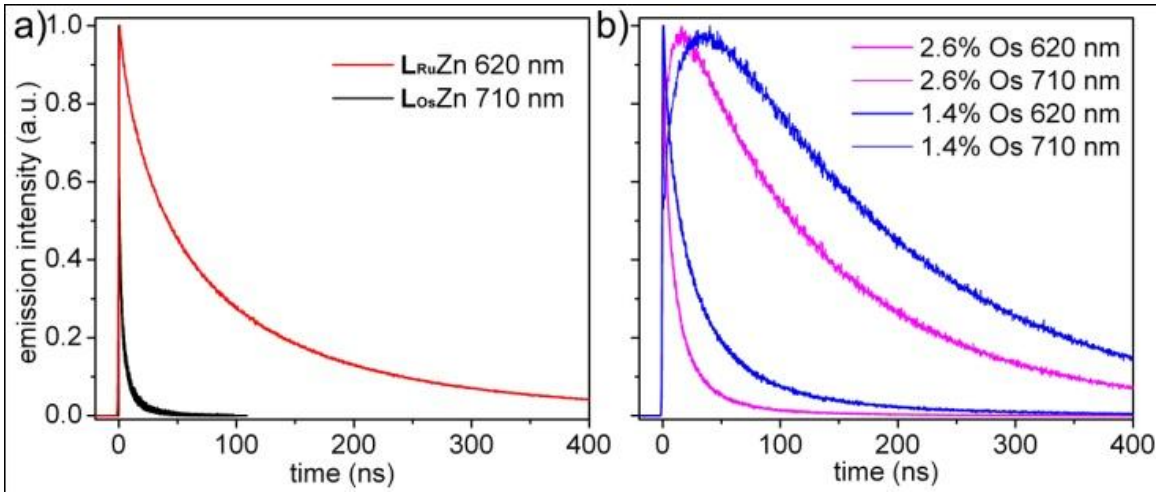

Figure 2-2. a) Transient emission decay profiles for **1** and **1**-Os monitored at 620 nm and 710 nm respectively following two-photon excitation at 850 nm. b) Transients for 1.4 and 2.6 mol% Os-doped **1** MOFs at 620 nm and 710 nm with emission at 620 nm dominated by Ru^{II}* and at 710 nm by Os^{II}*.

Displayed in Figure 2-3 are the averaged transients for a series of Os doped $\mathbf{L_{Ru}}$Zn MOFs collected at 620 nm. Each transient represents an average over multiple sites in multiple crystals. The decays show a qualitative shortening of the liftetime with increasing Os loading, consistent with energy transport to the Os traps. Analysis of the transients shows that they can be reasonably described by a biexponential equation. The results of the fitting are displayed as the black lines in the figure with the components reported in Section 2.5. The fits show a decrease in the lifetime of both the fast and slow time components with increased Os.

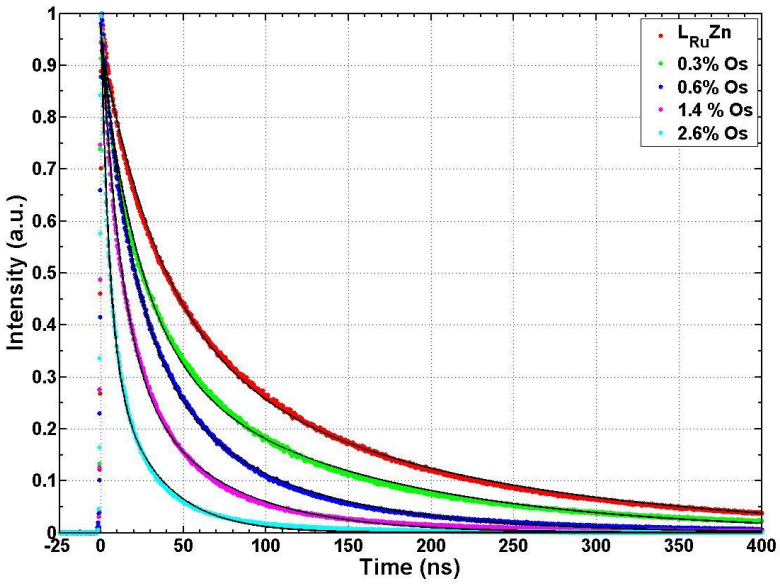

Figure 2-3. Decay of the Ru* emission from Os doped **1** detected at 620 nm. Black lines indicate biexponential fits.

The observation of multiple decay components in the photoluminescence from pure Ru MOFs is contrast to observations in fluid solution, where the luminescence decay is typically single-exponential. Triplet-triplet annihilation could account for the biexponential behavior; however, experiments performed at a series of excitation intensities show no evidence for intensity-dependent effects. The decay kinetics of the Ru^{II}* emission exhibit a clear detection wavelength dependence, with longer wavelengths showing slower decay rates. Time-dependent emission spectra reconstructed from a series of transients obtained at different detection wavelengths show that the biexponential kinetics arise (at least in part) from a time-dependent shift of the emission band. The Ru emission band, which at the earliest observation time has λ_{max}=612 nm, shifts by ≈15-20 nm to the red following photoexcitation. Similar red shifts have been observed, for example, in metal complex derivatized polymers,[10] in electropolymerized thin films,[11] and on surfaces,[12] where they were attributed to inter-site energy transfer to lower energy trap sites that dominate excited

state decay due to their decreased energy gaps. Measurements performed at the red edge of the emission band (≈700 nm) yield a Ru^{II}* lifetime of ≈375 ns. The trap sites in the MOFs may be a result of crystal defects during growth, surface sites, or from lattice distortion upon solvent removal. While the data presented represents observations obtained at single site, examination of other sites within the same crystal, and measurements performed on other crystals produced qualitatively similar results.

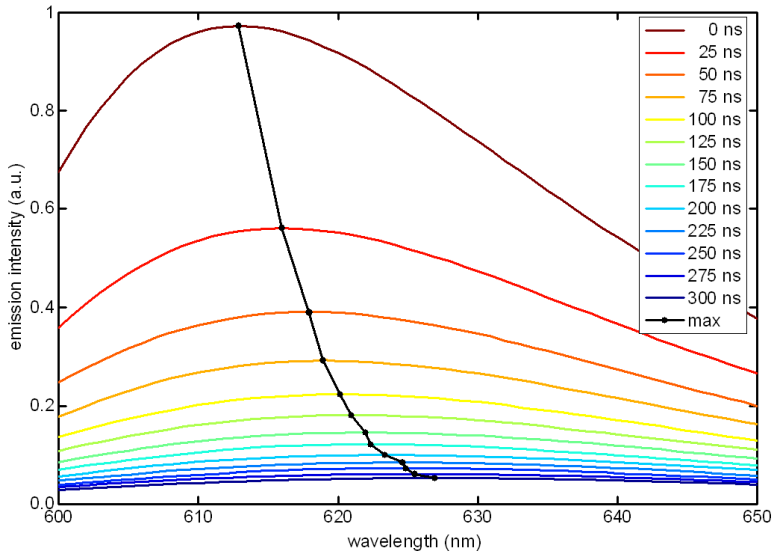

Figure 2-4. Reconstructed **1** time resolved emission spectra demonstrating a dynamic red-shift. Solid color lines indicate stretched Gaussian fits of experimental data. The black line designates the wavelength maximum for each time slice fit.

The dynamic spectral shift is also depicted in Figure 2-5 as the emission decay transients as a function of wavelength. The lower energy emission shows slower decay kinetics as a result of energy transfer to shallow trap sites.

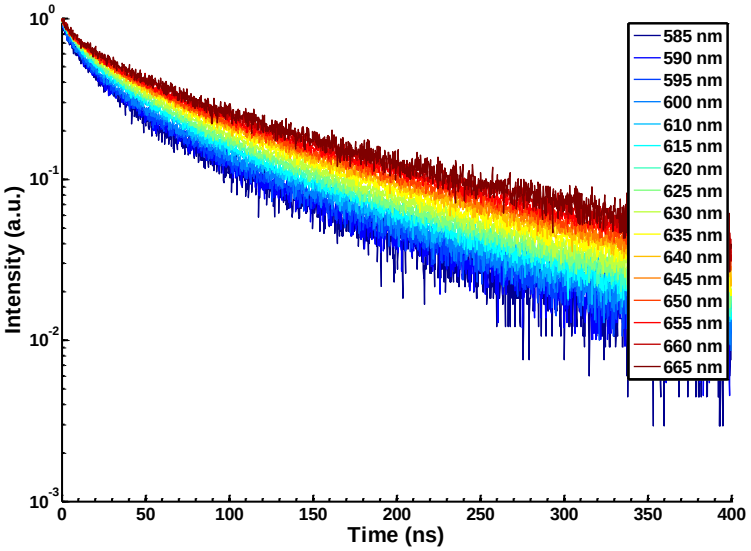

Figure 2-5. Ru emission transients from **1** as a function of wavelength. As the wavelength is shifted from the blue edge (585 nm) to the red edge (665 nm) the lifetime increases.

Direct evidence for site-to-site energy transfer in mixed Ru(II)-Os(II) MOFs had been obtained (Figure 2-2b). First, detection of the Os emission in the mixed Ru(II)-Os(II) systems at 710 nm shows a delayed growth in the first 10-40 ns that is attributable to Ru^{II}*-Ru^{II} energy migration followed by energy transfer to a lower energy Os "trap site". The growth is the fastest for the highest Os-doped sample (2.6 mol%), consistent with a shorter migration distance to the Os^{II} trap, implying that within the initial growth period the excited state makes multiple Ru to Ru hops. In addition, the delayed rise in the Os^{II}* emission at 710 nm coincides with the decay of Ru^{II}* emission detected at 620 nm, which becomes faster as the Os^{II} doping level is increased. Data taken from a series of MOFs with different doping levels show a decrease in both of the decay components of the Ru^{II}* emission with increased doping, consistent with greater quenching of the Ru^{II}* at higher Os^{II} concentrations.

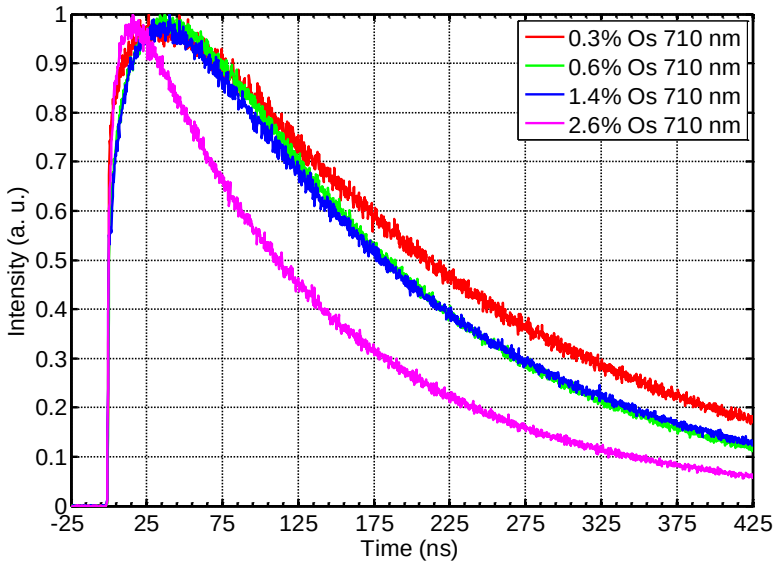

Figure 2-6. Growth and decay of Os* emission from Os doped **1** samples detected at 710 nm.

Estimate of the Ru*-Ru hopping time and transport distance can be made from the dependence of the time-resolved emission data on Os loading, which suggest that transport of the Ru excited state to the Os trap involves multiple Ru*-Ru steps. Since there is a finite diffusion distance of the Ru* excited state during its life time, each Os complex will have a radius (R_Q) in which energy transfer quenching of a Ru* can occur before excited state deactivation. At sufficiently low Os concentrations the average distance between Os^{II} complexes will exceed this quenching radius and the Os^{II} emission transient will be independent of Os loading. At higher Os levels there will be sufficient overlap between the quenching radii of the Os complexes that a given excited state could be quenched by more than one Os trap, resulting in a faster growth and subsequent decay of the Os emission, as well as a faster decay of the Ru^{*II} emission.

The time-resolved data show a dependence on the Os^{II} concentration, even at lowest doping levels studied, suggesting that for doping levels in the range of 0.3 to 0.6 mol% Os the quenching radii are starting to overlap. At 0.3 mol% Os there is approximately one Os per

every 330 complexes and at 0.6 % there is one Os for every 170 complexes, suggesting that there are approximately 200 Ru complexes contained within the quenching radius. The number of hops needed to reach the trap will depend upon connectivity and whether energy migration is isotropic (3D) or restricted to a bilayer (2D). Analysis of the crystal structure indicates that for 3D migration, these 200 complexes surrounding the trap would occupy a sphere of radius ≈35 Å. If energy transport is restricted to a bilayer (i.e. 2D) then the corresponding quenching radius is ≈70 Å. If we consider the migration process to be a random walk, then the number hops needed to traverse this distance is given by: $N_{Ru\text{-}Ru}= (R_Q/\sigma_{EnT})^2$, where σ_{EnT} is the distance traveled per hop. Taking $\sigma_{EnT}\approx 8$ Å, the nearest neighbor distance, we estimate that on average an excited state will make between 20-75 hops during its lifetime, with the lower and upper limits corresponding to 3D and 2D migration, respectively. The estimates for the number of hops and the excited state lifetime (375 ns) further suggest hopping times in the range of 20 ns (for 3D migration) to 5 ns (for 2D migration).

2.2 Energy Transfer Dynamics Theory in MOF-1

The ability to control excitation energy transport pathway dimensionality is of great significance for designing materials for efficient delivery of excitation energy to a target (e.g., a reaction center, reactive crystal surface, or a surface catalyst). Because of this interest, more advanced theoretical modeling has been pursued in collaboration with Beratan et. al.[13] The results provided show the first unified structure-to-function analysis of energy transport MOFs, and they point the way to rational design strategies for excitation energy harvesting and funneling to centers of chemical reactivity and catalysis.

The energy-transfer modeling was performed by a combination of ab initio electronic structure theory with kinetic network modeling. The simulations are in qualitative agreement with the experimental data and the results suggest that energy transport occurs via the Dexter mechanism. Energy migration can effectively be modeled with one dimensional migration pathways because the Dexter coupling between the shortest Ru-Ru distances of ~ 8 Å are 10^{-4} eV and are several orders of magnitude larger than next largest value. The nearest-neighbor hoping rate was treated as a free parameter in fitting the time-dependent luminescent data with the Ru and Os decay rates set to experimentally determined values. The Ru to Ru rate was found to be faster (5-10 ns) than the Ru to Os rate (20-100 ns) and that the Ru to Os rate increases with Os loading.

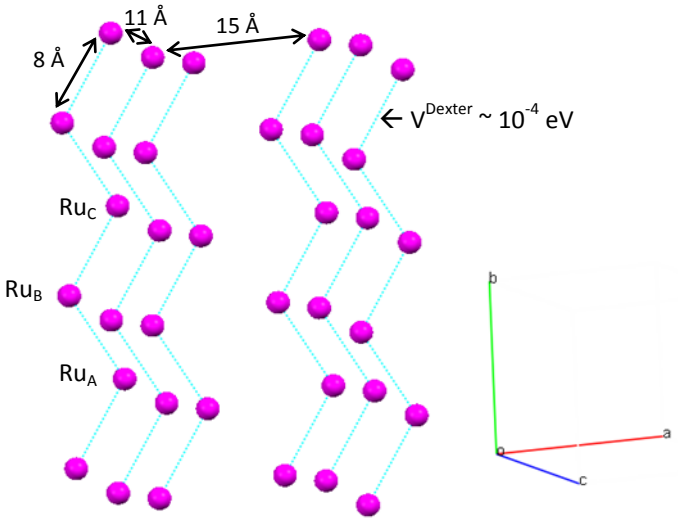

Figure 2-7. Strongest Dexter coupling network (dotted lines denote Dexter couplings) between Ru-pyridyl centered triplet excited states (a, b, and c are crystal axes). For simplicity we show only the Ru atoms of the Ru centers in the MOF. The network is quasi-linear and it involves nearest neighbour Ru centers with Ru-Ru distances of 8 Å, where successive centers along the b direction belong to different bilayers. Each Dexter coupling between neighboring centers along the b axis involves through-space interactions and has magnitude of approximately 10^{-4} eV.[5]

The synthetic tunability of MOFs has allowed for the design of other model systems for studying energy transfer dynamics in well defined crystalline solids to provide new insights into efficient energy migration and transfer pathways in artificial light-harvesting systems.

2.3 Energy Transfer Dynamics in MOF-4

The steady-state emission spectra of **4a**, **4a-Os**, **4b**, and **4b-Os** are shown below. The rigid environment of the oxalate framework leads to a high energy Ru emission with strong vibronic structure compared with $Ru(bpy)_3^{2+}$ in solution. The chromophores are insulated from solvent and therefore the emission is not broadened as in room temperature solution experiments. Both the steady-state and time-resolved emission characteristics of **4a** and **4b** are different but it is unclear if this result is inherent to the structure or a result of the crystallinity of the sample. The effects of defects in the crystal will be examined in more detail later in this section.

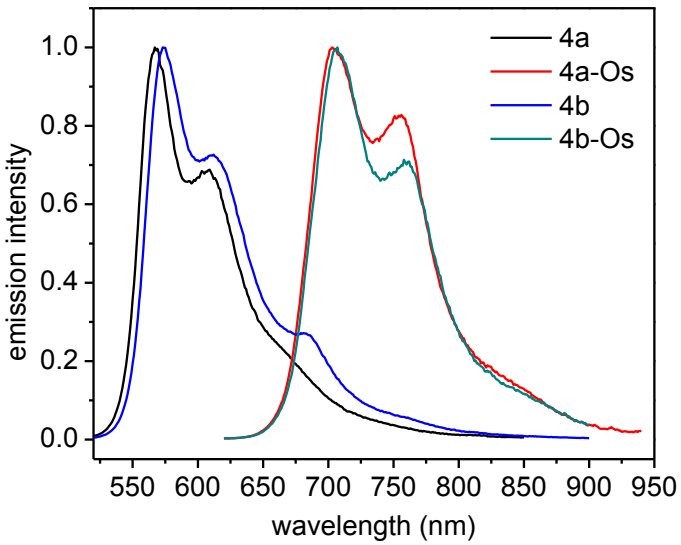

Figure 2-8. Steady-state emission of **4a**, **4b**, **4a-Os**, and **4b-Os** synthesized in an oxygen-free environment.

The emission lifetime of the **4a** can be satisfactorily fit with a single exponential but the lifetime was found to be 1305 ns at 580 nm and 1350 ns at 680 nm which is indicative of energy transfer to shallow trap sites. It is expected that the lifetime could approach 2.5 μs as reported by Hauser et. al. if the crystal were ideal and did not sample defect or surface sites.[14] In those studies the emission decay of isolated chromophores were studied by diluting either Ru or Os complexes to a concentration of about 1% with the remaining sites by occupied by photochemically inert $Zn(bpy)_3^{2+}$. In this way, energy transfer between complexes was virtually eliminated and the emission decays represent an isolated site within the oxalate framework.

If the crystal growth of **4a** occurs in the presence of oxygen the emission lifetime dramatically decreases from 1305 ns to 144 ns. The lifetime cannot be increased by bubble degassing a suspension or heating a solid sample at 80 °C under vacuum. Also, if a sample that was prepared in an oxygen free environment is exposed to air, the lifetime will decrease as oxygen is irreversibly trapped within the material. The decreased lifetime from oxygen quenching was confirmed by measuring singlet oxygen emission from a sample prepared in air while the samples synthesized under nitrogen exhibit no emission from singlet oxygen at ~7850 cm^{-1}.

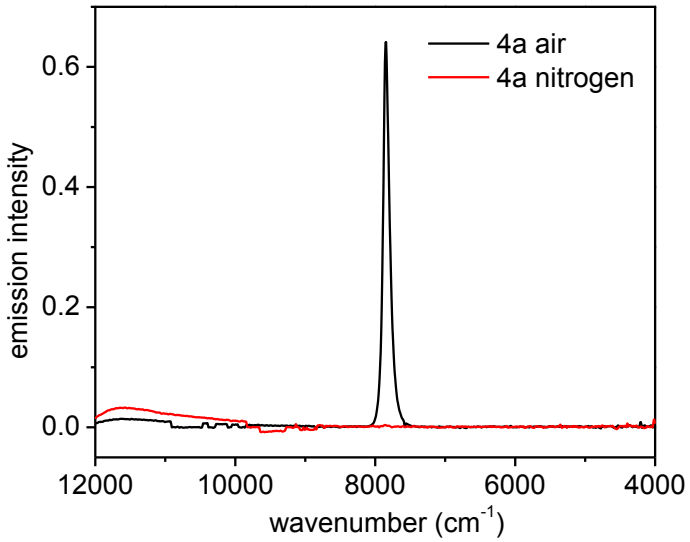

Figure 2-9. Singlet oxygen emission measurements of **4a** synthesized in air and under nitrogen.

The samples prepared by Hauser et. al. demonstrated short lifetimes at high chromophore loadings but as dilutions in $Zn(bpy)_3^{2+}$ the lifetimes increased to 2.5 µs for $Ru(bpy)_3^{2+}$ and 250 ns for $Os(bpy)_3^{2+}$ even though oxygen is trapped within the framework. These long lived excited-states are possible because energy transfer between chromophores is prevented by dilution and therefore quenching by oxygen is minimal. This suggests that the MOFs with high Ru or Os loading can be efficiently quenched by a small amount of oxygen trapped within the MOF because the excited-state can migrate long distances and sample many different environments. The excited-state migration results in an amplified quenching effect by any quenchers present and also suggests utility in light harvesting applications.

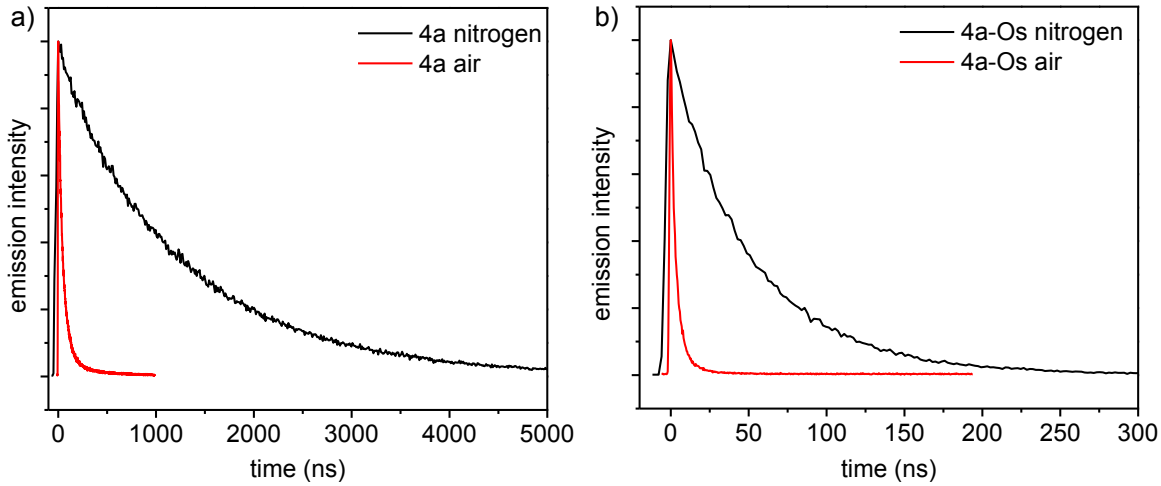

Figure 2-10. Time-resolved emission from a) **4a** and b) **4a-Os** synthesized under nitrogen and in air. The sample prepared in air were argon bubble degassed for 30 minutes prior to measurements demonstrating oxygen is trapped inside the framework.

Remarkably efficient energy transfer quenching is observed in samples of Os doped **4a**. Ru to Os energy transfer dynamics were studied in this system with concentrated chromophores and suggest a different energy transfer mechanism than previously observed. Previous work examined energy transfer from Ru to Os in dilute crystals and as a result of the long distances between photo-active components the dominant mechanism was determined to be Forster. However, energy transfer in samples with >99% $Ru(bpy)_3^{2+}$ are likely governed by a Dexter mechanism which would be expected to be dominant at short distances from work by Beratan et. al.[13]

At low Os doping levels, 1.0% and 0.2%, the extent of Ru emission quenching is large by steady-state emission but the value cannot be quantified because of the difference in quantum yield between Ru and Os. The extent of quenching can be calculated by integrating the emission transients at 580 nm if it is assumed that the Ru to Os energy transfer quenching does not occur faster than the resolution of the instrument (about 1 ns). This calculation actually is a lower limit because quenching that occurs faster than the instrument response will not be observed. The analysis shows that at 0.2% Os loading 78% of the Ru emission is

quenched. At a 1.0% Os loading the amount of Ru quenching increases to 95%. In **4b** the quenching is slightly lower at 65% and 90% for the 0.2% and 1.0% Os loading respectively.

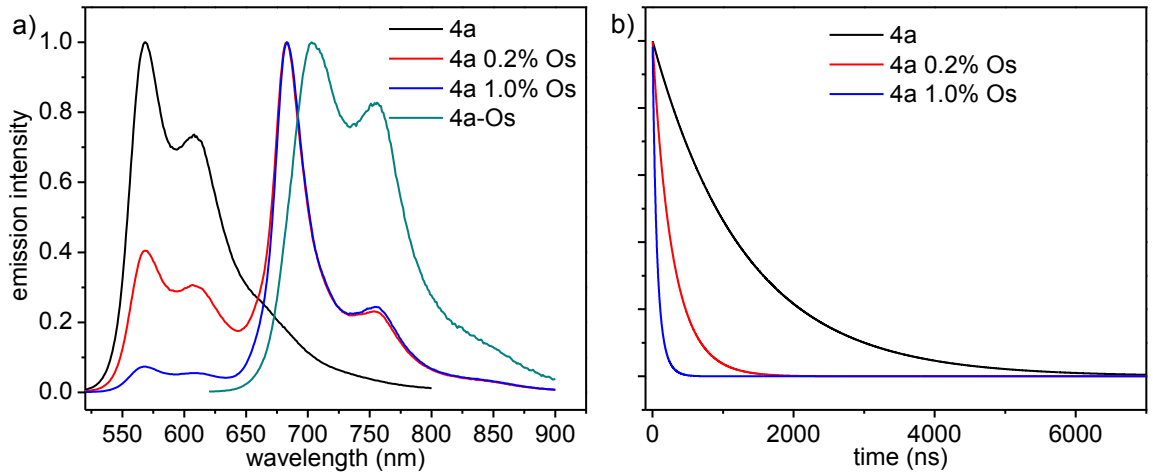

Figure 2-11. a) Steady-state emission from Os doped **4a** and b) time-resolved emission at 580 nm of Os-doped **4a**.

The emission energy of the pure Os MOF, **4a-Os**, shows a significantly lower energy emission than what is observed from the Os emission in the doped samples. This difference in energy occurs from energy transfer to lower energy defect sites. **4a-Os** decays at a faster rate (53 ns lifetime) than what is observed for an isolated Os excited-state in **4a** 1.0% Os (259 ns).

A growth in the Os emission transient, collected at 680 nm, is observed and indicates Ru to Os energy transfer. At 680 the emission is dominated by Os but there is an overlap with the Ru emission tail. The emission at 680 nm at time zero, or right after the laser pulse, could be from Ru sites, Os sites that were excited directly, or Os sites that quickly quenched a Ru excited-state via energy transfer. The first two types, directly excited Ru or Os sites, will decay according to their respective lifetimes and could not lead to a growth in the emission. The emission growth at 680 nm represents an increased Os excited-state population that occurred from excitation of a Ru site and energy transfer to a lower energy Os site. With 0.2% Os doping the maximum 680 nm emission is not observed until ~200 ns after the laser

pulse. With 1.0% Os doping the maximum emission occurs ~100 ns after the laser pulse. The decreased delay time is a result of the shorter average excited-state transport distance to find an Os trap.

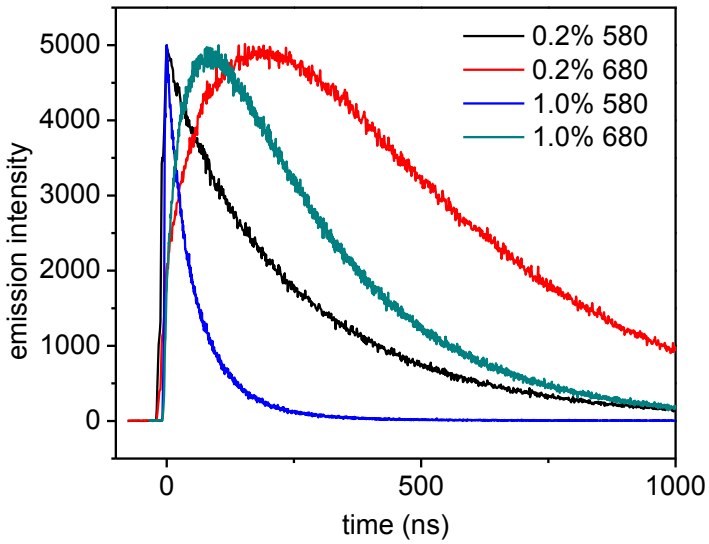

Figure 2-12. Time-resolved emission of Os-doped **4a** at 580 and 680 nm which are dominated by Ru and Os emission respectively.

The extent of quenching is so large in the 1.0% Os sample that after 500 ns the Ru emission is virtually gone and all that remains is the Os emission. Under these conditions the Os excited-states are isolated from each other and decay with a single-exponential lifetime of 257 ns. This lifetime is in agreement with what was observed previously with isolated $Os(bpy)_3^{2+}$ in $Zn(bpy)_3^{2+}$.[14]

The emission properties of **4b** are slightly different than what is observed for **4a** but it is challenging to distinguish between the effect of the structural differences and the crystallinity of the sample. The lifetime of **4b** at 580 nm is 760 ns compared to 1305 ns for **4a**. The steady-state emission of **4b** is also lower in energy that **4a**, as shown in Figure 2-9. The extent of quenching in Os-doped **4b** can be calculated as before with 65% and 90% quenching for the 0.2% and 1.0% Os loading respectively. Direct evidence of energy transfer is also observed in **4b** with a growth in the Os emission transient at 680 nm.

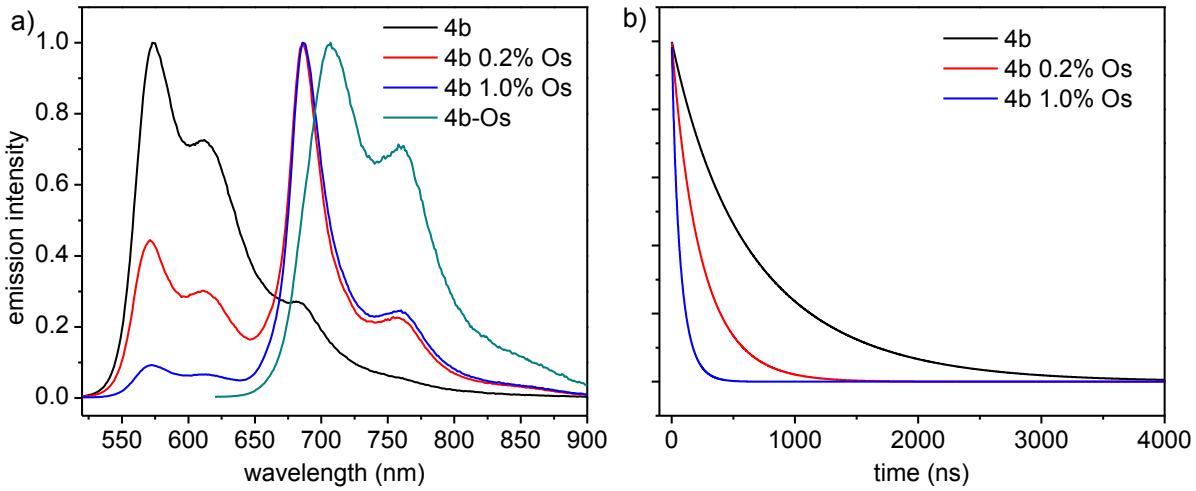

Figure 2-13. a) Steady-state emission from Os doped **4b** and b) time-resolved emission at 580 nm of Os-doped **4b**.

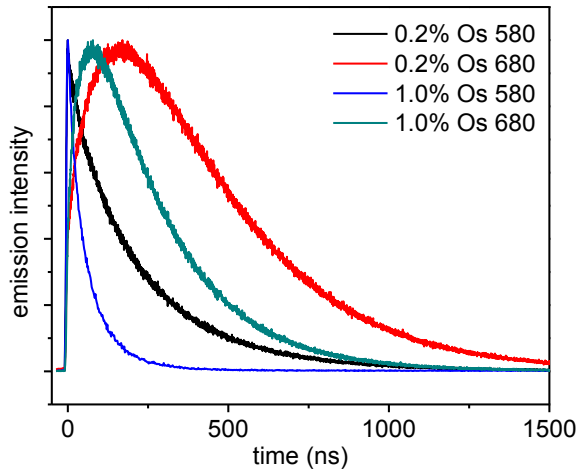

Figure 2-14. Time-resolved emission of Os-doped **4b** at 580 and 680 nm which are dominated by Ru and Os emission respectively.

Table 2-1. Average lifetime of various Os doping levels of **4a** and **4b** under nitrogen and in air.

Sample	**4a** average lifetime	**4b** average lifetime
Ru N_2	1305	760
Ru air	144	-
Os N_2	53	49
Os air	5	-
0.2% Os	306	260
1.0% Os	81	80

4a, **4b**, Os doped **4a**, and Os doped **4b** were measured at 580 nm. **4a-Os** and **4b-Os** were measured at 710 nm. Samples **4a** and **4a-Os** prepared under N_2 were fit with a single-

exponential while the other samples were fit with a biexponential and reported as an average lifetime. Samples labeled air were synthesized in the presence of oxygen and then argon bubble degassed for 30 minutes prior to measurement.

The most revealing data on the effect of the different oxalate frameworks of **4a** and **4b** can be observed in the 680 nm transients of the 1.0% Os doped samples. Because of the very high efficiency of Ru to Os quenching after 500 ns the Ru emission is virtually eliminated. The only emission that remains is from Os sites that are sufficiently separated from each other that Os to Os energy transfer is unlikely. The higher energy Ru sites do not quench the Os excited state and therefore it decays in a nearly defect free environment as shown by the difference in steady-state emission of the 1.0% Os sample compared to the pure Os sample. The emission decays with a single exponential lifetime which is also indicative of the highly uniform environment. The intrinsic Os emission lifetime is 259 ns in **4a** and 228 ns in **4b** which suggests the higher emission energy and longer lifetime of **4a** is a result of the framework geometry and not increased defects in **4b**.

A modified Stern-Volmer lifetime analysis was performed on the Os-doped MOFs to determine the relative rates of energy transfer. The relative rate of energy transfer can be compared between different structures by plotting the ratio of the Ru only lifetime, τ_0, vs the Ru lifetime, τ, at a given Os doping level. The increased rate of energy transfer in the oxalate frameworks compared to previous systems may be a result of the dimensionality of energy transfer. In MOF-1, energy transfer occurred along a 1-D chain as a result of 3 orders of magnitude higher dexter coupling within the chain compared to alternate energy transfer pathways. In the oxalate framework however, each chromophore is surrounded by 6 nearest neighbors each at a distance of 9.4 Å. This 3-dimensional energy transfer network allows for sampling a larger number of sites within the crystal.

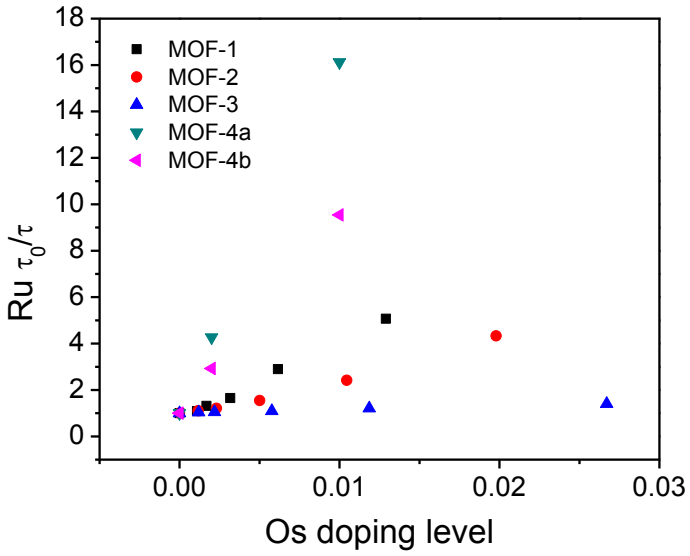

Figure 2-15. Summary of Os-doped MOFs as a function of change in Ru emission lifetime vs mole fraction Os.

2.3.1 Emission Spectral Fitting

The rigid environment of the oxalate framework leads to a high energy Ru emission with strong vibronic structure. The chromophores are insulated from solvent and therefore the emission is not broadened as in room temperature solution experiments. In fact, the emission spectral fitting shows similarity to what is observed for $Ru(bpy)_3^{2+}$ in a frozen solution at 77 K. Franck-Condon spectral fitting analysis can give insight into the distortion of the chromophore between the excited state and ground state and therefore a reorganizational energy can be calculated which is an important parameter in energy transfer modeling.

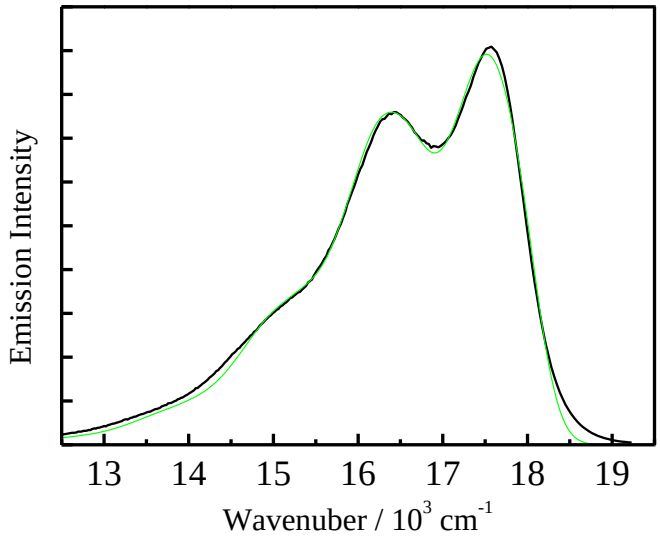

Figure 2-16. Steady-state emission of **4a** (black) and simulated emission spectra (green) at RT.

Table 2-2. Spectral fitting parameters.

	E_0 / cm^{-1}	$\tilde{\nu}_{1/2}$ / cm^{-1}	$\hbar\tilde{\nu}_M$ / cm^{-1}	$\hbar\tilde{\nu}_L$ / cm^{-1}	S_M	S_L	r
4a	17896	612	1290	386	0.98	1.49	0.99846
4a-Os	14191	864	953		1.09		0.99803
4a 1% Os	14607	626	1400	687	0.42	0.36	0.99755
4b	17781	717	1283	340	0.97	1.70	0.99928
4b-Os	14137	899	998		0.98		0.99580
4b 1% Os	14530	632	1403	680	0.42	0.38	0.99727
$[Ru(bpy)_3](PF_6)_2$ 77K[15]	17390 ± 50	625 ± 95	1380 ± 22	400 ± 12	1.00 ± 0.03	1.20 ± 0.18	
$[Os(bpy)_3](PF_6)_2$ 77K[15]	14175 ± 23	635 ± 44	1325 ± 20	400 ± 10	0.53 ± 0.02	0.87 ± 0.08	

Franck-Condon analysis is the spectral fitting analysis which evaluates the electronic structures and the vibrational characters of the complex in the excited-state, given in equation 2-2.[15,16]

$$I(\tilde{\nu}) = \sum_{\nu_M=0}^{\infty}\sum_{\nu_L=0}^{\infty}\left(\frac{\tilde{\nu}_{00}-\nu_M\tilde{\nu}_M-\nu_L\tilde{\nu}_L}{\tilde{\nu}_{00}}\right)^4\left(\frac{S_M{}^{\nu_M}}{\nu_M!}\right)\left(\frac{S_L{}^{\nu_L}}{\nu_L!}\right)\exp\left[-4\ln 2\left(\frac{\tilde{\nu}-\tilde{\nu}_{00}+\nu_M\tilde{\nu}_M+\nu_L\tilde{\nu}_L}{\tilde{\nu}_{\frac{1}{2}}}\right)^2\right]$$

(**eq 2-2**)

where $I(\tilde{\nu})$ is the emission intensity at the energy in wavenumber (cm^{-1}), relative to the intensity of the 0→0 transition. $\tilde{\nu}_{00}$ is the energy gap between the zeroth vibrational levels of the ground- and excited-states. $\tilde{\nu}_M$ and $\tilde{\nu}_L$ are the quantum spacings for two accepting averaged vibrational modes of medium and low frequency, respectively. S_M and S_L are the Huang-Rhys factors reflecting nuclear distortion along the medium- and low-frequency quantum modes. $\tilde{\nu}_{1/2}$ is the full width at half-maximum (fwhm) for individual vibronic lines, and they include contributions from solvent librations and low-frequency molecular modes treated classically.

The photon numbers of the emission spectra were corrected in wavenumber scale by using equation $I(\tilde{\nu}) = I(\lambda)$ x λ^2 and, then, the parameters $\tilde{\nu}_{00}$, S_M, S_L, $\tilde{\nu}_M$, $\tilde{\nu}_L$, $\tilde{\nu}_{1/2}$ were optimized with a least squares minimization routine using a Generalized Reduced Gradient (GRG2) algorithm. The summation was carried out over 11 levels of vibration ($\nu_M = 0 \rightarrow 10$).

Usually the emission spectra of ruthenium(II) polypyridal complexes at room temperature can be satisfactorily expressed by one-mode Franck-Condon analysis, given in eq 2-3. This is a simplified modulation of two-mode Franck-Condon analysis implementing one acceptor vibration mode in the excited-state fitting, due to their broad and structureless spectra.

$$I(\tilde{\nu}) = \sum_{\nu_M=0}^{\infty} \left(\frac{E_0 - \nu_M \hbar\omega_M}{E_0}\right)^3 \left(\frac{S_M{}^{\nu_M}}{\nu_M!}\right) \exp\left[-4\ln 2 \left(\frac{\tilde{\nu} - E_0 + \nu_M \hbar\omega_M}{\tilde{\nu}_{1/2}}\right)^2\right] \qquad \textbf{(eq 2-3)}$$

The emission spectra of **4a** or **4b** could not reproduced by using one-mode Franck-Condon analysis (eq 2-3) because of the narrow emission spectrum of the MOFs. Instead, two-mode Franck-Condon analysis (eq 2-2) could reproduce the observed emission spectrum

as shown in Figure 2-9, and the obtained values were quite similar to those of the ruthenium(II) complex in a frozen glass matrix.

The Frank Condon spectral fitting analysis calculated the excited-state reorganizational energy to be 0.25 eV by equation 2-4. As expected, vibronic structure is also observed with **4a**-Os which is similar to $Os(bpy)_3^{2+}$ in a frozen solution.

$$\lambda = \frac{(\tilde{\nu}_{1/2})^2}{16 k_B T \ln 2} + S_M \hbar\omega_M + S_L \hbar\omega_L \qquad \textbf{(eq 2-4)}$$

Table 2-3. Biexponential fit parameters and average lifetime for Os-doped **1**.

1-xOs	A_1	τ_1	A_2	τ_2	$< \tau >$ Lifetime (ns)
0	27.1	239.9	72.9	663.4	613
0.0011	28.3	205.2	71.7	611	564
0.0017	30.1	190.4	69.9	510.7	466
0.0032	26.1	151.1	73.9	400.3	371
0.0062	33.5	79.8	66.5	234	211
0.0129	34	45	66	134	121
1.00	19.7	5.04	80.3	15.63	15

Table 2-4. Biexponential fit parameters and average lifetime for Os-doped **2**.

2-xOs	A_1	τ_1	A_2	τ_2	$< \tau >$ Lifetime (ns)
0	22.9	453	77.1	1178	1104
0.0012	15.1	312	84.9	1032	995
0.0023	15.8	286	84.2	947	912
0.0050	22.7	276	77.3	761	714
0.0105	15.6	122	84.4	472	456
0.0198	14.4	58	85.6	262	255
1.00	15.8	10	84.2	31	30

Table 2-5. Biexponential fit parameters and average lifetime for Os-doped **3**.

3-xOs	A_1	τ_1	A_2	τ_2	$< \tau >$ Lifetime (ns)
0	15	43.8	85	140.9	136
0.001	16.7	41.6	83.3	136.4	131
0.002	19.3	44.2	80.7	135.6	129
0.004	20.5	41	79.5	130.8	124
0.009	21.7	36.4	78.3	118.6	112
0.017	26.8	32.8	73.2	104.3	97

Table 2-6. Biexponential fit parameters and average lifetime for Os-doped **4a**.

4a-xOs	A_1	τ_1	A_2	τ_2	$< \tau >$ Lifetime (ns)
0.00					1305
0.002	15.2	134	84.8	319	306
0.01	53.8	44	46.2	99.9	81
1.00					53

Table 2-7. Biexponential fit parameters and average lifetime for Os-doped **4b**.

4b-xOs	A_1	τ_1	A_2	τ_2	$< \tau >$ Lifetime (ns)
0.00	20	285	80	802	760
0.002	15.6	106	84.4	271	260
0.01	26.3	31.4	73.7	85.9	79.6
1.00	13.8	19	86.2	50.3	48.5

2.4 Concluding Remarks

Isomorphous metal-organic frameworks based on photo-active Ru(II) or Os(II) polypyridal complex building blocks with characteristic strong visible light absorption, and long-lived, high-energy excited states were designed and synthesized to study the classic Ru to Os energy transfer process for applications in light-harvesting with supramolecular assemblies. The crystalline nature of MOFs allows for determination of the distances between metal centers by X-ray diffraction which leads to more precise modelling of energy transfer rates than in amorphous systems. The Os doping level was systematically varied to experimentally determine relative rates of energy migration. Studies of oxalate frameworks with the photo-active component, $Ru(bpy)_3^{2+}$, trapped tightly inside the pores results in an emission with vibronic structure and show even more efficient $Ru(bpy)_3^{2+}$ excited state quenching than previously observed. Efficient long-range energy migration will be exploited and coupled to electron transfer for application in light-harvesting and amplified quenching in the following chapters.

2.5 Experimental Section

For the data reported in section 2.1 MOF emission transients were collected on a coupled microscope-time correlated single photon collection system. Two-photon absorption at 850 nm from an ultrafast mode-locked Ti:Sapphire laser was used for direct MLCT excitation at Ru^{II}. The excitation beam is reflected off a dichroic mirror (R: 850-1100 nm, T: 450-780 nm) into the objective (Olympus MSPlan 50x, NA 0.8) of an inverted microscope. Backscattered emission collected by the objective is transmitted through the beamsplitter, focused onto the entrance slit of a monochromator and detected by a photomultiplier tube operated in a time correlated single photon counting scheme. The diameter of the excitation region is estimated to be ~350 nm. The instrument response function of the system is ~200 ps.

MOF samples were washed with ethanol, vacuum degassed, and flame-sealed into capillary tubes under nitrogen. It was determined that the removal of solvent had a large negative influence of the photophysical properties of the material as a result of crystal deformation. Later experiments were performed on suspensions of crystals in either acetonitrile or ethanol. Emission lifetimes on the MOF samples were collected on a coupled microscope time correlated single photon collection system described above. Ru emission transients for all synthesized MOFs display biexponential kinetics suggesting the presence of different local environments within each structure. Furthermore, due to the inherent localized excitation region (~350 nm) various sites within multiple crystals were measured. In fact, variations in lifetimes were observed. Therefore, reported lifetimes were averaged from data collected at a series of locations in multiple crystals. The error bars represent the range of values obtained from the different individual sites.

Table 2-8. Lifetimes of Os doped **1** with varying amounts of the $\mathbf{L1_{Os}}$ complex.[a]

sample	mol %Os	amplitude$_1$	τ_1 (ns)	amplitude$_2$	τ_2 (ns)
1	0	0.41 ± 0.03	171 ± 30	0.59 ± 0.03	38 ± 7
$\mathbf{L_{0.3Os}}$Zn	0.3	0.38 ± 0.04	135 ± 31	0.62 ± 0.04	25 ± 6
$\mathbf{L_{0.6Os}}$Zn	0.6	0.37 ± 0.03	83 ± 9	0.63 ± 0.03	21 ± 3
$\mathbf{L_{1.4Os}}$Zn	1.4	0.36 ± 0.03	57 ± 10	0.64 ± 0.03	13 ± 2
$\mathbf{L_{2.6Os}}$Zn	2.6	0.37 ± 0.03	29 ± 4	0.63 ± 0.03	5 ± 1
1-Os	100	0.40 ± 0.02	8 ± 1	0.60 ± 0.02	1 ± 0.3

[a]Data were taken from multiple crystals in each sample. Lifetime measurements of **1** and doped samples were taken at 620 nm and **1**-Os MOF at 710 nm.

For emission data reported in section 2.3 the MOF particles were measured as a suspension in order to avoid creating defects by pulling vacuum. After crystal growth for **1**, **2**, and **3** the MOF particles were washed three times with methanol and then three times with acetonitrile. The samples were argon bubble degassed for 30 minutes prior to taking measurements to remove any oxygen. Solvent evaporation, which would result in concentration changes, was prevented by pre-saturating the argon with MeCN by passing argon through a fritted gas washing bubbler before the gas manifold. Samples of **4a** and **4b** were synthesized under nitrogen and worked up inside a glove box. Magnetic stirring was used to keep the particles suspended so that the emission signal did not decrease from settling of the crystals. Long pass filters were used to eliminate light scattering artifacts.

2.6 References

1. Krausz, E.; Ferguson, J., THE SPECTROSCOPY OF THE RU(BPY)3 2+ SYSTEM. *Progress in Inorganic Chemistry* 1989, 37, 293-390.

2. Krausz, E.; Riesen, H., Developments in laser selective spectroscopy and photophysics of d(6) metal-(di-imine) complexes. *Coordination Chemistry Reviews* 1997, 159, 9-40.

3. Yersin, H.; Braun, D., LOCALIZATION IN EXCITED-STATES OF MOLECULES - APPLICATION TO RU(BPY)3 2+. *Coordination Chemistry Reviews* 1991, 111, 39-46.

4. Komada, Y.; Yamauchi, S.; Hirota, N., PHOSPHORESCENCE PROPERTIES OF LOWER EMITTING STATES OF RU(BPY)3 (CLO4)2. *Journal of Physical Chemistry* 1988, 92, 6511-6518.

5. Ikeda, N.; Yoshimura, A.; Tsushima, M.; Ohno, T., Hopping and annihilation of (MLCT)-M-3 in the crystalline solid of Ru(bpy)(3) X-2 (X = Cl-, ClO4- and PF6-). *Journal of Physical Chemistry A* 2000, 104, 6158-6164.

6. Ohno, T.; Nozaki, K.; Nakamura, M.; Motojima, Y.; Tsushima, M.; Ikeda, N., Rates of electronic excitation hopping in anisotropic ionic crystals of Ru(2,2 '-bipyridine)(3) X-2 (X = ClO4-, PF6-, SbF6-); Monte Carlo simulation of single- and multi-exponential emission decays. *Inorganic Chemistry* 2007, 46, 8859-8870.

7. Tsushima, M.; Ikeda, N.; Nozaki, K.; Ohno, T., Fast Energy Transfer of Charge-Transfer Triplet Excited State (3CT) of [Ru(bpy)3](PF6)2 to Os2+ at Short Distances in the Crystal. *J. Phys. Chem. A* 2000, 104, 5176-5180.

8. Breu, J.; Kratzer, C.; Yersin, H., Crystal Engineering as a Tool for Directed Radiationless Energy Transfer in Layered {Λ-[Ru(bpy)3]Δ-[Os(bpy)3]}(PF6)4. *J. Am. Chem. Soc.* 2000, 122, 2548-2555.

9. Fetterolf, M. L.; Offen, H. W., Luminescence of ruthenium(II) and osmium(II) polypyridyls in acetonitrile at high pressures. *J. Phys. Chem.* 1985, 89, 3320-3.

10. Fleming, C. N.; Jang, P.; Meyer, T. J.; Papanikolas, J. M., Energy Migration Dynamics in a Ru(II)- and Os(II)-Based Antenna Polymer Embedded in a Disordered, Rigid Medium. *J. Phys. Chem. B* 2004, 108, 2205-2209.

11. Devenney, M.; Worl, L. A.; Gould, S.; Guadalupe, A.; Sullivan, B. P.; Caspar, J. V.; Leasure, R. L.; Gardner, J. R.; Meyer, T. J., Excited state interactions in electropolymerized thin films of Ru-II, Os-II, and Zn-II polypyridyl complexes. *Journal of Physical Chemistry A* 1997, 101, 4535-4540.

12. Trammell, S. A.; Yang, P.; Sykora, M.; Fleming, C. N.; Odobel, F.; Meyer, T. J., Molecular energy transfer across oxide surfaces. *Journal of Physical Chemistry B* 2001, 105, 8895-8904.

13. Hu, X.; Van Rynbach, A.; Beratan, D. N.; Mehl, *B. P.*; *Ke*nt, *C. A.*; *Papan*ikolas, *J. M.*; *Meyer, T.* J.; *Skourtis, S.* S.; *Lin,* W., A Theory for Triplet Excitation Energy Harvesting in Metal-Organic Framework Materials. in preparation.

14. von Arx, M. E.; Burattini, E.; Hauser, A.; van Pieterson, L.; Pellaux, R.; Decurtins, S., Luminescence and energy transfer of Ru(bpy)(3) (2+), Cr(ox)(3) (3-), and Os(bpy)(3) (2+) in three-dimensional oxalato-networks. *Journal of Physical Chemistry A* 2000, 104, 883-893.

15. Caspar, J. V.; Westmoreland, T. D.; Allen, G. H.; Bradley, P. G.; Meyer, T. J.; Woodruff, W. H., MOLECULAR AND ELECTRONIC-STRUCTURE IN THE METAL-TO-LIGAND CHARGE-TRANSFER EXCITED-STATES OF D6 TRANSITION-METAL COMPLEXES IN SOLUTION. *Journal of the American Chemical Society* 1984, 106, 3492-3500.

16. Allen, G. H.; White, R. P.; Rillema, D. P.; Meyer, T. J., SYNTHETIC CONTROL OF EXCITED-STATE PROPERTIES - TRIS-CHELATE COMPLEXES CONTAINING THE LIGANDS 2,2'-BIPYRAZINE, 2,2'-BIPYRIDINE, AND 2,2'-BIPYRIMIDINE. *Journal of the American Chemical Society* 1984, 106, 2613-2620.

CHAPTER 3

INTERFACIAL ELECTRON TRANSFER TO REDOX ACTIVE MOLECULES AT THE CRYSTAL SOLUTION INTERFACE

3. 1 Nano/Microscale MOFs for Light Harvesting

Nano/microscale MOFs have attracted recent interest due to the potential advantages over bulk phases of MOFs in biomedical and other applications.[1-5] Crystal size also plays an important role in light harvesting. The crystal must be able to absorb a high fraction of the incident light but be small enough so that the majority of excited states reach the surface for electron transfer before the excited state decays. In order to determine the optimal size of a light-harvesting crystal an estimate of the transmission and absorptance of **2** as a function of pathlength was performed by using the Beer Lambert law, equation 3-1. An extinction coefficient of 15,000 $M^{-1}cm^{-1}$ was used, which is an upper limit for a MLCT transition. An effective concentration was determined to be 1.46 M based upon the volume of the unit cell calculated from XRD. This analysis shows that approximately 150 nm of penetration is required to absorb half of the incident light, while 90% is absorbed around 500 nm. It should be noted that this model does not include reflectance of light off the crystal surface which would change initial light intensity but not the ratio of absorbed vs. transmitted light.

$$Transmission = 10^{-\varepsilon lc} \qquad \textbf{(eq 3-1)}$$

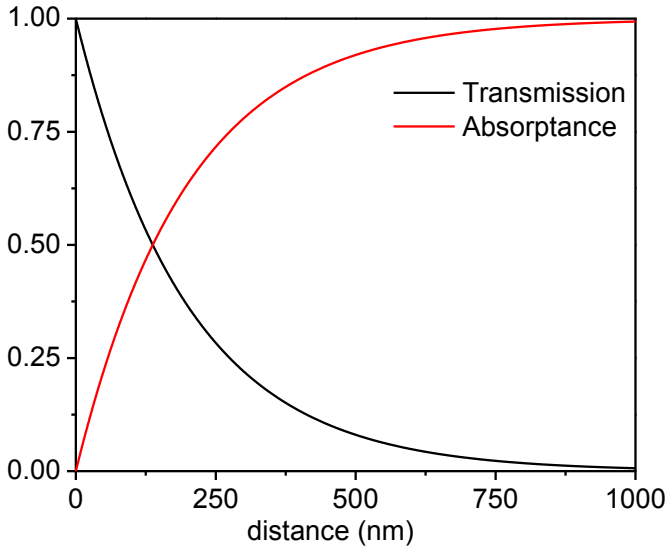

Figure 3-1. Transmission and absorptance of **2** as a function of distance calculated from the Beer-Lambert law with ε=15,000 $M^{-1}cm^{-1}$ and c=1.46 M.

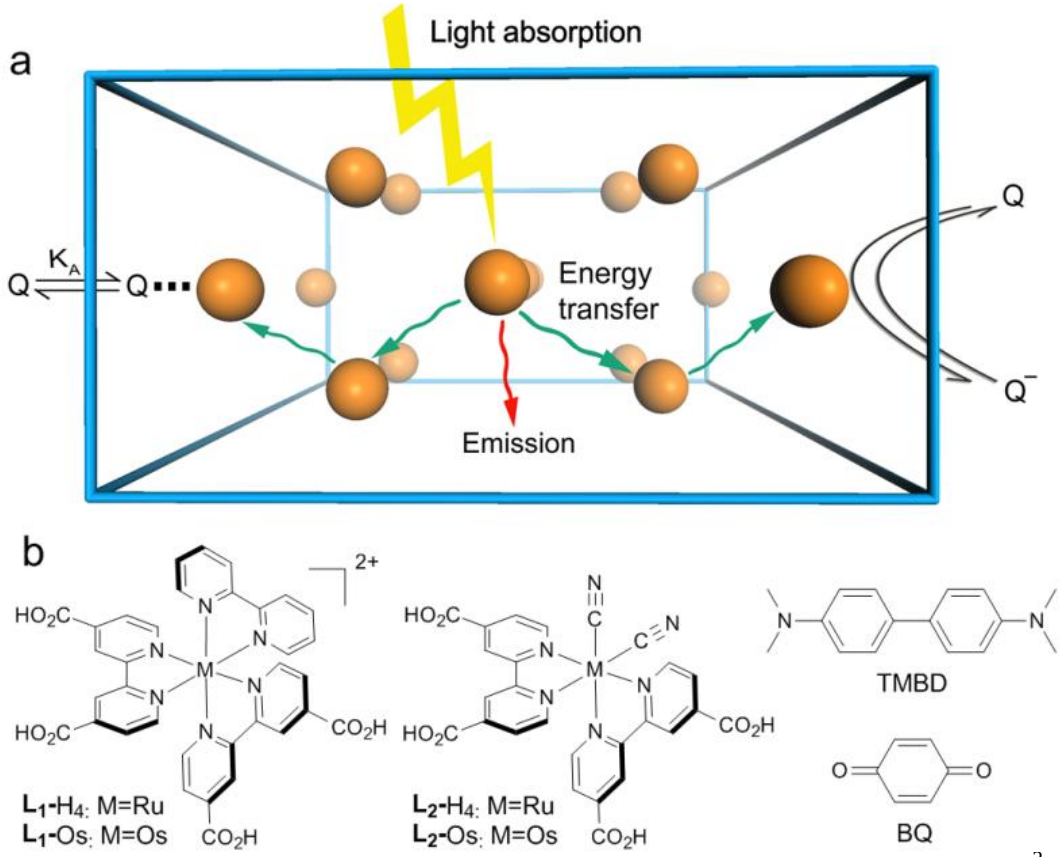

Figure 3-2. a) Schematic representation of a light-harvesting MOF microcrystal. The ^{3}MLCT excited states undergo rapid intra-framework energy migration to carry out electron transfer quenching at the MOF/solution interface. b) Chemical structures of the photo-active MOF building blocks and reductive (TMBD) and oxidative (BQ) quenchers.

In order to utilize the antenna effect illustrated in the previous chapter, redox active quenchers were introduced to suspensions of microcrystals of **1** and **2** to examine light-harvesting characteristics. Microcrystals of **1** and **2** were prepared by procedures reported in Chapter 1. SEM images showed that disk-shaped particles of **1** were ~100 nm in thickness and ~3 μm in diameter. Needle-like microcrystals of **2** fractured upon drying, but are ~750 nm in diameter and >10 μm in length. This suggests that the crystals synthesized in this work are in the proper size regime such that individual crystals absorb the majority of light but are not so large such that the core is inactive.

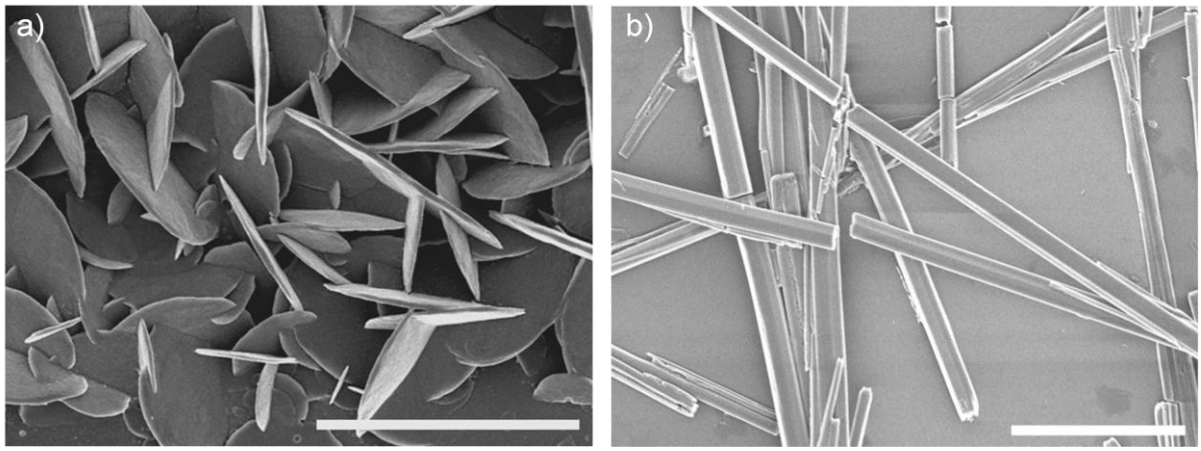

Figure 3-3. (a) SEM image of disk-like microcrystals of **1**. (b) SEM image of rod-like microcrystals of **2**. Scale bars represent 5 μm.

The scattering of visible light, as a result of the MOF dimensionality, made traditional UV-vis absorbance measurements of little value. MOF absorptance values were calculated from equation 2. Both transmission and reflectance measurements were required in order for accurate characterization. The samples were prepared as uniform films of crystals held between glass slides. An integrating sphere attachment was used to capture reflected light. Characteristic MLCT absorption bands dominate visible spectra as they do in solution. In the **1**-Os and **2**-Os, characteristic low energy, low absorptivity S → T MLCT absorptions appear

at 550-750 nm with strong overlap with Ru(II)* MOF emissions. This overlap is an important feature to allow for Ru → Os energy transfer. The emission measurements were performed on magnetically stirred, degassed suspensions in MeCN.

$$Absorptance = 1 - Transmission - Reflectance \quad \textbf{(eq 3-2)}$$

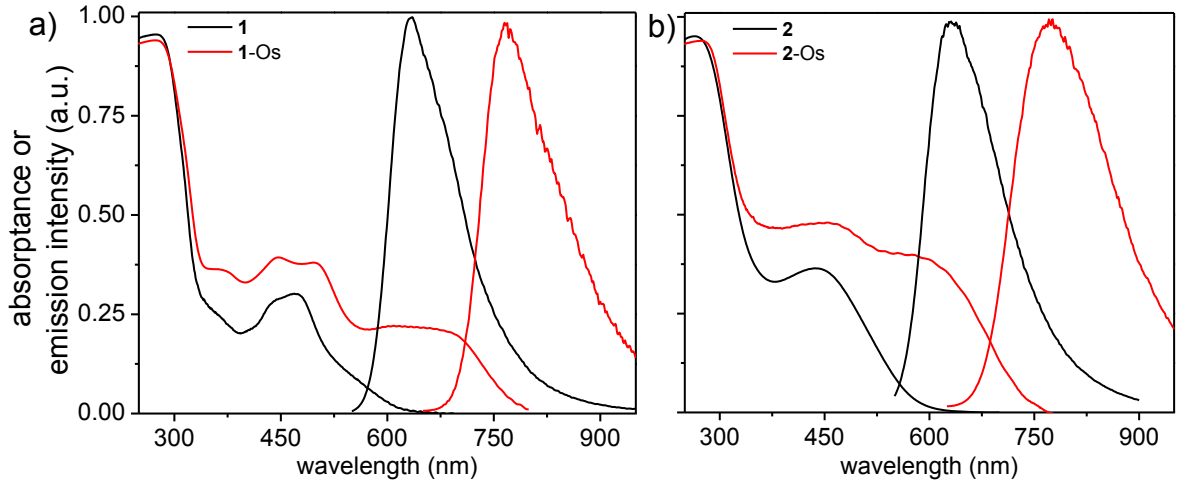

Figure 3-4. Absorptance and emission of (a) **1** and **1**-Os and (b) **2** and **2**-Os.

Os complexes $\mathbf{L1_{Os}}$–H_4 and $\mathbf{L2_{Os}}$–H_4 could be doped into microcrystals of **1** and **2**. The mixed Ru/Os MOFs are isomorphous to Ru-only MOFs as shown by PXRD.

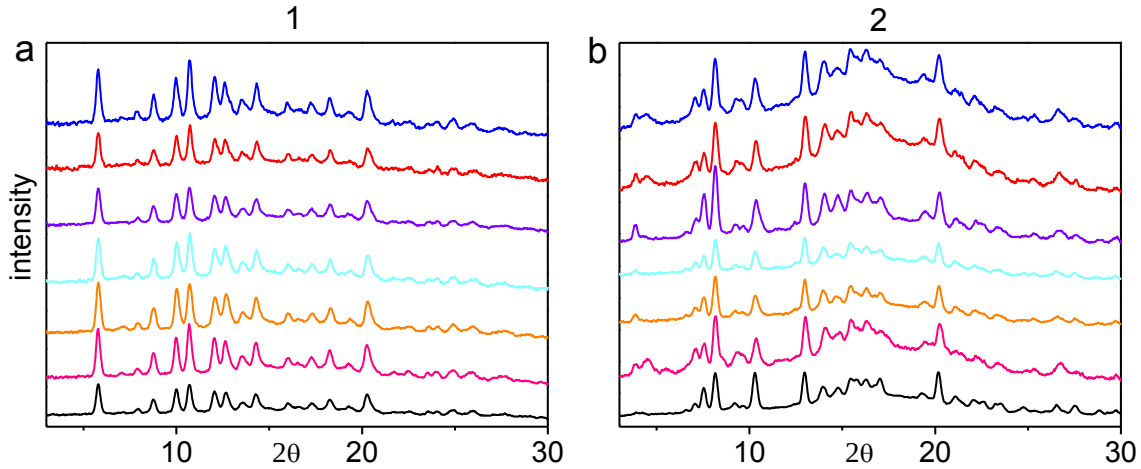

Figure 3-5. a) PXRD patterns of microcrystals of **1** with various Os doping levels: the mol% Os (from top to bottom) is 0.0, 0.11, 0.17, 0.32, 0.61, 1.29, and 100. b) PXRD patterns of **2** with various Os doping levels: the mol% Os (from top to bottom) is 0.0, 0.12, 0.23, 0.50, 1.04, 1.98, and 100.

3.2 Emission Quenching of 1 and 2 by Interfacial Electron Transfer

The MOF emission decays without added quenchers were satisfactorily fitted with a bi-exponential expression. Emission decays with added redox quenchers could only be satisfactorily fit to a tri-exponential form. The values reported in Table 1 are average lifetimes (<τ>), calculated by using eq 3-3, where A_i is the amplitude and τ_i is the lifetime of a given component. Average lifetimes are used as a mathematical model to represent the system as a whole and the amplitudes and lifetimes of the individual components are not interpreted to have a physical meaning.

$$< \tau > = \sum A_i \tau_i^2 \, / \sum A_i \tau_i \qquad \textbf{(eq 3-3)}$$

$$f(t) = A_1 e^{-(t/\tau_1)} + A_2 e^{-(t/\tau_2)} + A_3 e^{-(t/\tau_3)} \qquad \textbf{(eq 3-4)}$$

Table 3-1. Absorptance, emission, and lifetime data on Ru and Os MOFs suspended in degassed MeCN at 23°C ± 2°C.

	Abs. λmax (nm)	Em. λmax (nm)	average lifetime (ns)
1	470	635	610
2	435	630	1100
1-Os	445	765	15
2-Os	450	770	30

In order to demonstrate light harvesting, redox quenching was carried out with MOF microcrystals. Interfacial electron transfer quenching experiments were conducted by both emission intensity and lifetime measurements on stirred suspensions of the MOFs in degassed acetonitrile at 23°C±2°C with added oxidative quencher 1,4-benzoquinone (BQ; $E^{o\prime}(BQ/BQ^{-})$ = -0.52 V vs SCE in acetonitrile with 0.1 M TBAH) or reductive quencher N,N,N',N'-tetramethylbenzidine (TMBD; $E^{o\prime}(TMBD^{+})$ = 0.43 V vs SCE in acetonitrile with 0.1 M TBAH). In these experiments, stock suspensions of the MOFs were pipetted into cuvettes with the quencher subsequently added. The concentrations of MOF were ~40 μM

(based on Ru) as determined by digesting the sample with tetrabutylammonium hydroxide after data collection and measuring the absorbance of the released building blocks.

These data show that the extent of Ru(II)* emission quenching increases as the quencher concentration is increased. With added BQ, greater than 90% quenching of Ru(II)* in **1** is observed at ~0.3 M while >98% quenching in **2** is obtained at ~0.1 M BQ. As in solution quenching of related excited states,[7] quenching is by oxidative electron transfer, $Ru(II)^* + BQ \rightarrow [Ru(III)]^+ + BQ^{\cdot -}$. A major contribution from energy transfer is unlikely since the triplet energy of BQ is 18,600 cm^{-1}, ~400 cm^{-1} higher than the lowest MLCT excited state energy in **2**.[8] Based on estimated Ru(II)* MOF excited state energies, the driving force for electron transfer is favored by 0.46 eV for **1** and by 0.35 eV by **2**. Preliminary time-resolved electron paramagnetic resonance experiments provided direct evidence for the formation of semi-hydroquinone free radicals (HBQ·). Irradiation of an ethylene glycol suspension of **2** in the presence of BQ at 500 nm gave $BQ^{\cdot -}$ which subsequently abstracts a proton from ethylene glycol to yield HBQ·.

Similarly, with added reductive quencher TMBD, 98% of the Ru(II)* emission in **2** was quenched at its solubility limit in MeCN (~20 mM). Quenching of **1** also occurs but much less efficiently. Quenching by TMBD must also have occurred by electron transfer given the absence of a low-lying acceptor excited state for TMBD. Reductive electron transfer quenching by TMBD, $Ru(II)^* + TMBD \rightarrow Ru(II)]^- + TMBD^{+\cdot}$, is favored by 0.74 eV for **1** and by 0.91 eV for **2**.

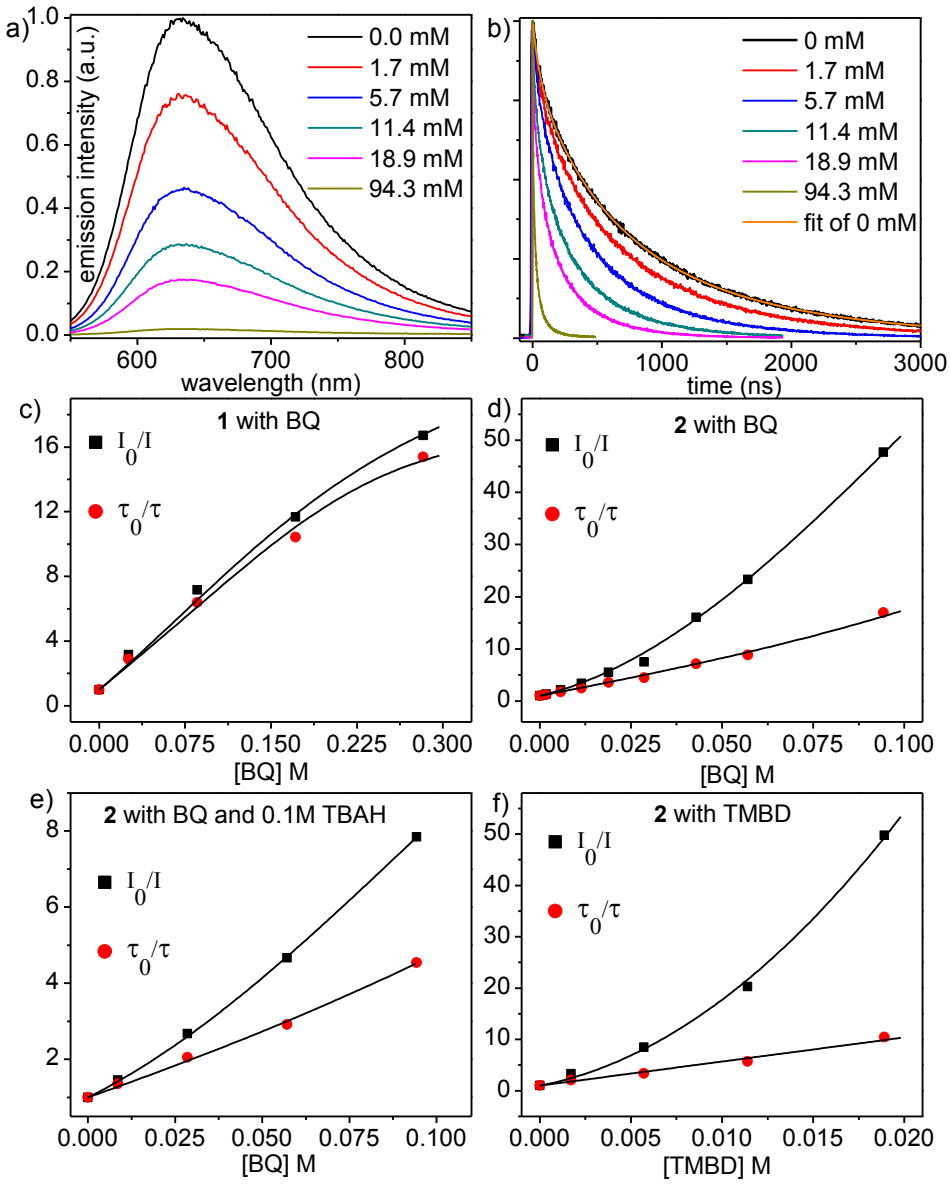

Figure 3-6. (a) Steady-state and (b) time-resolved emission data for **2** with added BQ in degassed MeCN at 23°C ± 2°C. For a Stern-Volmer analysis of steady-state emission, emission intensity was integrated from 550-850. Lifetime data were obtained following 485 nm excitation with monitoring at the emission max at 620 nm. (c-f) Steady-state and time-resolved Stern-Volmer quenching analysis of **1** or **2** with BQ or TMBD. Quenching by BQ of (a) **1** (b) **2** (c) **2** with 0.1 M TBAH and (d) quenching of **2** by TMBD.

The driving force for electron transfer reaction can have large influences on the rate and therefore it must be considered. The excited-state redox potentials of **1** and **2** can be estimated from the Ru III/II potential obtained from square-wave voltammetry and the

emission energy. The E_0 value was taken to be the energy at 10% of the emission maxima at the blue edge and was added to the Ru III/II potential to estimate the reduction potential of the excited-states of **1** and **2**.

Table 3-2. Excited-state redox potentials of **1** and **2**.

	Ru III/II Ox (V vs SCE)	Ru II* red (V vs SCE)
1	1.17	-0.98
2	1.34	-0.87

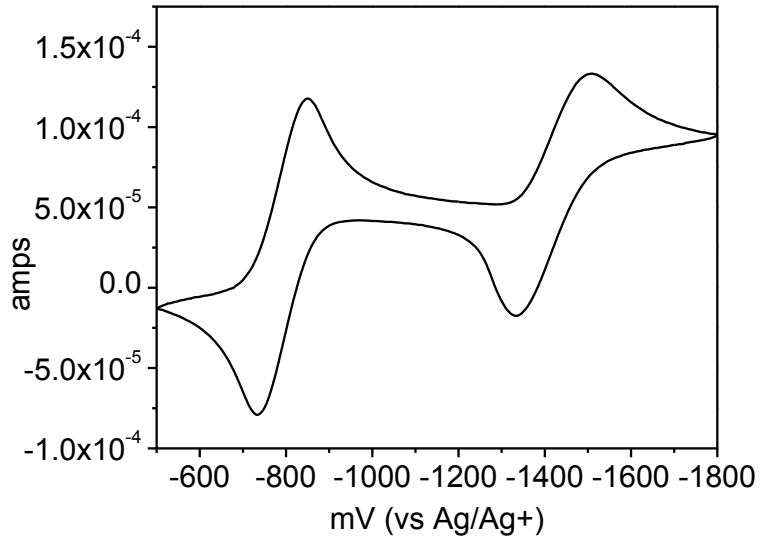

Figure 3-7. Cyclic voltammetry of BQ in acetonitrile with 0.1 M TBAH at 50 mV/s.

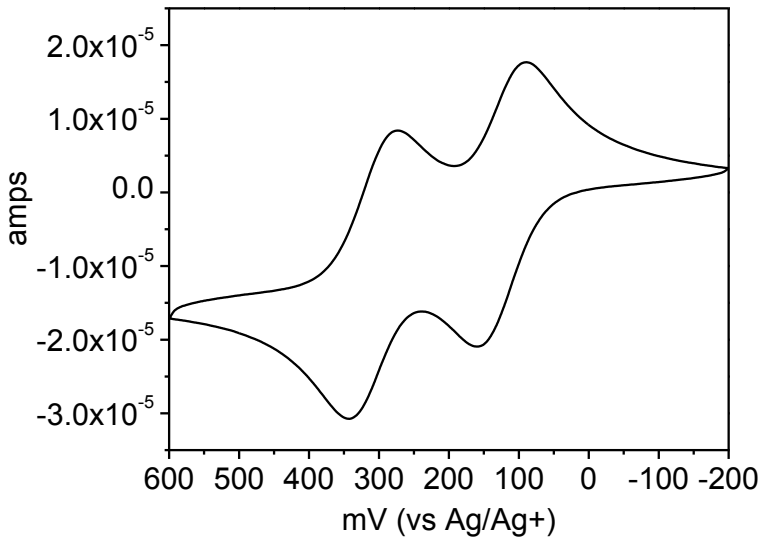

Figure 3-8. Cyclic voltammetry of TMBD in acetonitrile with 0.1 M TBAH at 50 mV/s.

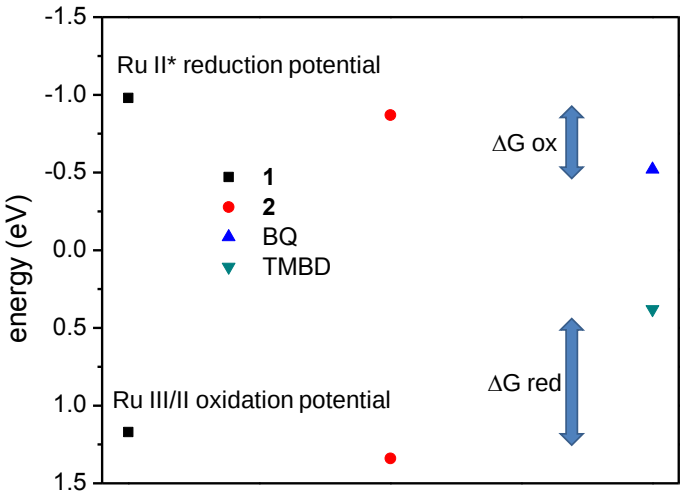

Figure 3-9. Thermodynamics of electron transfer quenching reactions reported vs SCE in MeCN. The Ru (III/II) potentials were determined from squarewave-voltametry and RuII* reduction potentials were estimated by adding E_0 to Ru(III/II) . E_0 was estimated to be the energy at 10% of the blue edge of the emission maximum.

Although there is 0.79 eV of driving force for the reaction between **1*** and TMBD the efficiency is quite low, while **2** is quenched rapidly. With added BQ the quenching efficiency of **2** was still greater than **1** but the difference was not as drastic.

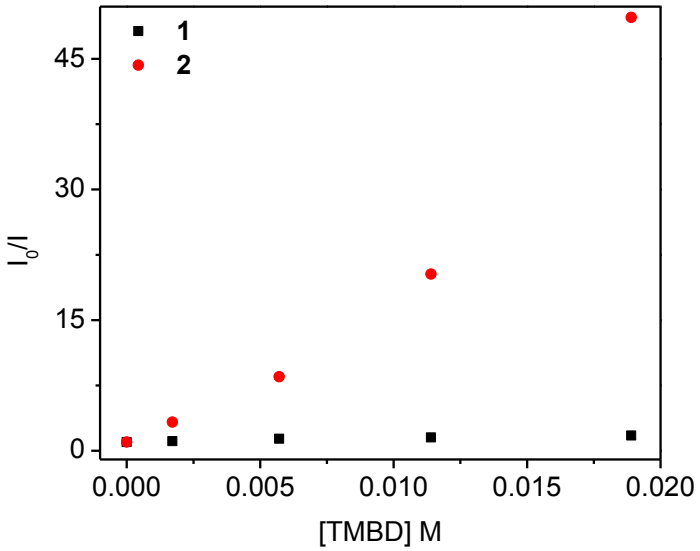

Figure 3-10. Steady-state emission quenching of the Ru MOFs by TMBD at 500 nm excitation. Intensity values were obtained by the integrated emission from 550 to 850 nm.

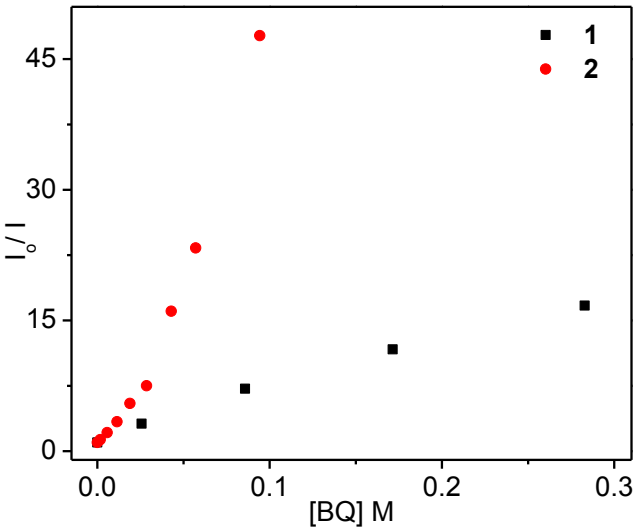

Figure 3-11. Steady-state emission quenching of the Ru MOFs by BQ at 500 nm excitation. Intensity values were obtained by the integrated emission from 550 to 850 nm.

3.2.1 Quencher/MOF Association

At the heart of the microscopic model used to describe the steady-state and time-resolved Stern-Volmer data is the equilibrium between the quencher (Q) in solution and quencher bound to the crystal surface. The fraction of occupied surface sites is described by the Langmuir isotherm:

$$F_{SQ} = \frac{K_A[Q]}{1+ K_A[Q]} \qquad \textbf{(eq 3-5)}$$

where F_{SQ} is the fraction of sites with surface-bound quencher, [Q] is the quencher concentration and K_A is the association constant.

For quenching of **1** by BQ, the Stern-Volmer plots reveal nearly parallel variations of I_o/I and τ_o/τ with increasing quencher concentration. This behavior is qualitatively consistent with minimal pre-association and/or relatively slow electron transfer with a minor role for static quenching. A significant difference in behavior was observed for **2**. For both oxidative quenching by [BQ] and reductive quenching by [TMBD], plots of I_o/I vs. [quencher] are dramatically upward curving while the τ_o/τ data deviate only slightly from linearity. These observations are consistent with pre-association and quenching by both static and dynamic

quenching mechanisms. The reversible pre-association of quenchers at the MOF/solution interface of **2** was confirmed by ^{1}H NMR studies on quencher-soaked MOF microcrystals and by the release of TMBD from the MOF microcrystals in fresh solutions as probed by luminescence measurements.

A sample of **2** was soaked in 20 mM TMBD in MeCN overnight. The crystals were then filtered and washed with MeCN and the TGA shows an additional 5% organic weight loss which corresponds with associated TMBD.

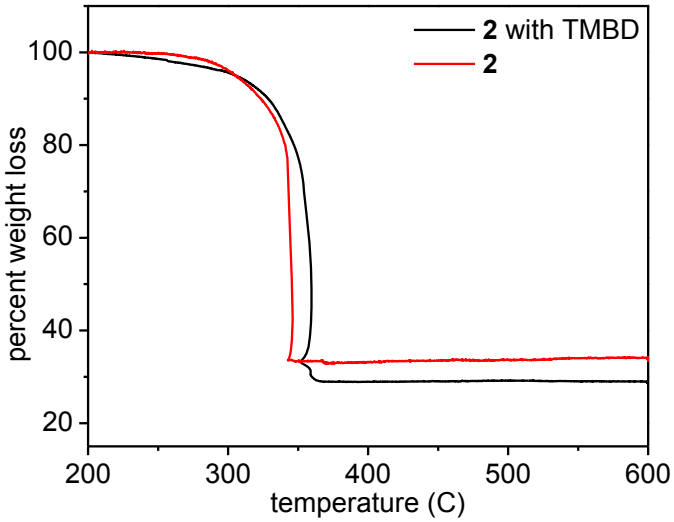

Figure 3-12. Thermogravimetric analysis of **2** after soaking overnight in a 20 mM TMBD solution in MeCN or pure MeCN.

The dynamics of this association can be examined by monitoring the steady-state emission at a single wavelength. MOF-**2** crystals were mixed with a quencher solution (0.05 M BQ or 0.01 M TMBD in MeCN) and then immediately monitored. It can be observed that the emission declines as the quenchers diffuse into the first few layers of the MOF with BQ reaching equilibrium more quickly than TMBD. This effect was not observed for **1**, which is consistent with the negligible association constant predicted. The crystals were soaked in the quencher solutions for approximately 1 hour and were then isolated by centrifugation. The reversibility of the interaction between **2** and the quenchers was tested by suspending the

isolated crystals in pure MeCN and monitoring the emission intensity as a new equilibrium is reached. As the quenchers dissociates, the emission intensity increases and as before the equilibrium is reached more quickly for BQ, about 5 minutes, than with TMBD which is still increasing after 40 minutes.

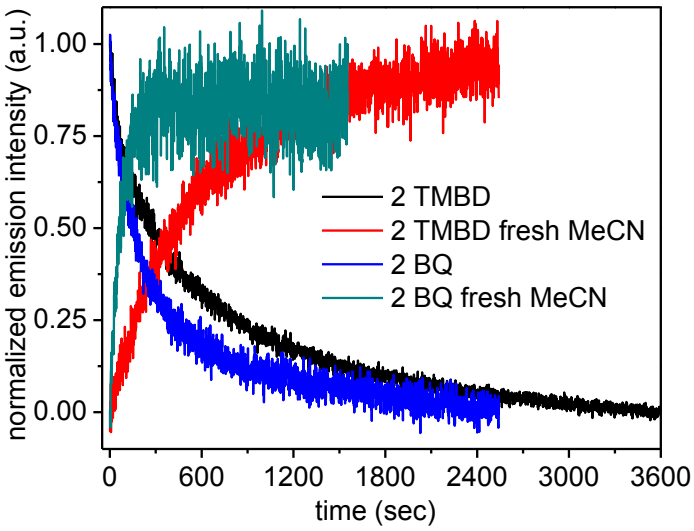

Figure 3-13. Normalized steady-state emission intensity of **2** at 650 nm with added TMBD or BQ to fresh crystals and quencher associated crystals in fresh MeCN.

NMR was used to quantify the ratio of Ru monomer to associated quencher by soaking the crystals overnight in 0.3 M BQ or 0.02 M TMBD in MeCN, quickly washing with acetone, and then digesting the sample in deuterated DMSO with DCl. MOF-**1** had only trace amounts of BQ which is consistent with the redox emission quenching occurring by a diffusional mechanism at the MOF/solution interface. With **2**, there is some extent of penetration of the quenchers into the pores and the trend is the same with the predicted association constant. One BQ molecule is incorporated for every 40 Ru complexes and the ratio increases for TMBD with one molecule for every 10 Ru complexes. PXRD was collected on the crystals after soaking in the quencher solutions overnight and no significant changes were observed.

Table 3-3. Ratio of Ru to quencher after soaking overnight in a 0.3 M BQ or 0.02M TMBD solution as determined by ^{1}H NMR.

Sample	Ru to quencher ratio
1 with BQ	>100 to 1
2 with BQ	40 to 1
2 with TMBD	10 to 1

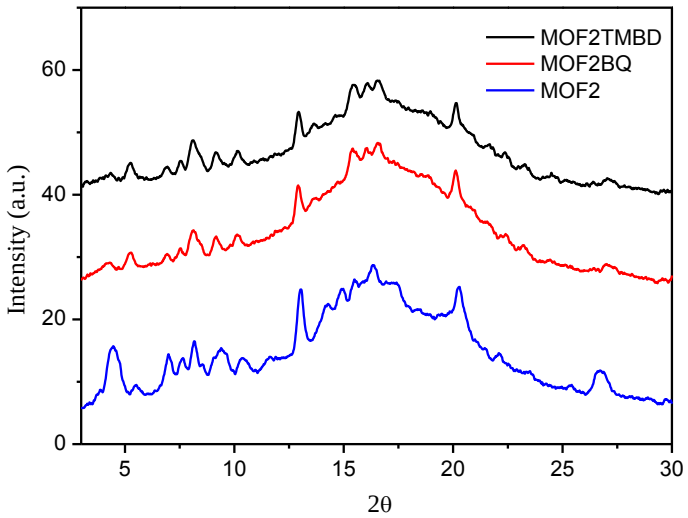

Figure 3-14. PXRD pattern of **2** after soaking in 0.02M TMBD, 0.3 M BQ, or pure MeCN overnight.

3.3 Modified Stern Volmer Quenching Analysis

Luminescence quenching behaviors were modeled using the series of reactions depicted in the figure below, with quenching by BQ as the example. In the scheme it is assumed that quenching occurs at the MOF-solution interface after migration from the core of the crystal and that there are two quenching pathways. One pathway is diffusional, k_D, while in the other is static, k_S, which involves pre-association at the surface followed by interfacial quenching.

Figure 3-15. MOF emission quenching with BQ.

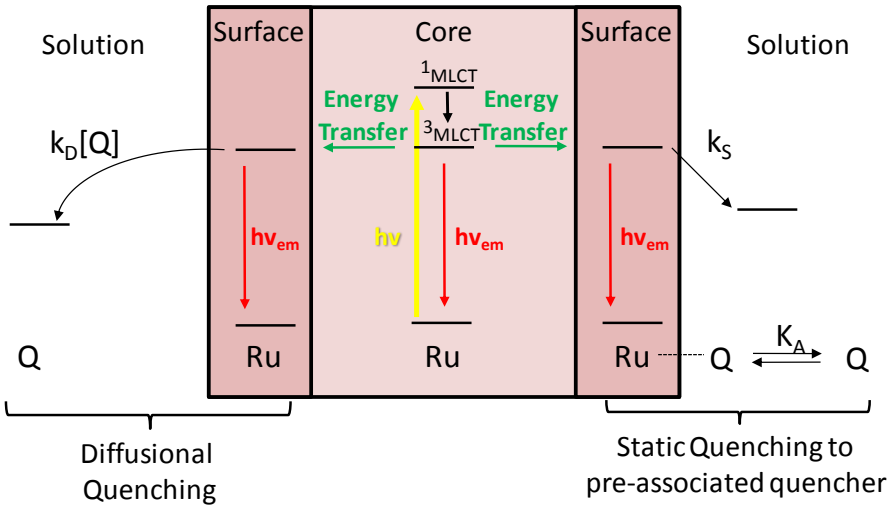

$$Ru^{II}_{core} \xrightarrow{h\nu} Ru^{II*}_{core}$$

$$Ru^{II*}_{core} \leftrightarrow Ru^{II*}_{surface} : F = k_{mig}/(k_{mig} + \tau_0^{-1})$$

$$Ru^{II*}_{surface} + BQ \leftrightarrow Ru^{II*}_{surface}, BQ : K_A$$

$$Ru^{II*}_{surface}, BQ \rightarrow Ru^{III}_{surface} + BQ^{-\cdot} : k_S$$

$$Ru^{II*}_{surface} + BQ \rightarrow Ru^{III}_{surface} + BQ^{-\cdot} : k_D$$

The constants in Figure 3-15 are: (i) F (or γ): The fraction of excited states that reach the MOF-solution interface. k_{mig} is the migration rate constant for energy transfer from core sites to the surface or the product of the number of energy transfer steps and the Ru(II)* to Ru(II) hopping rate. τ_0 is the excited state lifetime without added quencher. (ii) K_A: The association constant between the quencher and MOF surface. (iii) k_S: The rate constant for BQ quenching of Ru(II)* at the surface, $[Ru(II)^*]_{surface}$. (iv) k_D: The rate constant for diffusional quenching of Ru(II)* at the MOF-solution interface.

Photoexcitation produces excited states (Ru*) throughout the crystal, which then have to migrate to the surface in order to be quenched. The result is three classes of Ru excited states: (1) those trapped in the core of the crystal and inaccessible to quencher, (2) those

located at the crystal surface that are quenched by a pre-associated quencher (static quenching) and (3) those located the surface sites without pre-associated quencher and hence are quenched by quenchers in solution (diffusional quenching).

The emission intensity is the sum of these three contributions. The emission intensity emanating from the crystal interior is given by equation 3-7. In this expression (1- γ) represents the fraction of excited states that remain in the core of the crystal and are inaccessible to quencher and I_0 is the emission intensity in the absence of quencher. The static and diffusional quenching contributions are then given by equations 3-8 and 3-9 where $(k_{Ru*})^{-1} = \tau_0$.

$$I = I_{Bulk} + I_{Stat} + I_{Diff} \qquad \textbf{(eq 3-6)}$$

$$I_{Bulk} = (1-\gamma)I_0 \qquad \textbf{(eq 3-7)}$$

$$I_{Stat} = \gamma F_{SQ} \frac{k_{Ru*}}{k_{Ru*}+k_S} I_0 \qquad \textbf{(eq 3-8)}$$

$$I_{Diff} = \gamma(1-F_{SQ}) \frac{k_{Ru*}}{k_{Ru*}+k_D[Q]} I_0 \qquad \textbf{(eq 3-9)}$$

The quantity corresponding to the steady-state Stern-Volmer measurement is then given by equation 3-10.

$$\frac{I_0}{I} = \left((1-\gamma) + \gamma F_{SQ} \frac{k_{Ru*}}{k_{Ru*}+k_S} + \gamma(1-F_{SQ}) \frac{k_{Ru*}}{k_{Ru*}+k_D[Q]} \right)^{-1} \qquad \textbf{(eq 3-10)}$$

The luminescence decay corresponding to these three emitting components will be a sum of three decaying exponentials where the amplitudes are given by the equations below.

$$I(t) = A_{Bulk} exp(-k_{Ru*}t) + A_{Stat} \exp(-(k_{Ru*}+k_S)t) + A_{Diff} \exp(-(k_{Ru*}+k_D Q)t) \qquad \textbf{(eq 3-11)}$$

$$A_{Bulk} = (1-\gamma) \qquad \textbf{(eq 3-12)}$$

$$A_{Stat} = \gamma F_{SQ} \qquad \textbf{(eq 3-13)}$$

$$A_{Stat} = \gamma(1 - F_{SQ}) \quad \textbf{(eq 3-14)}$$

For the decay expressed above, the average lifetime can be written as:

$$\langle\tau\rangle = \frac{A_{Bulk}\left(\frac{1}{k_{Ru*}}\right)^2 + A_{Stat}\left(\frac{1}{k_{Ru*}+k_S}\right)^2 + A_{Diff}\left(\frac{1}{k_{Ru*}+k_D Q}\right)^2}{A_{Bulk}\left(\frac{1}{k_{Ru*}}\right) + A_{Stat}\left(\frac{1}{k_{Ru*}+k_S}\right) + A_{Diff}\left(\frac{1}{k_{Ru*}+k_D Q}\right)} \quad \textbf{(eq 3-15)}$$

Based on this, the time-resolved Stern-Volmer quantity can be expressed as:

$$\frac{\tau_0}{\tau} = \frac{1}{k_{Ru*}\langle\tau\rangle} \quad \textbf{(eq 3-16)}$$

The steady-state and time-resolved Stern-Volmer equations were simultaneously fit to the experimental data using a nonlinear least-squares regression analysis to extract values for the 4 adjustable parameters: K_A, γ, k_S and k_D. The value for k_{Ru*} was obtained through direct measurement of the emission decay in the absence of quencher. The fitting results for the Stern-Volmer analysis for BQ and TMBD quenching of **1** and **2** are summarized in Table 3-10. For oxidative quenching of **1** by BQ the results of the kinetic analysis are consistent with a small pre-association constant (K_A = 1.9 M^{-1}), high fraction of excited states captured at the interface (γ = 0.99), and relatively slow electron transfer quenching with $k_S = 2.5\text{x}10^7$ s^{-1} and $k_D = 9.5\text{x}10^7$ $M^{-1}s^{-1}$. The appearance of dual channels for quenching may have a microscopic origin in multiple quenching sites at the crystal-solution interface or may be due to quenching at different faces of the crystal. For quenching of **2** by BQ, K_A = 35 M^{-1}, $\gamma \sim 1$, $k_S = 2.3\text{x}10^8$ s^{-1}; and $k_D = 1.1\text{x}10^8$ $M^{-1}s^{-1}$. A role for the surface interaction in **2** is supported by less efficient quenching with added electrolyte. With 0.1 M added tetrabutylammonium hexafluorophosphate (TBAH), K_A = 14 M^{-1}, $\gamma \sim 1$, $k_S = 2.6\text{x}10^7$ s^{-1}; and $k_D = 2.9\text{x}10^7$ $M^{-1}s^{-1}$.

Table 3-4. Fitting Results of Stern-Volmer Plots in MeCN at 23 °C ± 2°C.

	K_A (M^{-1})	γ	k_S (ns^{-1})	k_D (10^7 $M^{-1}s^{-1}$)
1 - BQ	1.9±1.8	0.9996 ±0.0002	0.0246 ±0.005	9.5±0.9
2 - BQ	35.1±3.4	1.000	0.230 ±0.052	11.4±0.6
2 - BQ, TBAH	13.7±1.8	0.9992 ±0.0014	0.0265 ±0.006	2.9±0.2
2 - TMBD	259±31	1.000	>15	34.4±4.4

3.4 Concluding Remarks

Microscale MOFs based on photo-active Ru(II)-bpy building blocks have demonstrated "antenna"-like behaviors with high electron transfer efficiencies (>98%) toward both oxidative and reductive quenching. Efficient electron transfer quenching results from rapid energy migration over several hundred nanometers followed by efficient electron-transfer quenching at the MOF/solution interface. This is significant in demonstrating MOFs as a viable approach to light harvesting coupled with energy conversion by excited state quenching and electron transfer. Addition of catalytic components to light-harvesting MOFs may lead to interesting novel hybrid materials for efficient artificial photosynthesis. Additionally, attachment of MOF to planar electrodes could facilitate efficient light absorption without using high surface area materials like nanocrystalline TiO_2.

3.5 Experimental Section

After crystal growth the MOF particles were washed three times with methanol and then three times with acetonitrile. After soaking overnight in acetonitrile the crystals were washed once more to make a stock suspension with a concentration of approximately 1mM based on Ru. The Ru concentration was determined by adding tetrabutyl ammonium hydroxide to dissolve the particles and measuring the absorption spectrum. An aliquot of the MOF stock suspension in acetonitrile was combined with different amounts of quencher into

quartz cuvettes and capped with septa. This procedure gave reproducible MOF concentration between samples and concentrations from a typical experiment are shown below.

Table 3-5. Sample preparation for quenching of **1** by BQ.

Sample	**1** stock in MeCN (mL)	MeCN (mL)	0.3 M BQ in MeCN (mL)	Final [BQ] M
1	0.2	3.3	0	0
2	0.2	3.0	0.3	0.0257
3	0.2	2.3	1.0	0.0857
4	0.2	1.3	2.0	0.1714
5	0.2	0	3.3	0.2829

The samples were argon bubble degassed for 30 minutes prior to taking measurements to remove any oxygen. Solvent evaporation, which would result in concentration changes, was prevented by pre-saturating the argon with MeCN by passing argon through a fritted gas washing bubbler before the gas manifold. Magnetic stirring was used to keep the particles suspended so that the emission signal did not decrease from settling of the crystals. Steady-state emission was collected at 500 nm excitation and time-resolved experiments were excited at either 445 or 485 nm on an Edinburgh FLSP920 TCSPC spectrometer. For Ru only samples the emission was collected from 550-850 nm and Os-doped samples were collected between 550-950 nm. Long pass filters were used to eliminate light scattering artifacts.

The time-resolved emission data collected with added quenchers was fit to a tri-exponential and the parameters are shown below. In some cases, the amplitude of the short component is very small but was included such that the fits would be comparable.

Table 3-6. Triexponential fit parameters and average lifetime for **1** with added BQ.

[BQ] M	A_1	τ_1	A_2	τ_2	A_3	τ_3	$\langle\tau\rangle$ Lifetime (ns)
0	1.7	27.1	22	210.1	76.2	607.5	570.9
0.02571	4.3	13.6	44.7	88.7	51	235.1	198.0
0.08571	6.7	1.3	32.3	31.5	61	99.4	89.5
0.17143	32.5	0.8	22.7	19.1	44.8	60.9	54.7
0.28286	48.6	0.7	9.9	10.9	41.5	39.6	37.1

Table 3-7. Triexponential fit parameters and average lifetime for **2** with added BQ.

[BQ] M	A_1	τ_1	A_2	τ_2	A_3	τ_3	<τ> Lifetime (ns)
0	0.8	36.6	15.4	360.6	83.9	1105.4	1063.0
0.00171	0.8	30.6	15.3	283.3	84	902.1	868.4
0.00571	1.6	35.7	19.6	232.7	78.8	649	614.3
0.0114	1.7	19.1	18.5	137.6	79.9	451.4	430.4
0.0189	1.5	10.2	19.6	87.6	78.9	313.3	298.5
0.0286	3.1	15.9	23.8	83.3	73.1	253.3	236.3
0.0429	4.2	12.1	24.6	49.8	71.2	159.7	148.5
0.0571	4.8	10.2	31	43.2	64.2	133.4	120.7
0.0943	3.6	2.3	32.1	18.8	64.4	68.9	62.8

Table 3-8. Triexponential fit parameters and average lifetime for **2** with added BQ and 0.1M TBAH.

[BQ] M	A_1	τ_1	A_2	τ_2	A_3	τ_3	<τ> Lifetime (ns)
0	1	35.8	18.7	336.3	80.4	1012.2	963.3
0.00857	2	42.1	21.8	270.6	76.3	757.6	711.6
0.02857	2.5	30.1	22.5	165.5	75	501.2	470.1
0.05714	4.4	27.1	25.3	119.4	70.3	357.4	330.6
0.09429	2.4	4.4	22.7	55	75	223.9	212.1

Table 3-9. Triexponential fit parameters and average lifetime for **2** with added TMBD.

[BQ] M	A_1	τ_1	A_2	τ_2	A_3	τ_3	<τ> Lifetime (ns)
0	1	54	16	408.5	83	1194	1144.8
0.00171	2.5	38	20.5	192.2	77	583	550.5
0.00571	4.4	20.3	30.5	120	62.1	376.7	340.9
0.0114	4.9	9	29.7	60.1	65.4	219.1	201.0
0.0189	5.5	2.5	27.7	25.6	66.8	117.6	109.8

N,N,N',N' tetramethylbenzidine (TMBD) was purified by a silicia column eluting with chloroform and 1,4 benzoquinone (BQ) was purified by sublimation. Electrochemical measurements were performed on an BAS potentiostat/galvanostat. Voltammetric measurements were made with a planar EG&G PARC G0229 glassy carbon millielectrode, a platinum wire EG&G PARC K0266 counter electrode, and 0.01M $AgNO_3$ TBAH reference electrode.

3.6 References

1. Rieter, W. J.; Pott, K. M.; Taylor, K. M.; Lin, W., Nanoscale coordination polymers for platinum-based anticancer drug delivery. *J Am Chem Soc* 2008, 130, 11584-5.

2. Lin, W.; Rieter, W. J.; Taylor, K. M., Modular synthesis of functional nanoscale coordination polymers. *Angew Chem Int Ed Engl* 2009, 48, 650-8.

3. Spokoyny, A. M.; Kim, D.; Sumrein, A.; Mirkin, C. A., Infinite coordination polymer nano- and microparticle structures. *Chem Soc Rev* 2009, 38, 1218-27.

4. Horcajada, P.; Chalati, T.; Serre, C.; Gillet, B.; Sebrie, C.; Baati, T.; Eubank, J. F.; Heurtaux, D.; Clayette, P.; Kreuz, C.; Chang, J. S.; Hwang, Y. K.; Marsaud, V.; Bories, P. N.; Cynober, L.; Gil, S.; Ferey, G.; Couvreur, P.; Gref, R., Porous metal-organic-framework nanoscale carriers as a potential platform for drug delivery and imaging. *Nat Mater* 9, 172-8.

5. deKrafft, K. E.; Xie, Z.; Cao, G.; Tran, S.; Ma, L.; Zhou, O. Z.; Lin, W., Iodinated nanoscale coordination polymers as potential contrast agents for computed tomography. *Angew Chem Int Ed Engl* 2009, 48, 9901-4.

6. Shaw, G. B.; Brown, C. L.; Papanikolas, J. M., Investigation of interligand electron transfer in polypyridyl complexes of Os(II) using femtosecond polarization anisotropy methods: Examination of Os(bpy)(3)(2+) and Os(bpy)(2)(mab)(2+). *Journal of Physical Chemistry A* 2002, 106, 1483-1495.

7. Darwent, J. R.; Kalyanasundaram, K., ELECTRON-TRANSFER REACTIONS OF QUINONES, HYDROQUINONES AND METHYL VIOLOGEN, PHOTOSENSITIZED BY "TRIS(2,2'-BIPYRIDINE)-RUTHENIUM(II). *Journal of the Chemical Society-Faraday Transactions Ii* 1981, 77, 373-382.

8. Veenvliet, H.; Wiersma, D. A., STRUCTURE AND DYNAMICS OF LOWEST TRIPLET-STATE IN PARA-BENZOQUINONE .1. ISOTOPE-EFFECT STUDY ON OPTICAL-ABSORPTION, EMISSION AND ODMR SPECTRA. *Chemical Physics* 1975, 8, 432-457.

9. Kent, C. A.; Mehl, B. P.; Ma, L. Q.; Papanikolas, J. M.; Meyer, T. J.; Lin, W. B., Energy Transfer Dynamics in Metal-Organic Frameworks. *Journal of the American Chemical Society* 2010, 132, 12767-12769.

CHAPTER 4

AMPLIFIED QUENCHING IN METAL-ORGANIC FRAMEWORKS

4. 1 Introduction to Amplified Quenching

Amplified luminescence quenching, a signal gain as a result of interactions between a sensing material and analytes accompanied by rapid energy migration, has been demonstrated in fluorescent conjugated polymers functionalized with receptor sites.[1] Dramatic emission quenching enhancements have been observed compared to monomeric models due to a "molecular wire" effect with the conjugated polymer facilitating energy migration over long distances. As the excited-state migrates, it samples multiple receptor sites, thus requiring fewer receptor sites to be occupied by a quencher to elicit a significant spectroscopic response. Amplified fluorescence quenching of conjugated polymers is the basis of many practical sensing materials with extraordinarily high detection sensitivities.[2-4] To date, many types of conjugated polymers with singlet excited-states have been shown to exhibit amplified quenching.[5-14] Phosphorescent materials capable of amplified quenching are potentially advantageous because the large red-shifts between light absorption and emission, as a result of intersystem crossing, can eliminate interference from the exciting light source in device configurations. Long-lived triplet excited-states of phosphorescent materials can also allow excited state migration over longer distances, potentially leading to even higher levels of amplified quenching.

Attempts at developing amplified quenching with phosphorescent platinum(II)-acetylide polymers have been hindered by slow triplet diffusion despite long lifetimes of 20

μs.[15] Quenching enhancements of 75-fold have been demonstrated in conjugated polymers with covalently linked Ru-bpy complexes[16] although excited-state migration is likely by site-to-site hopping rather than via the polymer backbone.[17]

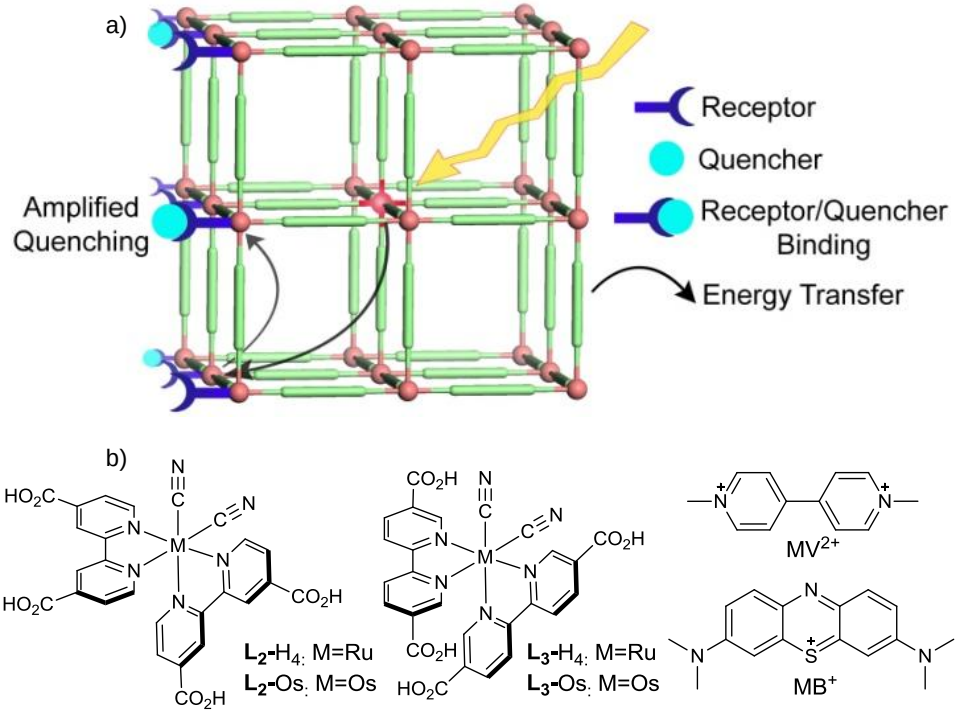

Figure 4-1. a) Schematic diagram illustrating amplified quenching in MOFs and b) chemical structures of the photo-active MOF building blocks and cationic quenchers (MV^{2+} and MB^{+}) used in this work. $\mathbf{L_2}$ and $\mathbf{L_3}$ refer to the building blocks for MOF **2** and **3** respectively.

Metal-organic frameworks (MOFs) represent a new class of structurally ordered hybrid materials whose properties can be fine-tuned at the molecular level to suit many applications.[18-33] In particular, our work described in chapters 2 and 3 demonstrated rapid energy migration over long distances[34] and efficient electron transfer quenching at the interfaces of emitting MOFs, respectively.[35] We surmised that MOFs composed of Ru(II)-bpy building blocks offer a promising scaffold for amplified quenching based on their lowest, largely triplet metal-to-ligand charge transfer (MLCT) excited-states. We report here a remarkable example of MOF-based amplified quenching in Ru(II)-bpy-based MOFs by cationic quenchers with enhancements of up to 7000-fold compared to a model complex.

4. 2 Amplified Quenching Stern-Volmer Analysis

Excited state quenching was investigated by both emission intensity and lifetime measurements on stirred suspensions containing the MOF microcrystals in degassed acetonitrile with added methyl viologen (MV^{2+}) or methylene blue (MB^{+}) as the quenchers. The MOF concentrations were 15 μM (based on Ru) as determined by the absorbance of the released building blocks after dissolution in 1M HCl. Emission transients were satisfactorily fit to biexponential or triexponential decay functions for **3** and **2**, respectively, and are reported as average lifetimes. Quenching results were analyzed by the Stern-Völmer expression in equation 4-1, in which I_o is the integrated emission intensity without quencher and I is the intensity at a given quencher concentration. In a diffusional system, the Stern-Völmer (SV) constant, K_{SV}, is given by equation 4-2 with k_q being the quenching rate constant and τ_o being the excited state lifetime without added quencher. When static quenching is the dominant mechanism, K_{SV} is given by equation 4-3 with K_A being the surface interaction constant and N_S being the number of surface sites sampled by the excited state.

$$I_0/I = 1 + K_{SV}[Q] \qquad \textbf{(Eq 4-1)}$$

$$K_{SV(\text{diffusional})} = k_q * \tau_0 \qquad \textbf{(Eq 4-2)}$$

$$K_{SV(static)} = K_A * N_S \qquad \textbf{(Eq 4-3)}$$

$$K_A = \frac{[SURF{-}Q]}{[SURF][Q]} \qquad \textbf{(Eq 4-4)}$$

The quenching rate constant is k_q and is limited by diffusion to a maximum value of around 2 x 10^{10} in MeCN depending upon the size of the molecule. In a solution system governed by static quenching the slope of the emission intensity SV plot is the association constant, K_A. The lifetime is unchanged with static quenching since emission is observed only from

molecules without associated quenchers. The relationship when both static quenching and dynamic quenching occur is shown below.

$$\frac{I_0}{I} = (1 + K_{SV}[Q])(1 + K_A[Q]) = 1 + (K_{SV} + K_A)[Q] + K_{SV}K_A[Q]^2 \qquad \textbf{(Eq 4-5)}$$

A quadratic relationship occurs when both static and dynamic quenching are present. However, the upward curvature observed in amplified quenching here occurs at such a low quencher concentration that diffusional quenching cannot account for even 1% of the total quenching.

When measuring the time-resolved emission of complexes in solution, the SV analysis measures only dynamic (diffusional) quenching if static quenching within a pre-associated chromophore-quencher pair is rapid. However, the time-resolved SV analysis of **2** does exhibit a MV^{2+} dependence even in the absence of diffusional quenching. In the MOF microcrystals, static quenching is not entirely instantaneous because excited-state migration occurs from the core to a pre-associated quencher at the surface after a finite time, resulting in a dynamic decrease in the experimentally observed lifetime.

4. 3 Amplified Quenching of 2 and 3

4.3.1 Amplified Quenching of 3 with MV^{2+}

Single crystals of $[Zn_5(\mathbf{L3})_2\bullet(\mu\text{-}OH)\bullet(HCO_2)\bullet DMF\bullet 2H_2O]\bullet 6H_2O$ (**3**) were prepared by heating a mixture of $\mathbf{L3_{Ru}}\text{-}H_4$ and $Zn(NO_3)_2$ in a solvent mixture of DMF and H_2O for two weeks. Plate-like microcrystals of **3** of approximately 200 nm in thickness and several microns in diameter were prepared by heating the above mixture and formic acid for 5 days.

Single-crystal X-ray structure determination of **3** revealed a three-dimensional (3D) framework that crystallizes in the monoclinic space group P2/n and gives a formula of $[Zn_5(\mathbf{L3})_2\bullet(\mu\text{-}OH)\bullet(HCO_2)\bullet DMF\bullet 2H_2O]\bullet 6H_2O$. There are two crystallographically distinct

four-metal centered cores in which Ru and Zn are bridged by cyano groups (simplified as rectangle with different colors in Figure 4-2b).

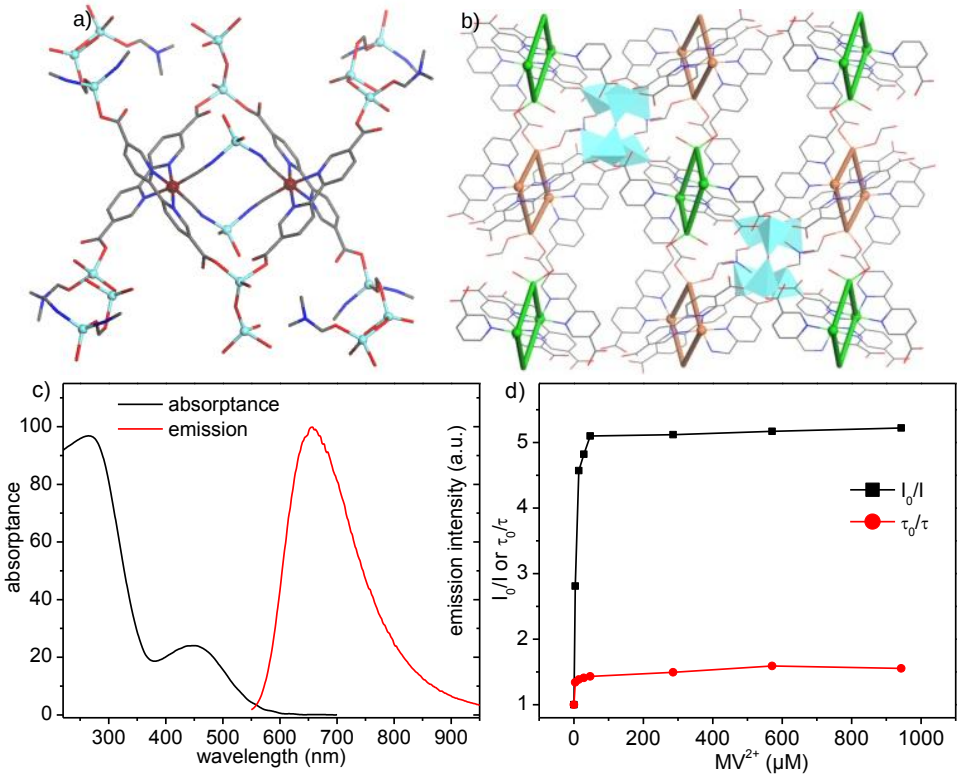

Figure 4-2. a) Stick/Ball model showing the four-Zn cores with cyano groups bridging between tetrahedral zinc and ruthenium centers in **3**. b) Stick/polyhedral model showing the connection of the four-Zn cores to form the 3-D framework structure of **3**. c) absorptance and emission spectra of **3**, and d) steady-state and time-resolved SV plot of **3** with methyl viologen dication (MV^{2+}) in acetonitrile with 485 nm excitation (15 μM based on Ru). Intensity values were obtained from the integrated emission from 650 to 950 nm; emission decays were monitored at 670 nm. Absorptance values were calculated from transmission and diffuse reflectance measurements.

3 emits at λ_{max} = 655 nm with a lifetime of 150 ns. Emission quenching of **3*** by MV^{2+} is efficient at low quencher concentrations. From the linear region of plots of I_o/I vs $[MV^{2+}]$, $K_{SV} = 4.2 \times 10^5\ M^{-1}$ for **3** with half quenching reached at $[MV^{2+}] = 2.4$ μM. Given the Stern-Völmer relationship in eq 2 the apparent quenching rate constant, $k_{q,app} = 2.8 \times 10^{12}\ M^{-1}s^{-1}$. This value is more than two orders of magnitude higher than the diffusion controlled

limit under these conditions, ruling out diffusional quenching. The MOF surface is partially terminated with carboxylate groups, promoting static quenching by binding MV^{2+} via ionic interactions on the surface, see below.

Emission quenching saturates at $[MV^{2+}]$ = ~50 μM, with 20% of the original emission intensity unquenched at I_0/I = ~5. A microscopic model consistent with the experimental observations is shown in Scheme 4-3. In this model, initial surface binding of the cation occurs by an ionic interaction with the surface carboxylates (K_A). The steady-state SV plot increases linearly with added MV^{2+} up to 5 μM. Quenching occurs by intra-MOF energy transfer via site-to-site hopping to the interface (k_{EN}), where electron transfer quenching of a surface excited state occurs (k_{ET}).[37] Electron transfer quenching is in competition with excited state decay ($1/\tau_o$). For **3**, quenching is incomplete even at high quencher concentration because of competitive excited state decay. Approximately 20% of the excited states remain unquenched even though quenching is expected to be complete at the surface.

Figure 4-3. Mechanism of surface MOF quenching by MV^{2+} (Ru_c and Ru_s are core and surface sites)

$$(Ru_c^{II})(Ru_s^{II}\text{-bpy-}COO^-) + MV^{2+} \rightarrow (Ru_c^{II})(Ru_s^{II}\text{-bpy-}COO^-,MV^{2+}) \qquad (K_A)$$

$$(Ru_c^{II})(Ru_s^{II}\text{-bpy-}COO^-,MV^{2+}) + h\nu \rightarrow (Ru_c^{II*})(Ru_s^{II}\text{-bpy-}COO^-,MV^{2+})$$

$$(Ru_c^{II*})(Ru_s^{II}\text{-bpy-}COO^-,MV^{2+}) \rightarrow (Ru_c^{II})(Ru_s^{II*}\text{-bpy-}COO^-,MV^{2+}) \qquad (k_{EN})$$

$$(Ru_c^{II})(Ru_s^{II*}\text{-bpy-}COO^-,MV^{2+}) \rightarrow (Ru_c^{II})(Ru_s^{III}\text{-bpy-}COO^-,MV^{+}) \qquad (k_{ET})$$

$$(Ru_c^{II*})(Ru_s^{II}\text{-bpy-}COO^-,MV^{2+}) \rightarrow (Ru_c^{II})(Ru_s^{II}\text{-bpy-}COO^-,MV^{2+}) + h\nu \qquad (1/\tau_o)$$

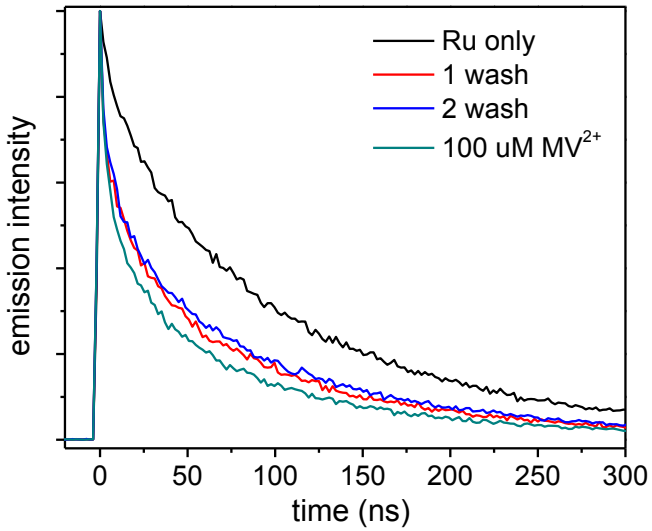

Figure 4-4. Time-resolved 630 emission of **3** with 100 μM MV^{2+} in MeCN upon 485 nm excitation.

The time-resolved emission spectra of **3** with 100 μM MV^{2+} in MeCN shows slower decay kinetics after washing with MeCN. The lifetime increases with successive washes, which suggests that unlike in **2** the MOF-quencher interaction is reversible.

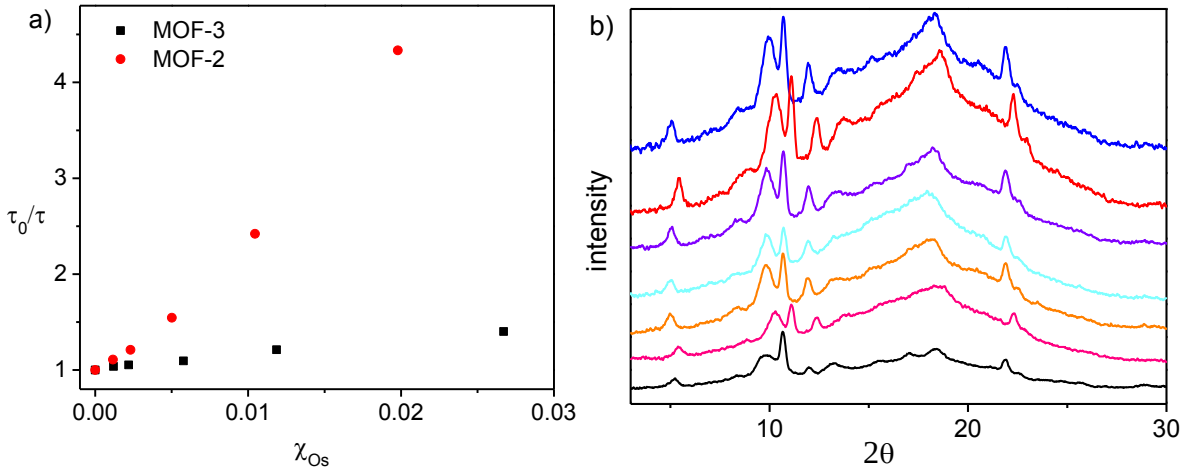

Figure 4-5. a) Stern-Volmer lifetime analysis of Os-doped **3** and **2** as a function of Os mole fraction. Emission lifetime was measured at 620 nm which corresponds with Ru emission. b) PXRD of Os-doped MOF-**3** with the following percent Os concentrations: (top to bottom) 0.00, 0.0012, 0.0022, 0.0058, 0.0119, 0.0267, and 100.00%.

The relative rate of energy transfer for **3** and **2** can be determined by a Stern-Volmer analysis of the Ru lifetime as a function of Os mole fraction. The Ru lifetime decreases as the

Os content increases because of Ru to Os energy transfer quenching. The steeper slope in **2** than in **1** demonstrates that energy transfer occurs at higher rate in **2** which may result in even more dramatic amplified quenching.[35] The PXRD demonstrates that the doping of Os does not change the phase of the MOF.

4.3.2 Amplified Quenching of 2 with MV^{2+}

2 emits with λ_{max} = 630 nm and τ = 900 ns and is also partially terminated with carboxylate groups which can participate in surface ionic interactions. At low MV^{2+} concentrations, in the linear response region, $K_{SV} = 3.2 \times 10^6\ M^{-1}$ at a concentration of 15 μM **2** (based on total Ru). This results in a $k_{q,app} = 3.6 \times 10^{12}\ M^{-1}s^{-1}$ which, again, is well beyond the diffusion controlled limit and consistent with static quenching as illustrated in Scheme 1. Based on lifetime measurements on Os^{II}-doped MOFs , intra-MOF energy transfer in **2** is more rapid than in **1** and quenching of **2*** proceeds essentially to completion as the concentration of MV^{2+} is increased. Quenching was 97% complete at $[MV^{2+}]$ = 2.8 μM with only 0.31 μM of MV^{2+} required for half quenching. This is several orders of magnitude less than required for half quenching of **2*** by the neutral quenchers 1,4-benzoquinone (7400 μM) and N,N,N',N'-tetramethylbenzidine (760 μM).[35]

The magnitude of K_{SV} in the linear region is also dependent on the MOF concentration with K_{SV} increasing as the MOF concentration decreases. This is a predicted result of the model in Scheme 1. It arises from a competition for MV^{2+} by a limited number of surface sites. At lower MOF concentrations, there is a higher concentration of quenchers available per MOF particle.

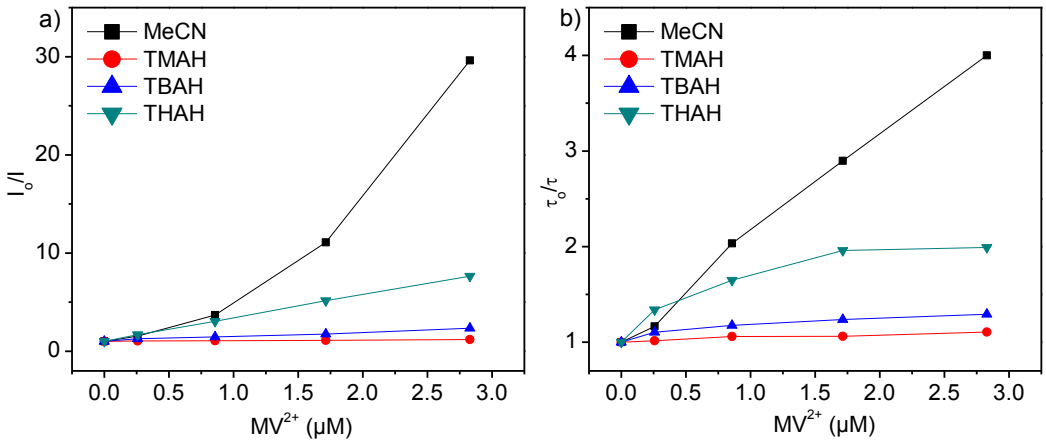

Figure 4-6. a) Steady-state (I/I_o) and b) time-resolved (τ/τ_o) SV plots of **2** (15 μM based on Ru) with methyl viologen (MV^{2+}) in acetonitrile with 0.1 M *tetra*-N-alkylammonium hexafluorophosphate electrolytes (TMAH, TBAH, and THAH are the methyl, *n*-butyl, and *n*-hexyl derivatives) at 485 nm excitation. Emission intensities were evaluated from the integrated emission spectra from 550 to 850 nm. Emission decay was monitored at 630 nm.

The steady-state emission SV plot in Figure 4-6a displays upward curvature or "superlinear" behavior. We reported similar behavior with neutral quenchers with small association constants arising from simultaneous static and dynamic quenching.[35] Given the absence of diffusional quenching for MV^{2+}, there must be a different origin for the present systems. Upward curvature is a common observation for polymer-based amplified quenching[6, 8] where it has been explained by invoking a "sphere of action" quenching mechanism[38] or as a result of aggregation of polymer fluorophores.[6] Superlinear behavior in the MOFs may arise from aggregation induced by neutralization of the negatively charged MOF surface by cationic quenchers. When samples are left unstirred, a suspension with added quencher settles faster than without quencher, which is consistent with surface association.

Emission quenching efficiencies for **2*** by MV^{2+} were investigated with added 0.1 M *tetra*-N-alkylammonium salts, $(NR_4)PF_6$. Steady-state SV plots, Figure 4-6a, were no longer superlinear. The magnitude of K_{SV} with added electrolyte increased with cation size in the

order: NMe_4^+ ($K_{SV} = 6.2 \times 10^4\ M^{-1}$) < N(*n*-butyl)$_4^+$ ($K_{SV} = 4.4 \times 10^5\ M^{-1}$) < N(*n*-hexyl)$_4^+$ ($K_{SV} = 2.4 \times 10^6\ M^{-1}$). This dependence is qualitatively consistent with stronger electrostatic interactions with surface carboxylate sites as the cation radius decreases presumably enhancing the surface ion exchange equilibrium, $-COO^-,NR_4^+ + MV^{2+} \leftrightarrow -COO^-,MV^{2+} + NR_4^+$.

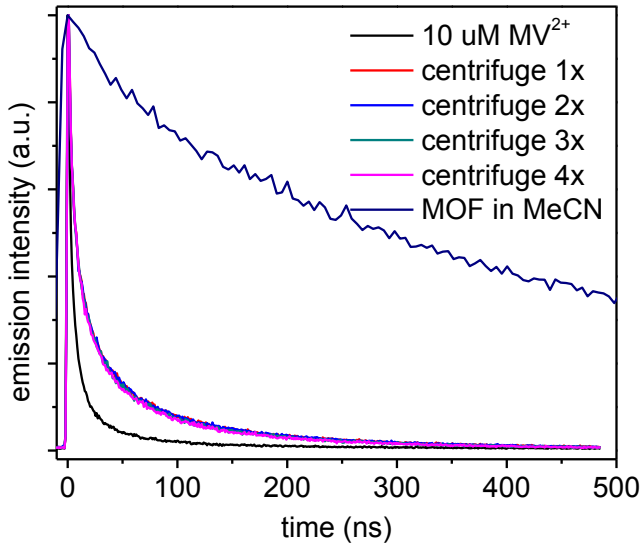

Figure 4-7. Time-resolved emission of **2** with 10 µM MV^{2+} in MeCN upon 485 nm excitation and 630 nm emission.

The time-resolved emission spectra of **2** with 10 µM MV^{2+} show slower decay kinetics after one MeCN wash but are unchanged after additional washing. The change in kinetics as a result of the first wash shows that dynamic quenching is occurring, however static quenching is still the dominant interaction.

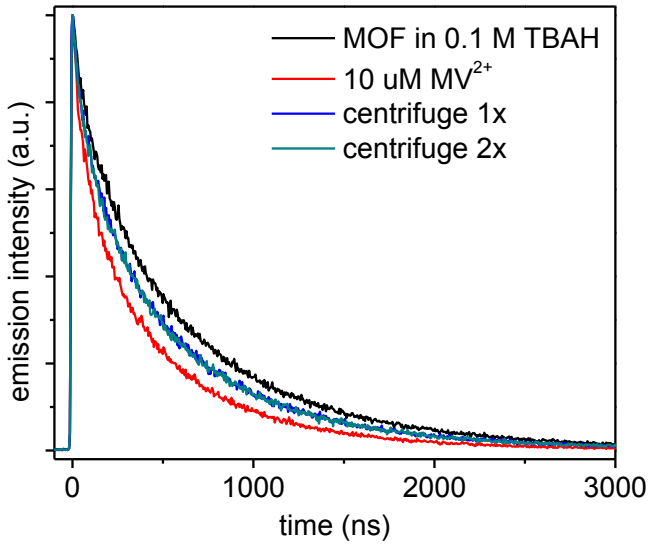

Figure 4-8. Time-resolved emission of **2** with 10 µM MV^{2+} in MeCN with 0.1M TBAH upon 485 nm excitation and 630 nm emission.

The time-resolved emission spectra of **2** with 10 µM MV^{2+} in MeCN with 0.1M TBAH shows slower decay kinetics after one 0.1 M TBAH in MeCN wash but is unchanged after additional washing. The change in kinetics as a result of the first wash shows that dynamic quenching is occurring, and static quenching plays less of a role because of the interaction between the MOF and the electrolyte.

4.3.3 Amplified Quenching of 2 with MB^+

Amplified quenching of **2*** by methylene blue cation (MB^+) was also observed. At a Ru concentration of 15 µM, $K_{SV} = 8.9 \times 10^6\ M^{-1}$. At [Ru] = 3 µM, K_{SV} increased to $2.7 \times 10^7\ M^{-1}$. Emission interferences occur for the quenching **2*** with MB^+, which are minimized by integrating the emission intensity from 750 to 850 nm . With MB^+, the MOF-quencher interaction can be easily observed by eye. Mixing of a MOF suspension and a methylene blue solution followed by centrifugation results in noticeable color loss in the supernatant and a change in color of the MOF microcrystals from bright orange-red to green.

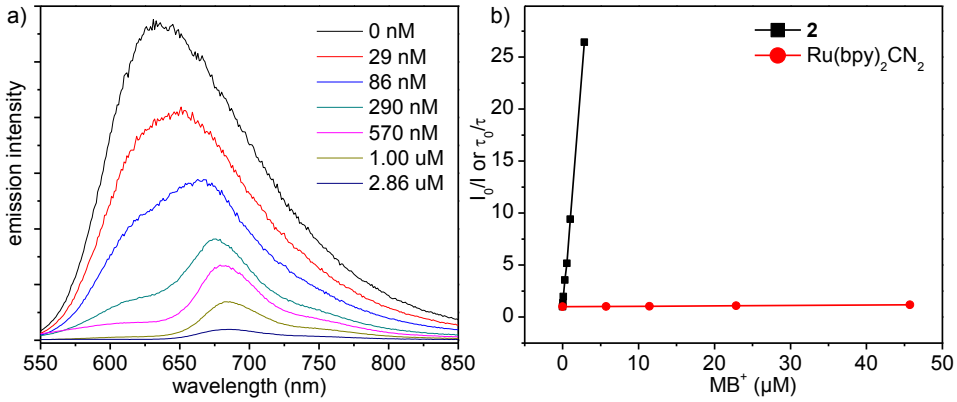

Figure 4-9. a) Steady-state emission of **2** (15 μM based on Ru) in acetonitrile with added methylene blue (MB^+) upon 420 nm excitation and b) Stern-Völmer analysis of **2** with added MB^+ by steady-state emission measurements and of $Ru(bpy)_2CN_2$ by time-resolved emission measurements. The emission intensity was integrated between 750-850 nm to minimize complications from absorption and emission from methylene blue. The first 50 ns after excitation were not included in the lifetime decay fits to avoid the contribution from methylene blue fluorescence at λ_{max} 676 nm.

A surface interaction constant for MB^+ and **2** (15 μM) was estimated by calculating the amount of surface-adsorbed dye by absorbance changes in the supernatant. Data acquired over the range of 1 - 3 μM MB^+, with fitting to a Langmuir model, gave $K = 7.5 \times 10^4\ M^{-1}$. With this value and the interpretation of K_{SV} for static quenching in eq 3, the excited state is estimated to sample ~120 surface sites during its lifetime. At MB^+ concentrations above 3 μM, the data deviate from Langmuir behavior apparently due to MB^+---MB^+ aggregation on the MOF surface. The onset of aggregation is evident by the appearance of emission at 570 nm. This observation is consistent with previous reports of ground state MB^+ aggregation leading to blue shifts in absorption and emission spectra.[39]

Even though the interaction of **2** with both MV^{2+} and MB^+ is irreversible, the powder X-ray diffraction pattern of **2** is unchanged after exposure to MB^+, consistent with a surface interaction without structural disruption by intercalation throughout the MOF framework.

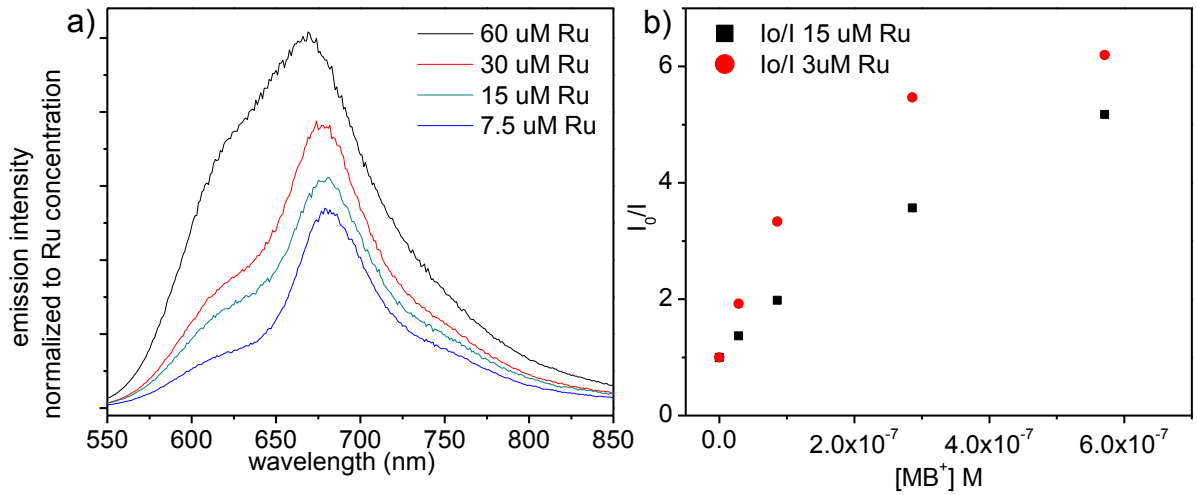

Figure 4-10. MOF concentration dependence with a) constant [MB^+] of 86 nM and MOF-**2** concentrations of 60, 30, 15, and 7.5 µM normalized to Ru concentration and b) steady-state Stern-Volmer plots with MOF-**2** concentrations of 15 or 3 µM and various MB^+ concentrations.

Emission interferences occur for the quenching **2*** with MB^+, which are minimized by integrating the emission intensity from 750 to 850 nm. The decrease in emission at the blue edge of the Ru spectrum is caused by an "inner filter" effect where the MB^+ absorbs a portion of the high energy Ru emission. Also a weak emission occurs from directly excited MB^+ at a λ_{max} around 680 nm with a tail extending to lower energy. The SV plot of **2**-Os with MB^+ does not have the same interference as **2** since the lower energy Os emission can be integrated from 850 to 950 nm. **2**-Os displays upward curvature as was observed with **2** quenched by MV^{2+}. It is expected that SV plot of **2** with added MB^+ would be upward curving if emission from directly excited MB^+ could be properly corrected. MB^+ absorption and emission spectra are reported in Figure 4-17.

The strong interaction of MB^+ with the MOF surface results in the concentration of MOF influencing the quenching efficiency. The graph in Figure 4-10a shows that when normalized to Ru concentration the extent of quenching is greater at low MOF

concentrations. At low MOF concentrations the quenching is more efficient because there are fewer binding sites to compete for association with a fixed number of quenchers.

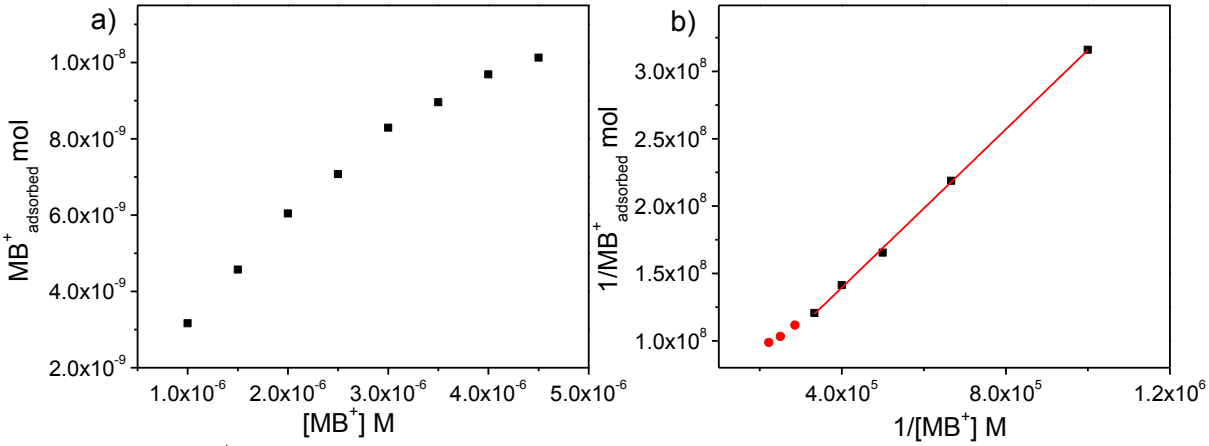

Figure 4-11. MB^+ formation constant calculation with **2** by a) supernatant absorbance analysis by a Langmuir model (equation 4-6) and b) fit of the data to the Lineweaver-Burk equation (equation 4-7).

$$\Gamma = \Gamma_{max} \frac{K_F[MB^+]}{1+K_F[MB^+]} \qquad \textbf{(eq 4-6)}$$

$$\frac{1}{\Gamma} = \frac{1}{\Gamma_{max}} + \frac{1}{\Gamma_{max}K_F[MB^+]} \qquad \textbf{(eq 4-7)}$$

The amount of MB^+ adsorbed onto the MOF surface was calculated by measuring the change in absorbance after mixing a certain concentration of MB^+ with 15µM **2** in 3.5 mL of MeCN. After mixing, the suspension was centrifuged to remove the MOF and the absorbance of the MB^+ remaining in solution was measured. The data was fit to eq 3 where Γ is the amount of MB^+ adsorbed onto the MOF in moles, Γ_{max} is the maximum amount adsorbed, and K_F is the formation constant per molar. As seen below in the PXRD, the adsorbed MB^+ does not change the structure of the MOF and is a result of interaction at the surface.

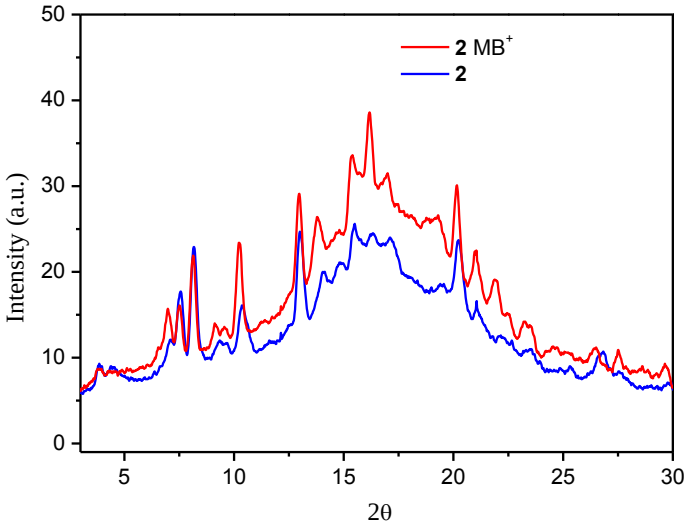

Figure 4-12. Powder X-ray diffraction pattern of **2** with MB^+.

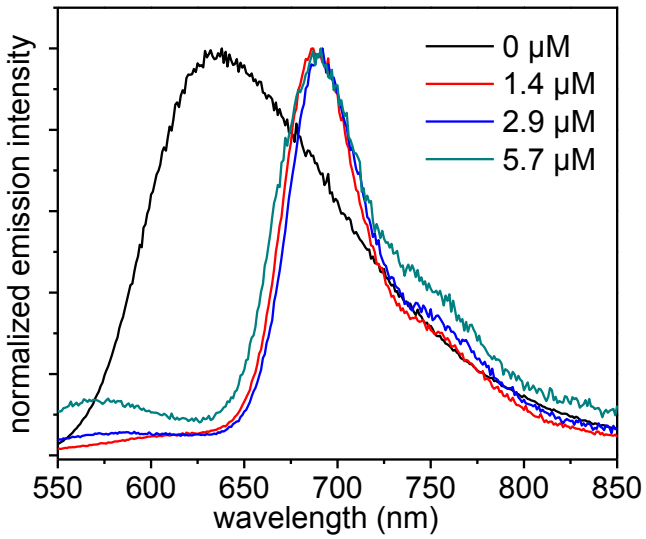

Figure 4-13. Normalized steady-state emission of **2** with added MB^+.

At concentrations above 3 μM the Langmuir model fails to accurately fit the amount of MB^+ adsorbed onto the MOF surface. This is likely the result of MB^+ aggregation which is evident by the growth in adduct emission at 570 nm.

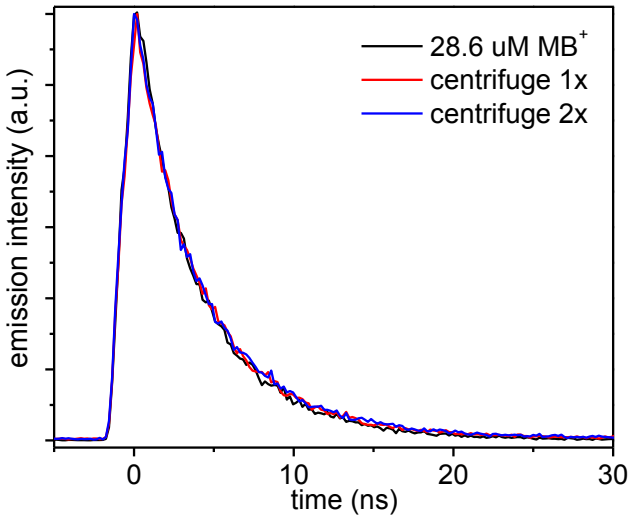

Figure 4-14. Time-resolved emission of **2** with 28.6 µM MB^+ in MeCN upon 445 excitation and 630 emission.

Time-resolved emission spectra of **2** with 28.6 µM MB^+ is unchanged after washing twice with fresh MeCN. This shows that dynamic quenching is not occurring and only static quenching needs to be considered.

Quenching of **2*** by MB^+, as with MV^{2+}, is probably by oxidative electron transfer. Quenching of the Os analog of **2** (**2**-Os) by MB^+ is also rapid and does occur by electron transfer. Energy transfer is unfavorable in this case since its thermally equilibrated excited state is too low in energy to undergo energy transfer to MB^+. The driving forces for electron transfer quenching for **2*** and **2***-Os should be comparable. Excited-state oxidation potentials for $Ru(bpy)_3^{2+}$* and $Os(bpy)_3^{2+}$* only differ by ~0.1 V.[40]

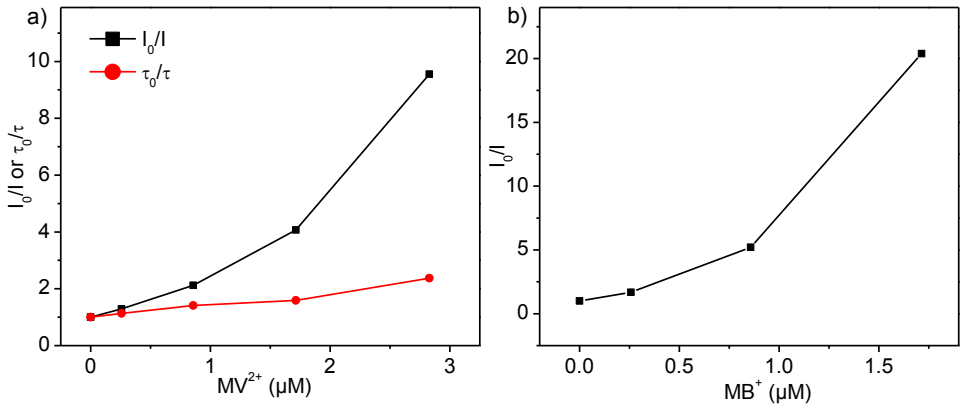

Figure 4-15. a) Steady-state and time-resolved SV plots for **2**-Os (15 μM based on Os) in acetonitrile with added MV^{2+} upon 485 nm excitation. The emission intensity was integrated from 650-950 and the decay was monitored at 740 nm. b) Steady-state SV plot of **2**-Os with added MB^+ in acetonitrile upon 420 nm excitation. The emission intensity was integrated from 850-950 nm to minimize complications from emission of methylene blue.

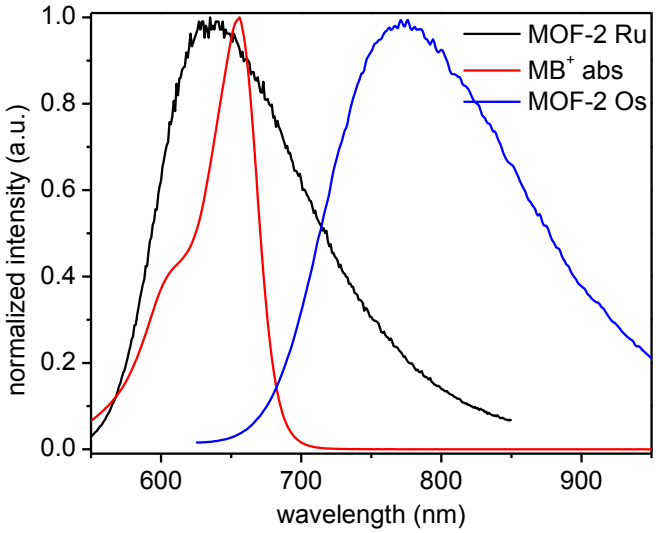

Figure 4-16. MOF-**2** Ru and Os emission overlap with MB^+ absorption.

The emission energy of the Ru MOF has significant spectral overlap with the absorption of methylene blue and therefore the quenching could occur by either an electron transfer or energy transfer quenching mechanism. However, the overlap of the Os MOF is much less and is still efficiently quenched. This suggests that electron transfer is the dominant quenching mechanism because the excited state reduction potentials of the Ru and Os MOFs are approximately equivalent.

2*-Os is quenched by both MV^{2+} and MB^{+} in acetonitrile at room temperature with $K_{SV} = 1.3 \times 10^6\ M^{-1}$ and $5.1 \times 10^6\ M^{-1}$, respectively. Upward curvature is also observed in the SV plots. The magnitudes of the SV constants in this case are half those for **2*** even though the emission lifetime decreases from 900 ns for **2*** to 30 ns for **2**-Os*. Based on Scheme 1, this observation points to a considerably enhanced rate of intra-MOF energy transfer for **2**-Os*, k_{EN} in eq 6, and a possible role for long-range singlet-singlet Förster transfer. Spin-orbit coupling is larger for Os with MLCT states ~30% singlet in character, promoting long-range dipole-dipole Förster transfer. Related observations have been made for energy transfer in crystalline solids.[41, 42] The relative rates for $Ru^{II}* \rightarrow Ru^{II}$ compared to $Os^{II}* \rightarrow Os^{II}$ energy transfer can be estimated based on the assumption that the K_{sv} is proportional to the number of energy transfer steps by the excited-state. The K_{SV} is equal to the product of the lifetime, the energy transfer rate, and a constant. The constant is dependent on the association constant, the rate of electron transfer, and the particle size. If these variables are assumed to be unchanged for the Ru and Os systems the relationship in Eq S7 holds. The equation can be rearranged in terms of a ratio of energy transfer rates and shows that Os to Os energy transfer is 12-17 times faster than Ru to Ru when experimental values are implemented.

$$K_{SV} = C * \tau * k_{en} \qquad \textbf{(eq 4-8)}$$

$$K_{SV\ Os} / \tau_{Os} * k_{en\ Os} = K_{SV\ Ru} / \tau_{Ru} * k_{en\ Ru} \qquad \textbf{(eq 4-9)}$$

$$k_{en\ Os} / k_{en\ Ru} = (K_{SV\ Os} * \tau_{Ru}) / (K_{SV\ Ru} * \tau_{Os}) \qquad \textbf{(eq 4-10)}$$

Quenching studies were also conducted on $Ru(bpy)_2CN_2$ with MB^{+} in order to estimate the degree of amplification of emission quenching in the MOF compared to the neutral model compound in solution (Figure 4-18). In order to accurately quantify the quenching efficiency in solution, K_{SV} was calculated from time-resolved data with the first

50 ns of data excluded to avoid MB^+ emission. The quenching of $Ru(bpy)_2CN_2$ by MB^+ in solution is far less efficient, with $K_{SV} = 3.9 \times 10^3\ M^{-1}$. Comparison with **2** gives an amplification factor of 7000 which is two orders of magnitude higher than those observed in earlier studies based on conjugated polymers with covalently linked Ru-bpy complexes.[16] This work thus demonstrates the remarkable ability of phosphorescent MOFs in amplifying luminescence quenching as a result of long-distance intra-MOF energy transfer and efficient electron transfer quenching at the interface. The tunability and crystalline structures of MOFs should allow for the design of systems for selective sensing of chosen analytes and merits further investigation.

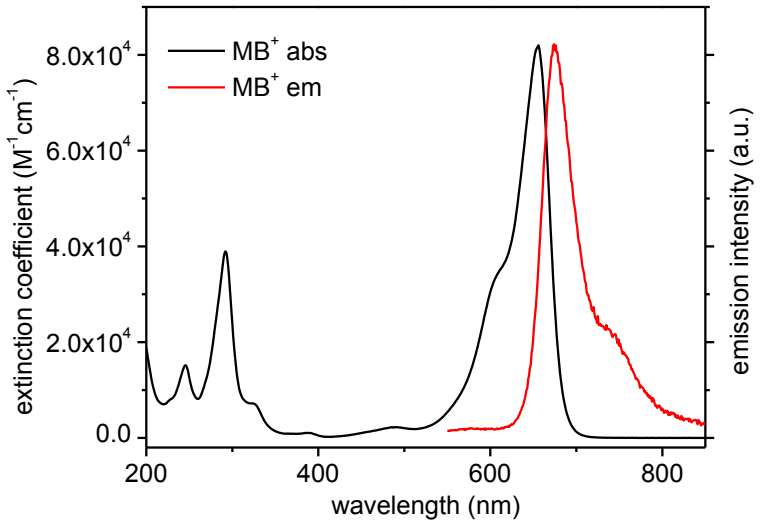

Figure 4-17. Absorption and emission of MB^+ in MeCN.

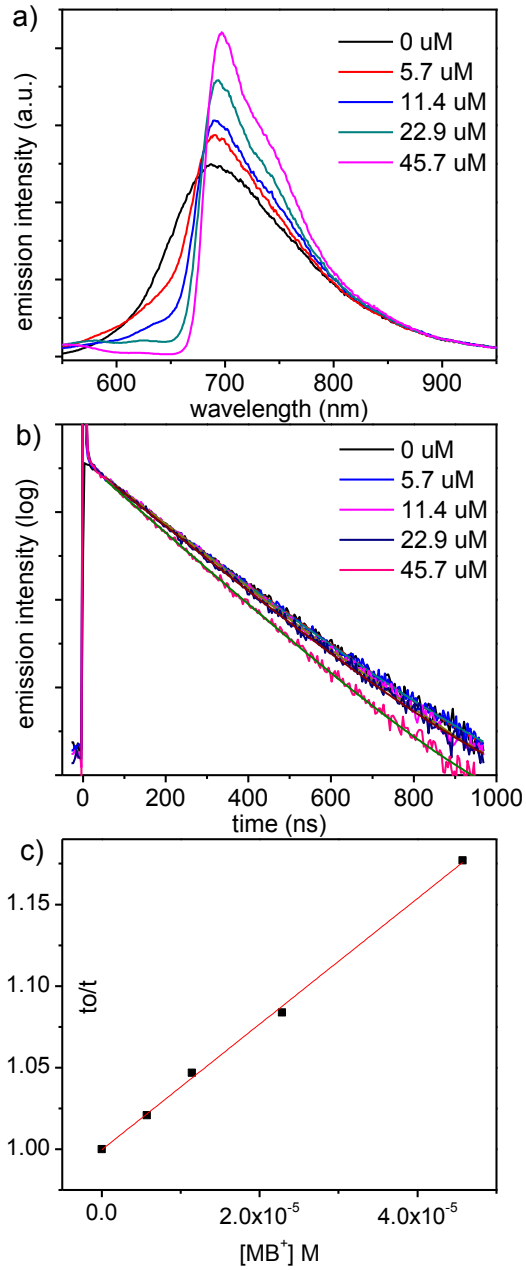

Figure 4-18. $Ru(bpy)_2CN_2$ with methylene blue in degassed acetonitrile (a) steady-state emission upon 420 nm excitation (b) time-resolved emission upon 445 nm excitation and monitoring emission at 700 nm (c) time-resolved Stern-Volmer analysis. The first 50 ns after excitation were not included in the fits to avoid methylene blue emission.

The direct excitation of MB^+ becomes significant at high concentrations and distorts the steady-state emission spectra. This problem can be avoided by measuring the emission lifetime and fitting the long component which corresponds to Ru emission.

4.4 Concluding Remarks

The light harvesting characteristics of the MOFs allow them to be utilized as highly responsive sensors by an amplified quenching mechanism with the highest triplet excited state quenching amplification in the literature. Strong noncovalent interactions between the MOF microcrystal surface and cationic quencher molecules coupled with rapid energy transfer through the MOF microcrystal facilitates amplified quenching with an enhancement of 7000-fold in the Stern-Völmer quenching constant compared to a model complex. With the synthetic tunability of MOFs it is likely that frameworks can be designed to have selective interactions with a desired analyte for further advancements in chemical sensing.

4.5 Experimental Section

After crystal growth, the MOF particles were washed with methanol and isolated by centrifugation three times and then washed with acetonitrile three more times. After soaking overnight in acetonitrile, the crystals were centrifuged once more to make a stock suspension with a concentration of 0.26 mM based on Ru. The Ru concentration was determined by adding 0.2 mL of the MeCN stock solution into 3.3 mL of 1M HCl and measuring the absorption spectrum. An aliquot of the MOF stock suspension in acetonitrile was combined with different amounts of quencher into quartz cuvettes and capped with septa. This procedure gave reproducible MOF concentration between samples and concentrations from a typical experiment are shown in Table S5.

Table 4-1. Sample preparation for quenching of **2** by MV^{2+}.

Sample	**2** stock in MeCN (mL)	MeCN (mL)	3.0 μM MV^{2+} in MeCN (mL)	Final [MV^{2+}] μM
1	0.2	3.3	0	0
2	0.2	3.0	0.3	0.257
3	0.2	2.3	1.0	0.857
4	0.2	1.3	2.0	1.714
5	0.2	0	3.3	2.829

The samples were degassed for 30 minutes by bubbling with argon (to remove any oxygen) prior to taking measurements. Solvent evaporation, which would result in concentration changes, was prevented by pre-saturating the argon with MeCN by passing argon through a fritted gas washing bubbler before the gas manifold. Magnetic stirring was used to keep the particles suspended so that the emission signal did not decrease from settling of the microcrystals. For the quenching experiments with MB^+, the steady-state emission and time-resolved data were collected by exciting at 420 and 445 nm, respectively. For the quenching experiments with MV^{2+}, the samples were excited at 485 nm. For MV^{2+}, the SV plots were generated from the integrated emission from 550-850 nm. For MB^+, the steady-state state SV plots are reported as the integrated intensity from 750-850 nm to avoid the region where MB^+ in solution acts as an inner filter on Ru emission. Long pass filters were used to eliminate light scattering artifacts.

Table 4-2. Biexponential fit parameters and average lifetime for **3** with added MV^{2+} in MeCN at 485 nm excitation and 670 nm emission.

$[MV^{2+}]$ M	A_1	τ_1	A_2	τ_2	$\langle\tau\rangle$ Lifetime (ns)
0.00	20.4	58.6	79.6	158	149.4
4.29E-06	20.6	25	79.4	118	113.2
1.43E-05	25	21.2	75	115	109.6
2.86E-05	25.6	20	74.4	113	107.7
4.71E-05	26	18.4	74	111	105.9
2.86E-04	23.4	16.2	76.6	104	100.0
5.71E-04	24.2	15	75.8	100	96.1
9.43E-04	26.8	15.4	73.2	98.5	94.0

Table 4-3. Triexponential fit parameters and average lifetime for **2** with added MV^{2+} in pure MeCN at 485 nm excitation and 630 nm emission.

$[MV^{2+}]$ μM	A_1	τ_1	A_2	τ_2	A_3	τ_3	$\langle\tau\rangle$ Lifetime (ns)
0	1.5	57.5	23.3	374	75.2	963	899
0.257	2.9	52.7	36.7	355	60.4	875	770
0.857	4.9	27.4	31.9	160	63.2	490	442
1.714	11.9	18.5	47	96.7	41.1	377	310
2.829	25	13.7	38.4	61.8	36.6	271	225

Table 4-4. Triexponential fit parameters and average lifetime for **2** with added MV^{2+} in 0.1 M TMAH at 485 nm excitation and 630 nm emission.

$[MV^{2+}]$ µM	A_1	τ_1	A_2	τ_2	A_3	τ_3	<τ> Lifetime (ns)
0	7.2	194	54.2	778	38.6	1507	1187
0.257	6.4	206	43.5	698	50.1	1391	1168
0.857	3.4	115	36.5	568	60.1	1273	1119
1.714	6.1	161	46.7	671	47.2	1351	1117
2.829	6.3	178	43.5	649	50.2	1276	1073

Table 4-5. Triexponential fit parameters and average lifetime for **2** with added MV^{2+} in 0.1 M TBAH at 485 nm excitation and 630 nm emission.

$[MV^{2+}]$ µM	A_1	τ_1	A_2	τ_2	A_3	τ_3	<τ> Lifetime (ns)
0	1.5	55.8	22.2	362	76.3	951	891
0.257	1.8	49	26.7	348	71.5	877	808
0.857	2.2	52	24.9	320	72.9	817	757
1.714	2.8	59	25.7	295	71.5	780	720
2.829	2.8	38.7	31	276	66.2	761	689

Table 4-6. Triexponential fit parameters and average lifetime for **2** with added MV^{2+} in 0.1 M THAH at 485 nm excitation and 630 nm emission.

$[MV^{2+}]$ µM	A_1	τ_1	A_2	τ_2	A_3	τ_3	<τ> Lifetime (ns)
0	1.6	48.7	19.4	326	79	915	867
0.257	2.5	40.7	26.1	252	71.4	700	647
0.857	6.9	40.3	35.3	212	57.8	598	526
1.714	7	25	33.2	143	59.8	493	442
2.829	8.7	21.6	36.2	133	55.1	492	435

Table 4-7. Triexponential fit parameters and average lifetime for **2**-Os with added MV^{2+} in MeCN at 485 nm excitation and 740 nm emission.

$[MV^{2+}]$ µM	A_1	τ_1	A_2	τ_2	A_3	τ_3	<τ> Lifetime (ns)
0	5.3	4.4	43.5	18.1	51.2	35.3	29.9
0.257	5.8	3.4	41.6	14.8	52.6	30.9	26.3
0.857	6.5	2.2	47.7	10.7	45.8	25.9	21.2
1.714	13.5	1.9	48.6	8.4	37.9	23.9	18.8
2.829	16.6	1.1	44.1	4.7	39.3	15.6	12.6

Table 4-8. Lifetime for $Ru(bpy)_2CN_2$ with added MB^+ in MeCN at 445 nm excitation and 700 nm emission.

$[MB^+]$ µM	Lifetime (ns)
0	246
5.71	241
11.4	235
22.9	227
45.7	209

4.6 References

1. Zhou, Q.; Swager, T. M., Fluorescent chemosensors based on energy migration in conjugated polymers: The molecular wire approach to increased sensitivity. *Journal of the American Chemical Society* 1995, 117, 12593-12602.

2. Yang, J. S.; Swager, T. M., Porous shape persistent fluorescent polymer films: An approach to TNT sensory materials. *Journal of the American Chemical Society* 1998, 120, 5321-5322.

3. Yang, J. S.; Swager, T. M., Fluorescent porous polymer films as TNT chemosensors: Electronic and structural effects. *Journal of the American Chemical Society* 1998, 120, 11864-11873.

4. Narayanan, A.; Varnavski, O. P.; Swager, T. M.; Goodson, T., III, Multiphoton fluorescence quenching of conjugated polymers for TNT detection. *Journal of Physical Chemistry C* 2008, 112, 881-884.

5. McQuade, D. T.; Pullen, A. E.; Swager, T. M., Conjugated polymer-based chemical sensors. *Chemical Reviews* 2000, 100, 2537-2574.

6. Thomas, S. W., III; Joly, G. D.; Swager, T. M., Chemical sensors based on amplifying fluorescent conjugated polymers. *Chemical Reviews* 2007, 107, 1339-1386.

7. Liu, Y.; Ogawa, K.; Schanze, K. S., Conjugated polyelectrolytes as fluorescent sensors. *Journal of Photochemistry and Photobiology C-Photochemistry Reviews* 2009, 10, 173-190.

8. Chen, L. H.; McBranch, D. W.; Wang, H. L.; Helgeson, R.; Wudl, F.; Whitten, D. G., Highly sensitive biological and chemical sensors based on reversible fluorescence quenching in a conjugated polymer. *Proceedings of the National Academy of Sciences of the United States of America* 1999, 96, 12287-12292.

9. Tan, C. Y.; Pinto, M. R.; Schanze, K. S., Photophysics, aggregation and amplified quenching of a water-soluble poly(phenylene ethynylene). *Chemical Communications* 2002, 446-447.

10. Fan, C. H.; Plaxco, K. W.; Heeger, A. J., High-efficiency fluorescence quenching of conjugated polymers by proteins. *Journal of the American Chemical Society* 2002, 124, 5642-5643.

11. Fan, C. H.; Wang, S.; Hong, J. W.; Bazan, G. C.; Plaxco, K. W.; Heeger, A. J., Beyond superquenching: Hyper-efficient energy transfer from conjugated polymers to gold nanoparticles. *Proceedings of the National Academy of Sciences of the United States of America* 2003, 100, 6297-6301.

12. Achyuthan, K. E.; Bergstedt, T. S.; Chen, L.; Jones, R. M.; Kumaraswamy, S.; Kushon, S. A.; Ley, K. D.; Lu, L.; McBranch, D.; Mukundan, H.; Rininsland, F.; Shi, X.; Xia, W.; Whitten, D. G., Fluorescence superquenching of conjugated polyelectrolytes: applications for biosensing and drug discovery. *Journal of Materials Chemistry* 2005, 15, 2648-2656.

13. Jones, R. M.; Lu, L. D.; Helgeson, R.; Bergstedt, T. S.; McBranch, D. W.; Whitten, D. G., Building highly sensitive dye assemblies for biosensing from molecular building blocks. *Proceedings of the National Academy of Sciences of the United States of America* 2001, 98, 14769-14772.

14. Tan, C. Y.; Alas, E.; Muller, J. G.; Pinto, M. R.; Kleiman, V. D.; Schanze, K. S., Amplified quenching of a conjugated polyelectrolyte by cyanine dyes. *Journal of the American Chemical Society* 2004, 126, 13685-13694.

15. Haskins-Glusac, K.; Pinto, M. R.; Tan, C. Y.; Schanze, K. S., Luminescence quenching of a phosphorescent conjugated polyelectrolyte. *Journal of the American Chemical Society* 2004, 126, 14964-14971.

16. Liu, Y.; Jiang, S. J.; Schanze, K. S., Amplified quenching in metal-organic conjugated polymers. *Chemical Communications* 2003, 650-651.

17. Fleming, C. N.; Maxwell, K. A.; DeSimone, J. M.; Meyer, T. J.; Papanikolas, J. M., Ultrafast excited-state energy migration dynamics in an efficient light-harvesting antenna polymer based on Ru(II) and Os(II) polypyridyl complexes. *J Am Chem Soc* 2001, 123, 10336-47.

18. Seo, J. S.; Whang, D.; Lee, H.; Jun, S. I.; Oh, J.; Jeon, Y. J.; Kim, K., *Nature* 2000, 404, 982.

19. Evans, O. R.; Lin, W., *Acc. Chem. Res.* 2002, 35, 511.

20. Kitagawa, S.; Kitaura, R.; Noro, S.-I., *Angew. Chem. Int. Ed.* 2004, 43, 2334.

21. Kaye, S. S.; Dailly, A.; Yaghi, O. M.; Long, J. R., *J. Am. Chem. Soc.* 2007, 129, 14176.

22. Farha, O. K.; Hupp, J. T., *Acc. Chem. Res.* 2010, 43, 1166.

23. Chen, B.; Wang, L.; Xiao, Y.; Fronczek, F. R.; Xue, M.; Cui, Y.; Qian, G., *Angew. Chem. Int. Ed.* 2009, 48, 500.

24. Furukawa, H.; Ko, N.; Go, Y.-B.; Aratani, N.; Choi, S. B.; Choi, E.; Yazaydin, A. O.; Snurr, R. Q.; O'Keeffe, M.; Kim, J.; Yaghi, O. M., *Science* 2010, 329, 424.

25. Rieter, W. J.; Taylor, K. M. L.; An, H.; Lin, W.; Lin, W., *J. Am. Chem. Soc.* 2006, 128, 9024.

26. Rieter, W. J.; Pott, K. M.; Taylor, K. M. L.; Lin, W., *J. Am. Chem. Soc.* 2008, 130, 11584.

27. Ma, L.; Falkowski, J. M.; Abney, C.; Lin, W., *Nat. Chem.* 2010, 2.

28. Lan, A.; Li, K.; Wu, H.; Olsson, D. H.; Emge, T. J.; Ki, W.; Hong, M.; Li, J., *Angew. Chem. Int. Ed.* 2009, 48, 2334.

29. Li, J.-R.; Kuppler, H.-C.; Zhou, H.-C., *Chem. Soc. Rev.* 2009, 38, 1477.

30. Wu, C.-D.; Hu, A.; Zhang, L.; Lin, W., *J. Am. Chem. Soc.* 2005, 127, 8940.

31. Xie, Z.; Ma, L.; deKrafft, K. E.; Jin, A.; Lin, W., *J. Am. Chem. Soc.* 2009, 132, 922.

32. D'Alessandro, D. M.; Smit, B.; Long, J. R., *Angew. Chem. Int. Ed.* 2010, 49, 6058.

33. Shustova, N. B.; McCarthy, B. D.; Dinca, M., *Journal of the American Chemical Society*, ASAP.

34. Kent, C. A.; Mehl, B. P.; Ma, L. Q.; Papanikolas, J. M.; Meyer, T. J.; Lin, W. B., Energy Transfer Dynamics in Metal-Organic Frameworks. *Journal of the American Chemical Society* 2010, 132, 12767-12769.

35. Kent, C. A.; Liu, D.; Ma, L.; Papanikolas, J. M.; Meyer, T. J.; Lin, W., Light Harvesting in Microscale Metal-Organic Frameworks by Energy Migration and Interfacial

Electron Transfer Quenching. *Journal of the American Chemical Society* 2011, 133, 12940-12943.

36. Spek, A. L., Single-crystal structure validation with the program PLATON. *Journal of Applied Crystallography* 2003, 36, 7-13.

37. Bock, C. R.; Meyer, T. J.; Whitten, D. G., ELECTRON-TRANSFER QUENCHING OF LUMINESCENT EXCITED-STATE OF TRIS(2,2'-BIPYRIDINE)RUTHENIUM(II) - FLASH-PHOTOLYSIS RELAXATION TECHNIQUE FOR MEASURING RATES OF VERY RAPID ELECTRON-TRANSFER REACTIONS. *Journal of the American Chemical Society* 1974, 96, 4710-4712.

38. Wang, J.; Wang, D. L.; Miller, E. K.; Moses, D.; Bazan, G. C.; Heeger, A. J., Photoluminescence of water-soluble conjugated polymers: Origin of enhanced quenching by charge transfer. *Macromolecules* 2000, 33, 5153-5158.

39. Severino, D.; Junqueira, H. C.; Gugliotti, M.; Gabrielli, D. S.; Baptista, M. S., Influence of negatively charged interfaces on the ground and excited state properties of methylene blue. *Photochemistry and Photobiology* 2003, 77, 459-468.

40. Hoselton, M. A.; Lin, C. T.; Schwarz, H. A.; Sutin, N., KINETICS AND MECHANISM OF QUENCHING OF EMISSION OF SUBSTITUTED POLYPYRIDINERUTHENIUM(II) COMPLEXES - REACTIONS OF RUL3+, STARRUL-3(2+), AND RUL-3(3+) WITH COPPER(I)-COPPER(II) COUPLE. *Journal of the American Chemical Society* 1978, 100, 2383-2388.

41. von Arx, M. E.; Burattini, E.; Hauser, A.; van Pieterson, L.; Pellaux, R.; Decurtins, S., Luminescence and energy transfer of Ru(bpy)(3) (2+), Cr(ox)(3) (3-), and Os(bpy)(3) (2+) in three-dimensional oxalato-networks. *Journal of Physical Chemistry A* 2000, 104, 883-893.

42. Sewell, G.; Forster, R. J.; Keyes, T. E., Influence of steric confinement within zeolite Y on photoinduced energy transfer between Ru(bpy)(3) (2+) and iron polypyridyl complexes. *Journal of Physical Chemistry A* 2008, 112, 880-888.

CHAPTER 5

THERMAL POPULATION OF A LIGAND-BASED TRIPLET IN $[Ru^{II}(bpy)_2(phendione)]^{2+}$ AT ROOM TEMPERATURE

5. 1 Introduction to Singlet-Triplet Gaps in Organic Molecules

Organic triplet states have long been studied photochemically, and are of particular interest in the emerging fields of spintronics and molecular electronics for their magnetic properties and the ease of synthetic manipulation of organic systems. Typically these states are only accessible via photoexcitation, as the singlet-triplet (S-T) energy gaps for Kekulé-structures are on the order of 12,000-20,000 cm^{-1}. These states can be stabilized through synthetic modification and careful molecular design thus modulating the molecular orbital coefficients, extending the conjugation and reducing the HOMO-LUMO gap, or introducing some level of strain. Even with the litany of stabilization motifs available to the synthetic chemist, very few Kekulé structures present thermally accessible triplet states, requiring S-T gaps less than ca. 2000 cm^{-1}. Wirz and coworkers have prepared highly conjugated napthoquinodimethane derivatives with S-T gaps on the order of 500-1000 cm^{-1}, with one such example even favoring a triplet ground state.[1] Others involve elaboration of the *para*-quinodimethane core, offering conjugated systems with thermally accessible S-T gaps.[2] However, often these systems suffer from instability to high temperatures, oxygen, and light which limits their potential in a more robust device configuration.

5. 2 Observation of a Thermally Populated Triplet in $[Ru^{II}(bpy)_2(phendione)]^{2+}$

We report here on the unexpected observation of paramagnetic character in the stable complex $[Ru^{II}(bpy)_2(pd)](PF_6)_2$ (**5**, bpy = 2,2′-bipyridine, pd = 1,10-phenanthroline-5,6-dione, or phendione) and initial investigations into the origin of the paramagnetism.[3] Complex **5** is a widely utilized precursor for preparing more elaborate ligand systems[4, 5] and the electrochemistry has been previously reported.[3] Our initial interest in this system was exploitation of the $[Ru^{III}(bpy)_2(pd^{\bullet-})]^{2+}$ excited state towards proton-coupled electron transfer, in a similar fashion to that studied previously in $[Ru^{II}(bpy)_2(bpz)]^{2+}$.[6, 7] Initial studies concluded that the lifetime of the $[Ru^{III}(bpy)_2(pd^{\bullet-})]^{2+}$ state is extremely short-lived due to rapid intramolecular quenching because it was not observable by ns transient absorption (10 ns time resolution). As such its action in PCET could not be probed; however, these studies led to the discovery of previously unreported phenomenon of paramagnetic character.

5.2.1 Emission Studies in Solution

Complex **5** is very weakly emissive in acetonitrile solution (57 μM) with a λ_{max} of ca. 640 nm and a lifetime of 748 ns. Although this emission appears structurally similar to $[Ru^{II}(bpy)_3]^{2+}$, a potential impurity in the synthesis, the behavior of the emission observed for **5** with added water is clearly different than $[Ru^{II}(bpy)_3]^{2+}$. Surprisingly, with increasing water concentration, the emission gains intensity and presents a bathochromic shift, while the single exponential lifetime decreases. By the energy gap law,[8] the decrease in lifetime is consistent with this bathochromic shift as a result of faster non-radiative decay processes. However, the increase in intensity is inconsistent with a shorter lifetime, as the quantum yield and lifetime are directly proportional. This observation can be explained by the formation of an emissive species by a chemical reaction of **5** with water forming a monohydrated

phendione (**5a**), where one molecule of water adds across one half of the dione, affording a ketone/diol. This addition product breaks the quinoid core conjugation and greatly reduces the electron accepting ability, thus turning on emission. The hydration chemistry of phendione has been characterized previously by NMR and electrochemical methods, but is only observed when N-coordinated to metals or a proton, activating the dione to attack.[9-11] As a result of hydration, the reduction potentials of coordinated phendione-OH_2 shift much higher relative to the mild potentials of coordinated-phendione, rendering it less effective at quenching the ^{3}MLCT excited state in **5a**. It is likely that the minor emission observed in "pure" acetonitrile originates from this hydrated complex, rather than the phendione complex, due to the presence of trace water (ca. 0.5 mM in standard acetonitrile). This explains the observed emission behaviors, where the facile quenching observed for **5** is thought to be an intramolecular oxidative quenching mechanism to the dione (*o*-benzoquinone mimic), a quenching pathway removed in **5a**.

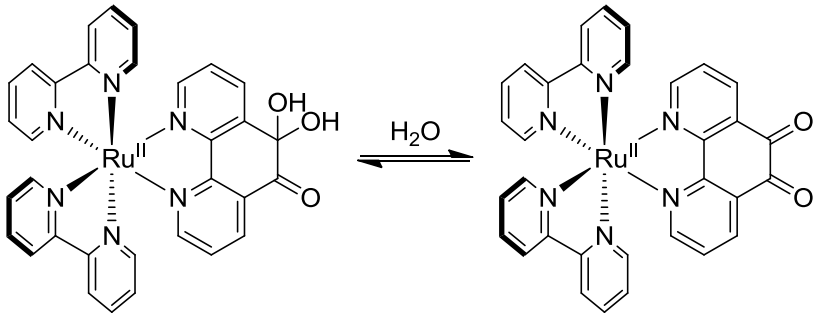

5a **5**

Figure 5-1. Hydration equilibrium of $[Ru^{II}(bpy)_2(phendione)]^{2+}$

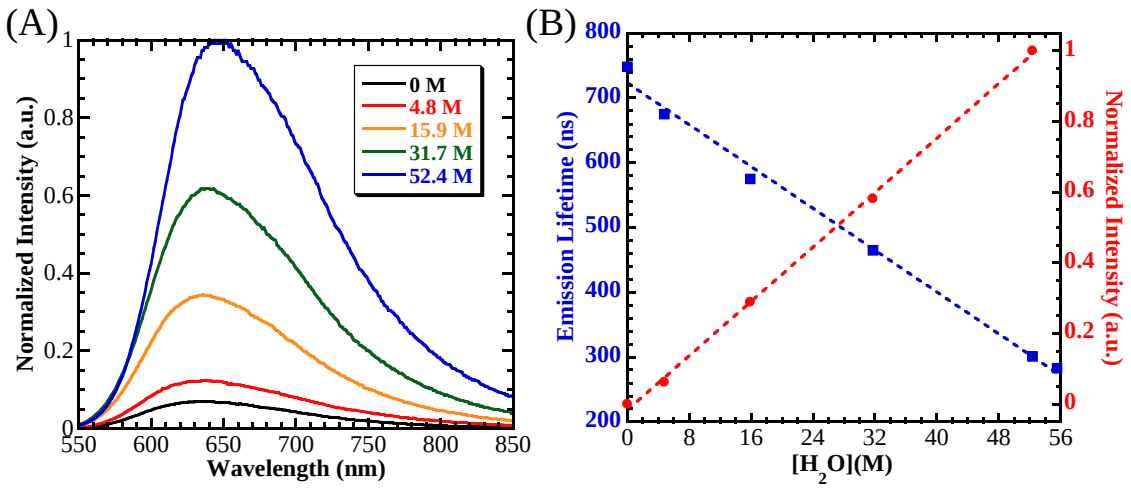

Figure 5-2. $[Ru^{II}(bpy)_2(phendione)]^{2+}$ (a) emission spectra and (b) lifetime and intensity versus water concentration.

5.2.2 Nuclear Magnetic Resonance Studies

When **5**, purified by Sephadex chromatography and multiple recrystallizations, is dissolved in anhydrous d^3-acetonitrile at 10 mM, the ^{1}H-NMR spectrum is sharp, and all of the expected proton signals are present (blue, Figure 5-3).[5] If that same purified sample is dissolved in D_2O, the NMR spectrum dramatically changes, with broadening of several resonances and the appearance of minor features associated with species **5a** from the chemical equilibrium process (black, Figure 5-3). Interestingly, if the concentration is reduced to 1 mM in anhydrous d^3-acetonitrile (red, Figure 5-3), the three phendione signals are broadened significantly, while the bpy signals remain sharp and unshifted (a similar effect is observed in d^6-DMSO, Figure 5-4).

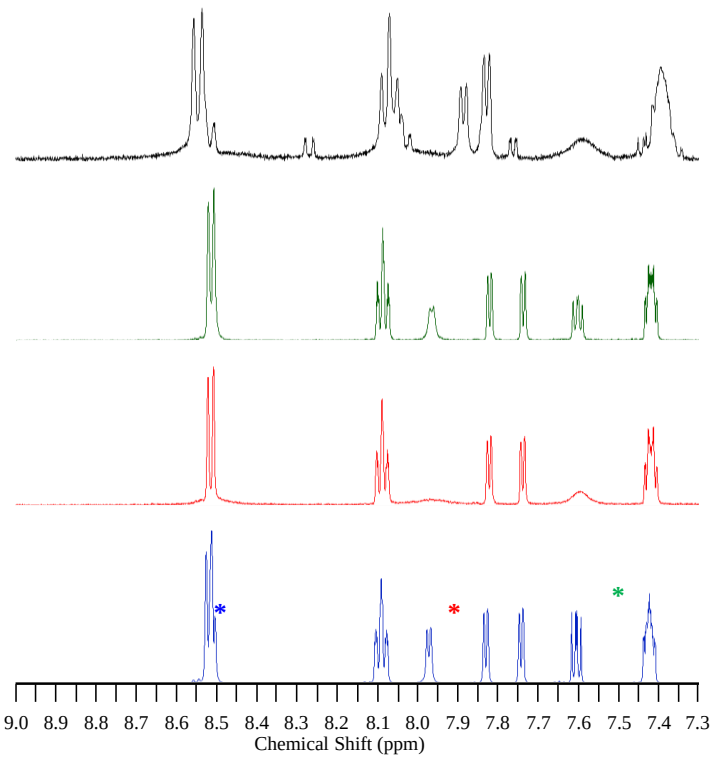

Figure 5-3. ^{1}H-NMR spectra of $[Ru^{II}(bpy)_2(phendione)]^{2+}$ collected at 10 mM in CD_3CN (blue), 1 mM in CD_3CN (red), 1 mM in CD_3CN/0.25% D_2O (green), and in D_2O (black). Asterisks correspond to the phendione protons as labeled in Figure 5-4.

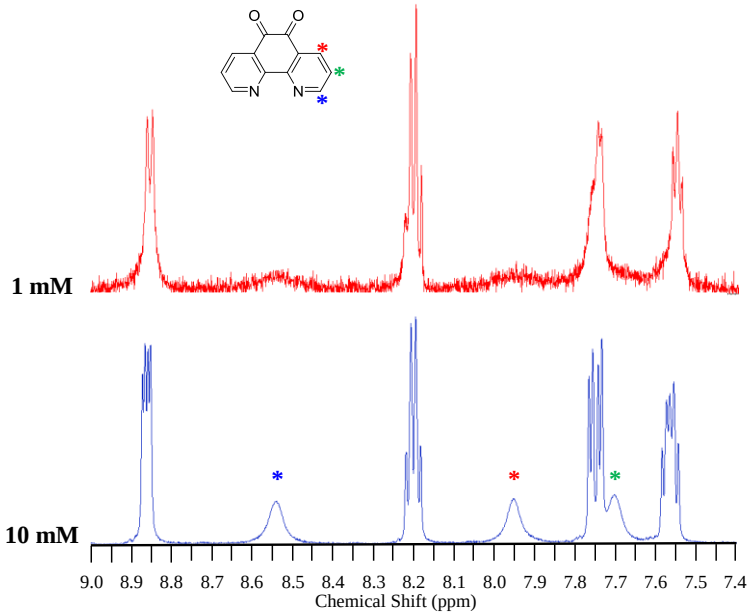

Figure 5-4. ^{1}H-NMR spectra of $[Ru^{II}(bpy)_2(phendione)]^{2+}$ collected at 10 mM (blue) and 1 mM (red) in DMSO. Asterisks correspond to the phendione protons.

The broadening of the phendione signals in the 1 mM d^3-acetonitrile sample could be reduced, nearly returning the original diamagnetic spectrum, with the addition of as little as 0.25% D_2O (green, Figure 5-3), note that the water concentration is low enough that neither the equilibrium product nor peak shifts are observed. This broadening follows an opposite concentration dependence than that typically observed due to non-covalent interactions, and suggests paramagnetic character as an origin of the broadening. A similar localized broadening effect in the NMR was recently reported by Nakamura, et. al. for a quinodimethane derivative as a consequence of a thermally populated triplet state.[2] The broadening behavior in the ^{1}H-NMR of **5** is clearly linked to both substrate concentration and the presence of water, the latter of which had a dramatic effect on the emission spectra. The presence of a phendione-localized thermally populated triplet (**5b**) could provide both a rapid relaxation mechanism for the photophysics, in the absence of water, as well as a broadening mechanism for the NMR in dilute solution, as high concentrations could lead to spin relaxation phenomena affording a diamagnetic NMR. However, DFT calculations place the lowest lying triplet as a phendione localized biradical with a calculated singlet-triplet gap of 13,000 cm^{-1}, appropriate for an organic S-T gap, and far beyond the thermally accessible regime.

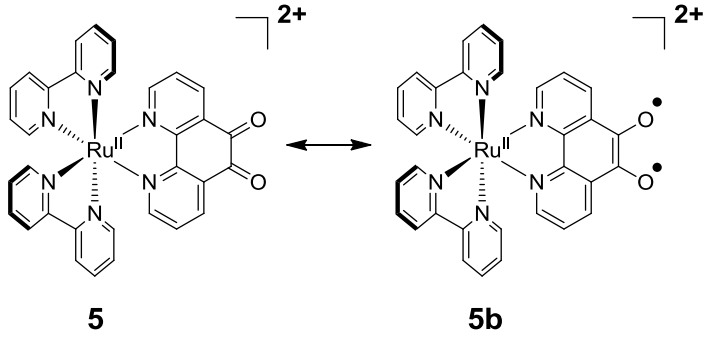

Figure 5-5. Singlet-triplet equilibrium of $[Ru^{II}(bpy)_2(phendione)]^{2+}$.

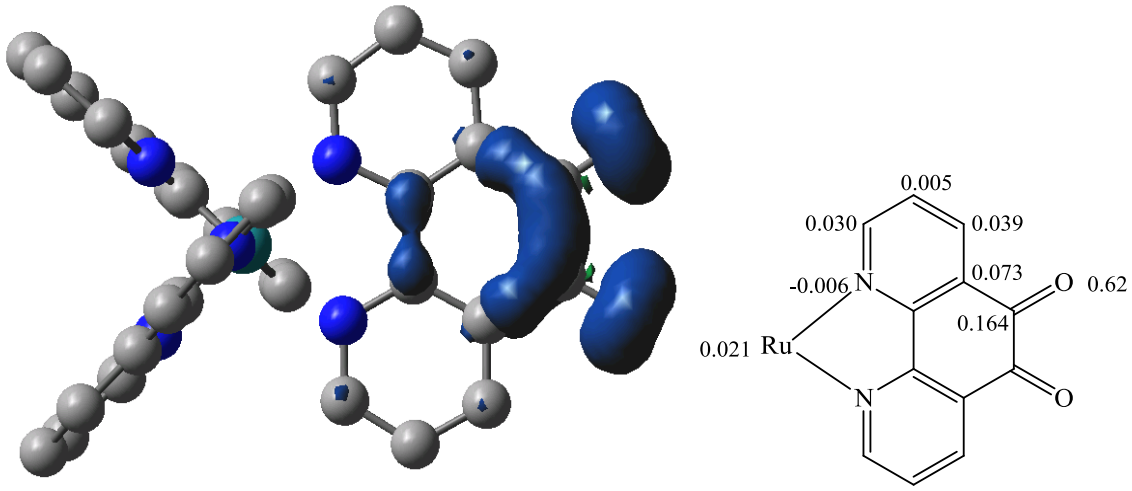

Figure 5-6. Spin density calculated at the B3LYP/6-31G* level for the lowest lying triplet state of $[Ru^{II}(bpy)_2(phendione)]^{2+}$ (**5b**), a dione centered biradical state. Positive spin density in blue, negative spin density in green. The numerical values for the Mulliken spin densities for phendione are shown.

To probe any temperature dependence on the broadening observed, variable temperature ^{1}H-NMR was collected on a 1 mM sample of **5** in d^3-acetonitrile, from 260 K – 340 K. At temperatures below ca. 290 K, the phendione resonances sharpen, affording the expected diamagnetic NMR spectrum. As the temperature is increased, these three peaks begin to broaden, at different rates, and there is an apparent downfield shift of all the bipyridine proton resonances, again with a different magnitude. Interestingly, a residual water peak appears between ca. 2.29 ppm and 1.97 ppm, which demonstrates a steady ca. 0.04 ppm/10 K upfield shift with increasing temperature. This is likely a manifestation of the **5-5a** equilibrium, dynamic on the NMR timescale at low concentrations of water, which is shifted towards **5** with increasing temperature. This temperature dependent broadening and observed shifts in the bpy-proton resonances suggest the possibility of a paramagnetic species.

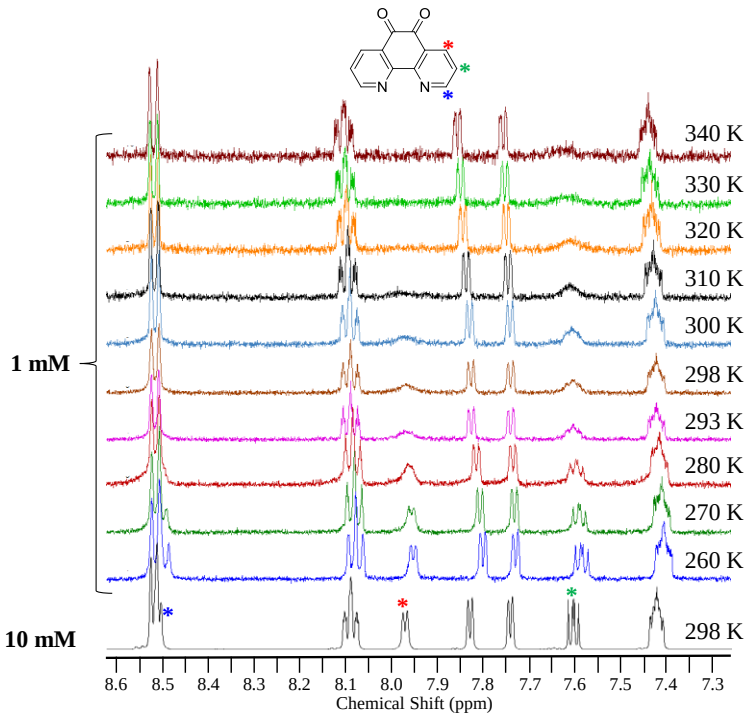

Figure 5-7. VT-^{1}HNMR for a 1 mM sample of **5** in d^3-acetonitrile collected from 260 K to 340 K. 10 mM sample at 298 K shown for reference, starred peaks highlight phendione protons. All spectra are referenced to CD_2HCN.

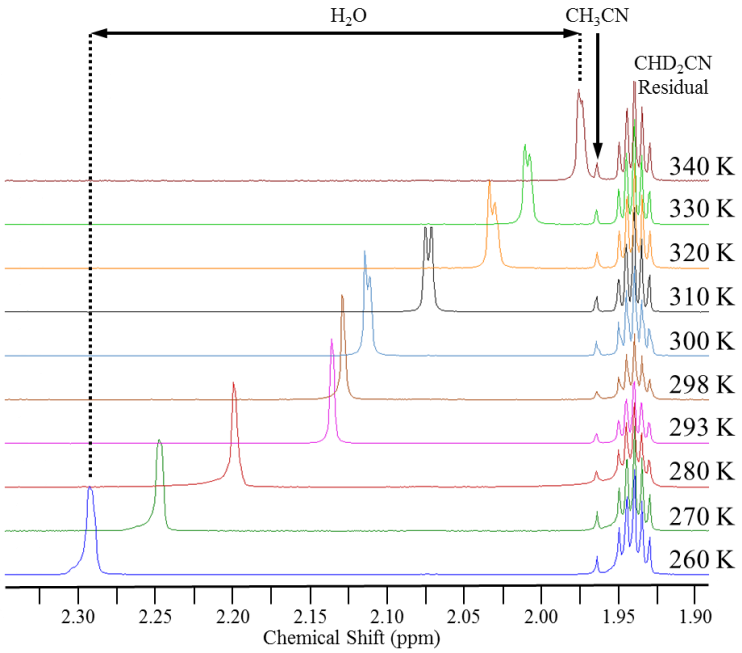

Figure 5-8. VT-^{1}HNMR for a 1 mM sample of **5** in d^3-acetonitrile collected from 260 K to 340 K in the range 2.40 – 2.00 ppm illustrating the large temperature-dependent chemical shift dependence for a water peak. Peak assigned to H_2O in the NMR solvent following 0.25% spike with H_2O.

5.2.3 Electron Paramagnetic Resonance Studies

Following the photophysical and NMR observations, complex **5** was studied in both solid and solution state by EPR spectroscopy at X-band. Initial experiments on the powder reveal an anisotropic, featureless signal centered at ca. g = 2.005 with a total spectral width of ca. 25 G, typical for an organic radical. When a sample of **5** is dissolved in anhydrous acetonitrile, a similar, symmetric signal is observed with no resolvable fine structure; an analogous spectrum is obtained in DMSO, with a stronger intensity. Given the unexpected concentration dependence demonstrated in the NMR experiments, a similar profile was examined by EPR. For a paramagnetic impurity at low concentration (< 5 mM) in the absence of significant intermolecular interactions, one would expect the spectral intensity to scale linearly with concentration. Figure 5-10A presents the spectral evolution from an initial concentration of 5 mM; dilution of the sample with anhydrous acetonitrile affords a sharp *increase* in the spectral intensity, before falling off, due primarily to low concentrations (ca. 0.01 mM) reaching the detection limit of the instrument.

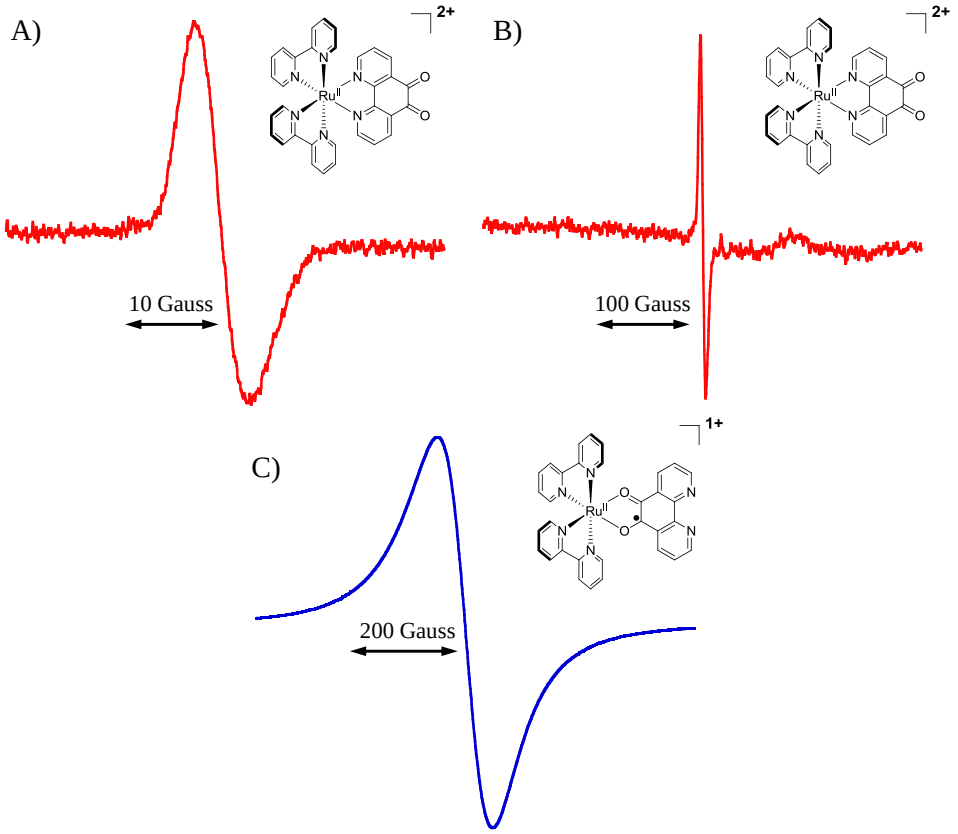

Figure 5-9. Room temperature (293 K) EPR spectra for powder samples collected at a center field of 3363.87 G, modulation of 5 G, sweep time of 2 min, time constant of 0.1 s and 3 scan average: (A) **5** at a 50 G sweep width, 2000 gain setting, (B) **5** at a 500 G sweep width, 2000 gain setting, and (C) **6** at an 800 G sweep, 100 gain setting.

In a separate experiment, two samples of **5** were prepared at ca. 1 mM in CD_3CN – one anhydrous and one with ca. 0.25% D_2O. ^{1}H-NMR were first collected, demonstrating the broadened spectrum attributed to paramagnetism in the anhydrous sample, and the sharpened spectrum expected for the diamagnetic complex in the 'wet' sample. The NMR samples were then taken directly to the EPR for measurement and a significant paramagnetic signal was observed for the anhydrous sample while virtually no signal could be detected in the wet sample (Figure 5-10B). This result links the appearance of broadening in the phendione resonances observed by NMR to the presence of a paramagnetic signal in the EPR. The paramagnetism can be subsequently eliminated in the presence of D_2O, thus

restoring the diamagnetic NMR spectrum observed at higher concentrations. The minor EPR signals observed for both the wet and >5 mM anhydrous samples would likely not greatly affect the NMR spectrum, given the higher sensitivity of EPR over NMR.

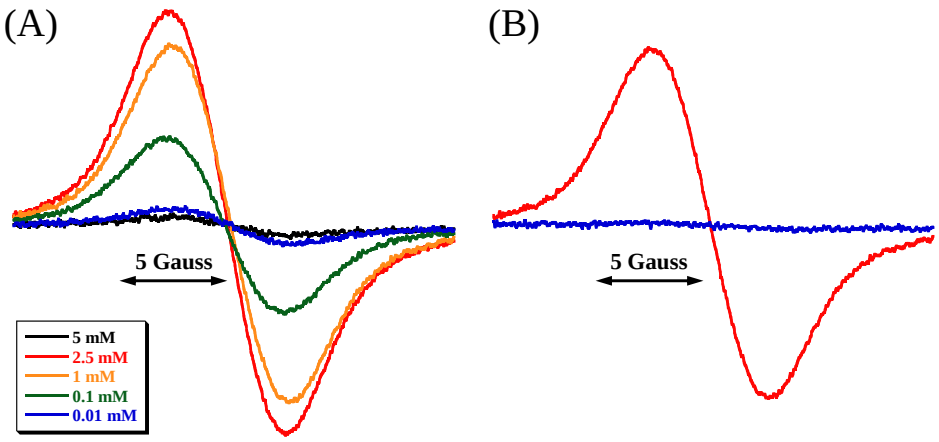

Figure 5-10. Initial EPR spectra of **5**: (A) Concentration dependence of EPR signal intensity, (B) 1 mM CD_3CN NMR Sample (red) vs. 1 mM CD_3CN/0.25% D_2O NMR sample (blue).

With a direct correlation of the behavior observed in the NMR and EPR spectra, the origin of the paramagnetism is probed with variable temperature techniques to complement the VT-^{1}HNMR results. VT-EPR on **5** in a 1 mM solution in anhydrous acetonitrile reveals a strong temperature dependence on the intensity of the EPR signal (Figure 5-11), while the total spectral width and peak-peak distance remains unchanged. Note that at only ca. 278 K the signal approaches baseline. The thermal-induced behaviors are consistent with magnetometry results for **5**, which demonstrate a temperature dependence to χ_{para}•T and suggest a large χ_{TIP}, tending towards zero at low temperature, indicative of a singlet ground state (Figure 5-12).

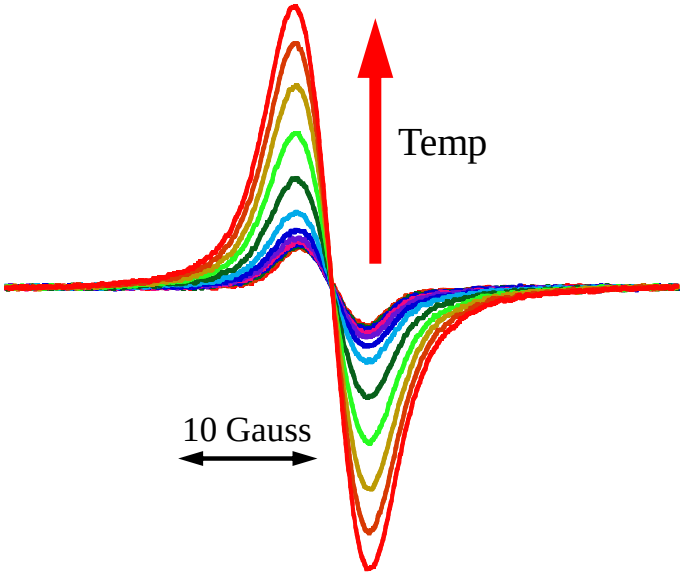

Figure 5-11. VT-EPR spectrum for **5** at 1 mM in CH_3CN collected at 10 K increments from 233 K to 343 K.

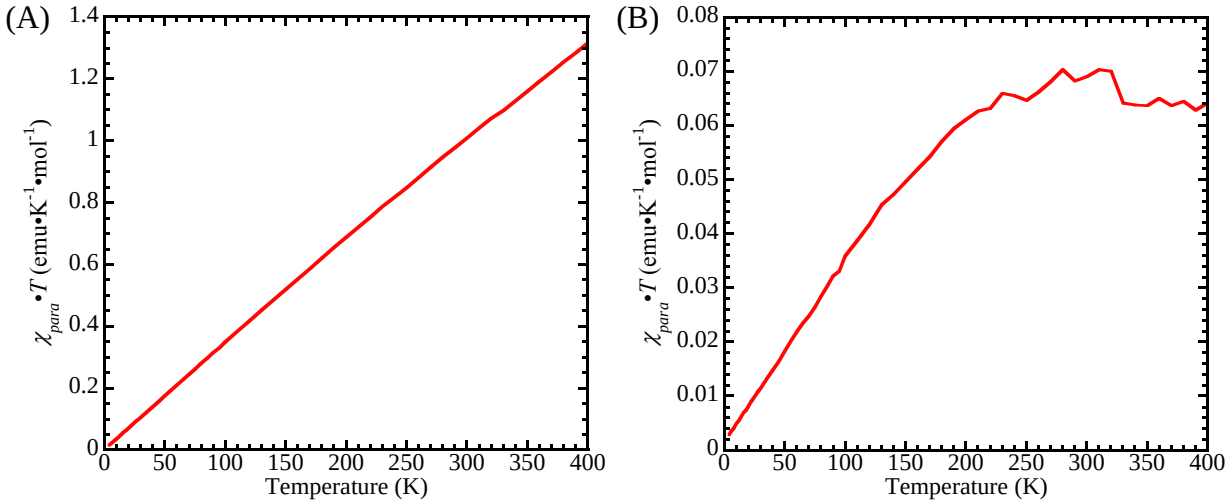

Figure 5-12. SQUID Magnetometry plotted as χ_{para}•T vs. T for a powder sample of **5**. (A) Uncorrected χ_{para}•T values obtained, positive slope component suggests large χ_{TIP} component; (B) Corrected χ_{para}•T values, following subtraction of a straight line.

Given that the phendione ligand contains an *ortho*-quinone core, a semiquinone-type radical must be considered for the observed signal. The semiquinonate forms of both the free phendione ($pd^{\bullet-}$) and **5** (**5**$^{\bullet-}$) are known,[12] as well as several other semiquinonate-containing Ru-phendione complexes.[13, 14] The free ligand and N,N′-bound derivatives $pd^{\bullet-}$ and **5**$^{\bullet-}$ have

been studied through electrochemical generation, and both present narrow EPR signals, with well resolved hyperfine.[12] The O,O′-bound monomer and dimeric complexes (**6** and **7**) have also been reported, and are characterized by a broad featureless signalat ca. g = 2.015 with a total spectral width of ca. 500 G.[13, 14]

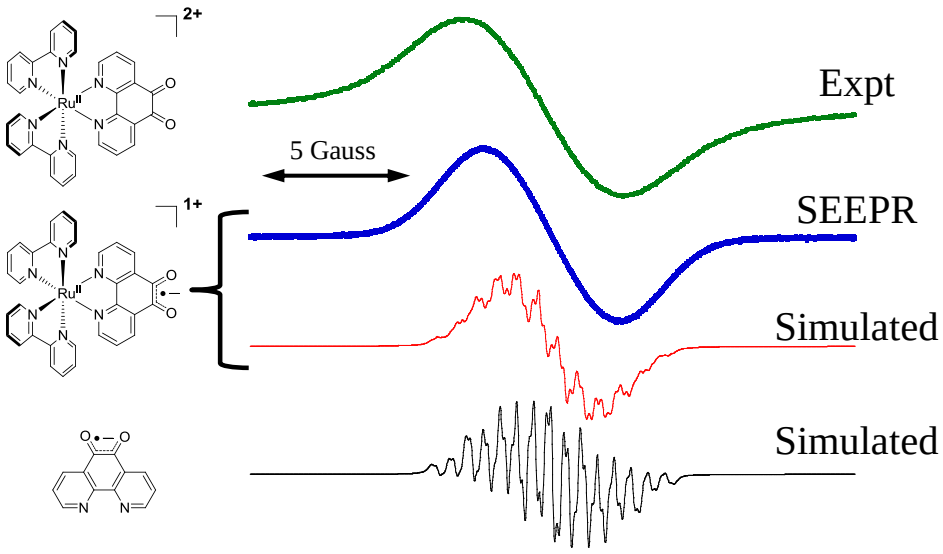

Figure 5-13. Simulated EPR spectra of **pd**$^{\bullet-}$ (black) **and 5**$^{\bullet-}$ (red) using reported hyperfine values,[12] with experimental spectra obtained for **5** (green) and **5**$^{\bullet-}$ (blue) at 5 G modulation included for comparison.

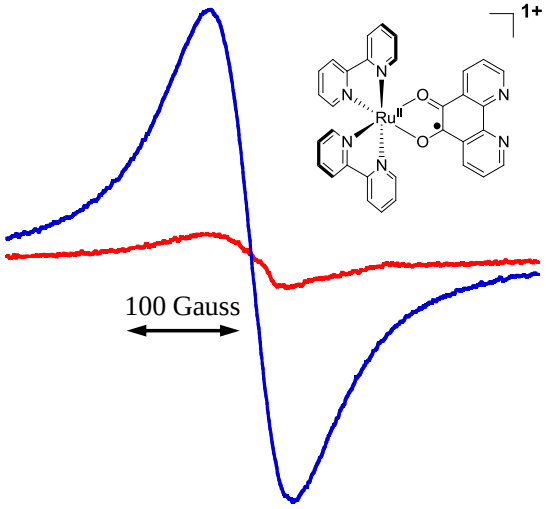

Figure 5-14. Fluid solution EPR spectra of **6** in anhydrous CH_3CN at 1 mM (red) and 10 mM (blue). Note the *increase* in EPR signal intensity with concentration, expected for a doublet, contrary to the observed *decrease* in intensity observed with **5**.

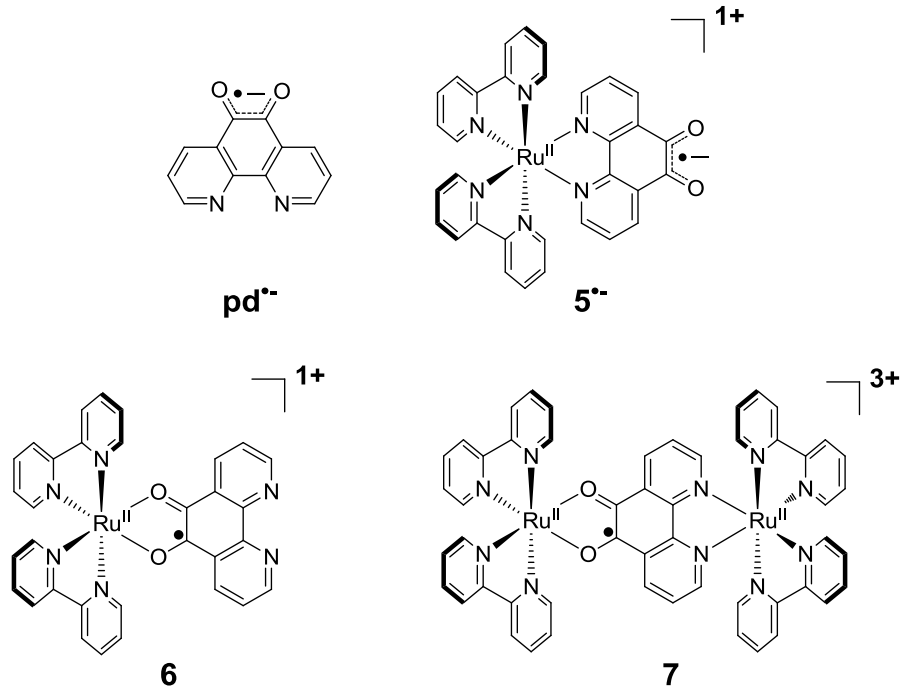

Figure 5-15. Structures of paramagnetic species considered but ruled out.

5.2.4 Optical Spectroscopy

The electronic absorption and infrared spectra for **5** and **6** were collected for comparison. Figure 5 shows the electronic absorption spectra for **5** and **6**, where **6** is dominated by a band at 950 nm, attributed to a $d(\pi_{Ru}) \rightarrow \pi^*(sq_{SOMO})$ MLCT (expanded views provided in Supporting Figure 9).[13-18] This band is virtually absent in **5**, which is dominated by the typical $d(\pi_{Ru}) \rightarrow \pi^*$(phendione) bpy-localized MLCT band at ca. 435 nm.[3] A key point here is the absence of any significant absorption in **5** at 950 nm, suggesting there are no semiquinone-containing species present. A similar result was obtained for **5** in DMSO solution.

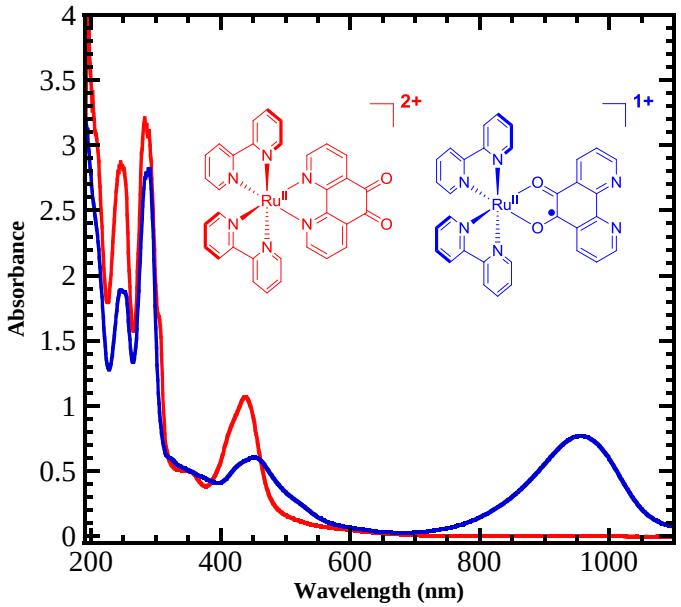

Figure 5-16. Electronic Absorption spectra for **5** (red) and **6** (blue) in acetonitrile.

Infrared spectra for solid samples of both **5** and **6** were also obtained for comparison (Figure 5-17). The IR spectrum of **5** is dominated by the C=O absorption at ca. 1700 cm^{-1}, indicative of the dione moiety.[3, 19] The spectrum of **6** lacks this 1700 cm^{-1} band, and is rather dominated by a typical semiquinone stretch at ca. 1430 cm^{-1}.[13, 14, 17, 18]

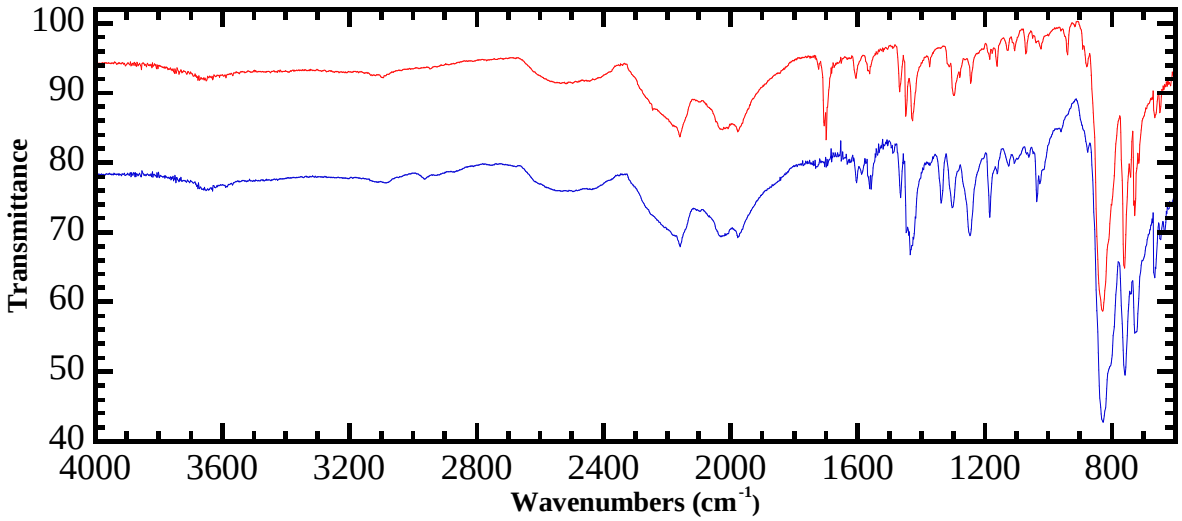

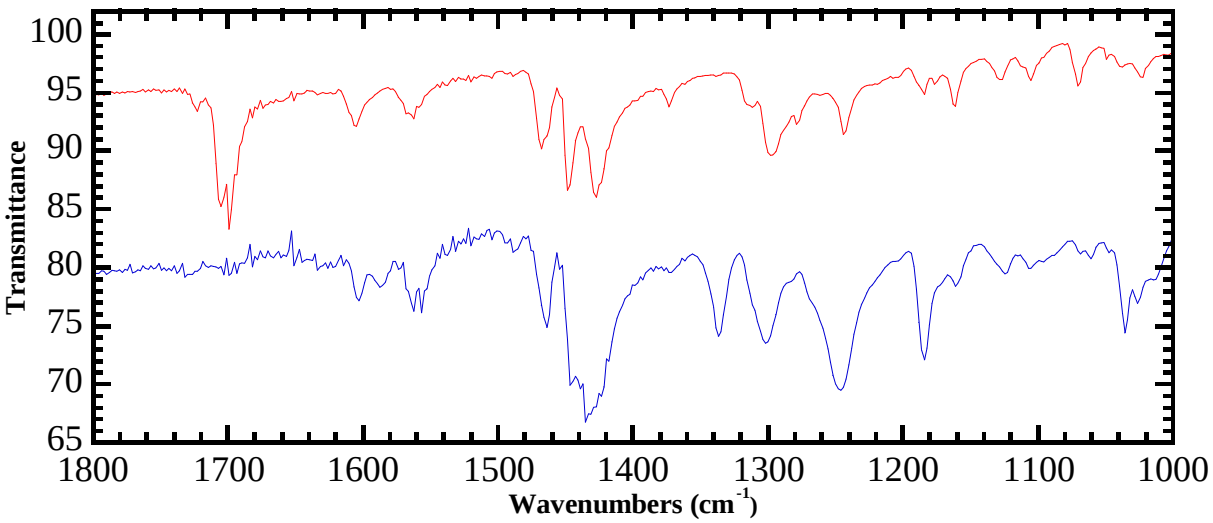

Figure 5-17. Infrared spectra for solid samples of **5** (red) and **6** (blue). (Top) Full spectral region, (B) Zoom 1800-1000 cm^{-1} region.

Based on the comparison of EPR, electronic absorption, and infrared spectra of **5** and **6**, it appears clear that an O,O′-bound semiquinonate structure is not responsible for the observed paramagnetic behavior. Additionally, the ^{1}H-NMR spectrum for **6** shows complete broadening of all of the resonances, expected for a radical species with a permanent magnetic moment.

The equilibrium **5↔5b** representing the dione-localized singlet-triplet states is consistent with the experimental observations, with DFT placing the energy gap at ca. 13,000 cm^{-1}. The effects observed on the ^{1}H-NMR suggest a minor paramagnetic contribution, likely not originating from a permanent doublet, and the primary broadening effect is localized to the phendione resonances with a minor shift in the remaining bpy proton resonances. The EPR experiments correlate with the onset of broadening in the NMR experiment, and are representative of an organic paramagnetic species. Both magnetic resonance techniques demonstrate a strong temperature dependence on the observed phenomena, suggestive of thermal population of a paramagnetic state, as well as inverse

concentration dependence, which could be due to spin lattice relaxation or triplet-triplet annihilation mechanisms. The presence of any O,O′-bound semiquinonate species has been ruled out through NMR, EPR, and optical spectroscopies, in not only the spectral appearance, but also the dependence on concentration and temperature. The observed paramagnetic character also appears to be directly related to metal coordination, which is consistent with the reliance on *N*-coordination in the phendione hydration chemistry (electron withdrawing character activates C=O bond for attack). These experimental observations suggest that a thermally accessible triplet, rather than a doublet impurity, is a reasonable source for the observed paramagnetic behaviors, which suggests the DFT results overestimate the singlet-triplet gap. In the **5b** form, the ring aromatizes, offering some degree of stabilization, but the typical S-T energy gap for an organic remains large. The presence of the Ru-center, however, offers a dense excited state manifold, through which spin-orbit coupling and configuration interaction can conspire to stabilize the phendione-triplet state.

5.3 Substituent effects on $[Ru^{II}(bpy)_2(phendione)]^{2+}$ paramagnetic behavior

Preliminary studies on a series of $[Ru^{II}(N\text{-}N)_2(pd)]^{2+}$ complexes (N-N = 2,2′-bipyridine with electron donating or withdrawing substituents) show this paramagnetic behavior is not limited to **5**, but rather is a general phenomenon, dependent on the electronic structure of the ligand set. The bpy substituents have a large impact on the Ru III/II potential (a range of 360 mV) but only change the first phendione reduction potential by about 60 mV. This small change in the reduction potential of phendione is a result of the extent of back-bonding based on the electron density at the Ru center.

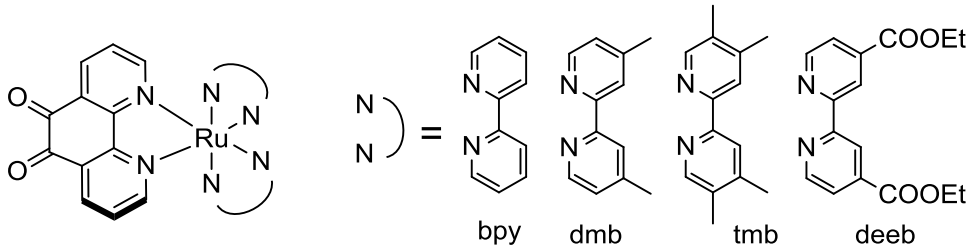

Figure 5-18. Structure of $[Ru^{II}(N\text{-}N)_2(pd)]^{2+}$ complexes.

Table 5-1. Redox potentials of $[Ru^{II}(N\text{-}N)_2(pd)]^{2+}$ vs Ag/Ag^+ in 0.1M TBAH in MeCN.

N-N	Ru III/II	$pd/pd^{\cdot-}$
tmb	0.948	-0.461
dmb	1.015	-0.453
bpy	1.110	-0.440
deeb	1.305	-0.400

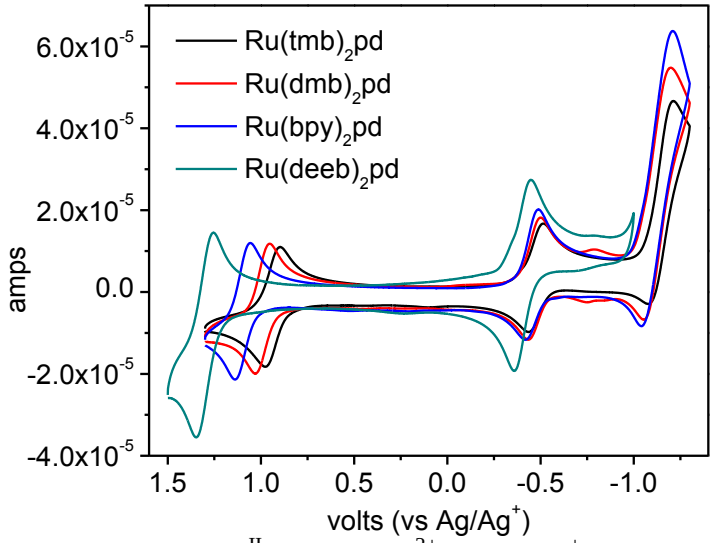

Figure 5-19. Cyclic voltametry of $[Ru^{II}(N\text{-}N)_2(pd)]^{2+}$ vs Ag/Ag^+ in 0.1M TBAH in MeCN. The solution was insufficiently degassed to observe reversible ligand reductions past the first pd reduction.

Paramagnetic behavior was observed in all of the $[Ru^{II}(N\text{-}N)_2(pd)]^{2+}$ complexes shown in Figure 5-18 to various degrees. The complexes with electron donating ligands, tmb and dmb, show an observable but weak signal compared to the parent compound. The incorporation of an electron withdrawning ligand, deeb, led to an increase in the paramagnetic signal. This may be a result of enhanced configuration interactions as the

excited state energy decreases and has more mixing with the ligand based triplet. These electronic effects will be more closely examined in future work.

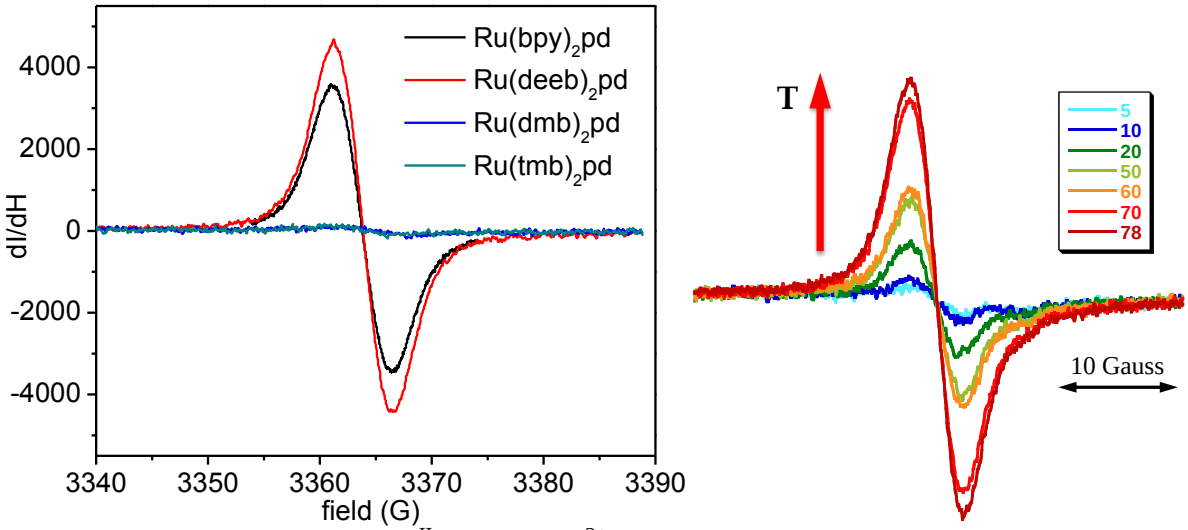

Figure 5-20. EPR spectra of $[Ru^{II}(N\text{-}N)_2(pd)]^{2+}$ complexes at a 1mM concentration in MeCN. VT-EPR spectrum for $Ru(deeb)_2pd$ at 1 mM in MeCN from 5°C to 78°C.

5.4 Concluding Remarks

A detailed experimental investigation into the paramagnetic behavior of **5** supports the presence of a thermally-accessible paramagnetic species, **5b**. The presence of this species may force reevaluation of the quenching mechanisms observed in a wider class of ruthenium polypyridal complexes, which may lead to a greater insight into the function of many of these complexes as luminescent sensors and catalysts. Additionally, the ability to control spin-state with mild stimuli such as solvent or temperature may allow for the use of related compound in spintronic applications.

5.5 Experimental Section

[$Ru^{II}(bpy)_2(pd)](PF_6)_2$ and **[**$Ru^{II}(bpy)_2(O,O'\text{-}pd)](PF_6)$ were prepared according to reported methods.[3, 13] All solvents were obtained from Fisher and used as received, unless noted otherwise.

Ru^{II}(4,4'dimethylbpy)$_2$Cl$_2$. Ru^{II}(4,4'dimethylbpy)$_2Cl_2$ was prepared by the reaction of 2 equivalents of 4,4'dimethylbpy (658 mg, 3.57 mmol) with Ru(cyclo-octadiene)Cl_2 polymer (500 mg, 1.78 mmol) in 20 mL of argon degassed *o*-dichlorobenzene for two hours at 160 °C. After cooling to room temperature, the solution was precipitated by the addition of ether; the solid was filtered and washed with ether. Yield: 897 mg (93%).

[Ru^{II}(4,4'dimethylbpy)$_2$(pd)](PF$_6$)$_2$. [Ru^{II}(4,4'dimethylbpy)$_2$(pd)](PF$_6$)$_2$ was prepared by reacting Ru^{II}(4,4'dimethylbpy)$_2Cl_2$ (200 mg, 0.37 mmol) with 1.2 equivalents of phendione (93.6 mg, 0.44 mmol) in thoroughly degassed 1:1 water:ethanol at reflux overnight. If the solvent is not degassed the reaction gives multiple products. Yield: 313 mg (87%).

[Ru^{II}(4,4',5,5'tetramethylbpy)$_2$(pd)](PF$_6$)$_2$.

[Ru^{II}(4,4',5,5'tetramethylbpy)$_2$(pd)](PF$_6$)$_2$ was prepared in the same manner as [Ru^{II}(4,4'dimethylbpy)$_2$(pd)](PF$_6$)$_2$ with similar yield. The ligand 4,4',5,5'tetramethylbpy was available from previous studies within the lab.

[Ru^{II}(4,4'COOEtbpy)$_2$(pd)](PF$_6$)$_2$. [Ru^{II}(4,4'COOEtbpy)$_2$(pd)](PF$_6$)$_2$ was prepared in the same manner as [Ru^{II}(4,4'dimethylbpy)$_2$(pd)](PF$_6$)$_2$ with similar yield. The ligand 4,4'COOEtbpy was made according to literature procedure.[20]

Photophysics. Steady-state and time-resolved emission experiments were performed on an Edinburgh FLSP920 spectrometer in quartz cuvettes. The TCSPC measurements were collected using an EPL-445 laser with sub-100 ps pulse width.

DFT Calculations. Theoretical calculations were carried out by using density functional theory as implemented in Gaussian09, revision A.02.[21] Becke's three-parameter hybrid functional[22-25] with the LYP correlation functional[26] (B3LYP) was used. For Ru, the

LANL2 relativistic effective core potential and associated uncontracted basis set was used, in combination with the 6-31 g* basis for the ligands (C, N, O, and H).

NMR Spectroscopy. ^{1}H NMR spectra were recorded on a Bruker Ultrashield 600 Plus NMR spectrometer at 600.13 MHz and referenced to the residual solvent proton resonance of water (δ 4.79 ppm) or acetonitrile (δ 1.94 ppm). Variable Temperature ^{1}H-NMR spectra were recorded on a Bruker 500 NMR spectrometer at 500.13 MHz and referenced to the residual solvent resonance of acetonitrile (δ 1.94 ppm).

Electron Paramagnetic Resonance Spectroscopy. All EPR spectra were recorded at X-band at room temperature (unless noted otherwise) on a JEOL FA-100 continuous-wave spectrometer. Powder spectra were recorded at room temperature on solid samples in quartz sample tubes. Fluid samples were collected on anhydrous CH_3CN solutions (0.01 mM – 5 mM) in ca. 1.6 mm OD capillary tubes. Dilutions were prepared from a common 5 mM stock; wet samples were prepared by adding DI water.

Magnetometry. Magnetic susceptibilities were measured on a Quantum Design MPMS-XL7 SQUID Magnetometer using an applied field of 0.1 T for Curie plots. Microcrystalline samples (ca. 35mg) were loaded into gelcap/straw sample holders and mounted to the sample rod with Kapton tape. Data from the gelcap samples were corrected for the sample container and molecular diamagnetism using Pascal's constants as a first approximation.

5.6 References

1. McMasters, D. R.; Wirz, J., Spectroscopy and Reactivity of Kekulé Hydrocarbons with Very Small Singlet−Triplet Gaps. *J. Am. Chem. Soc.* 2000, 123, 238-246.

2. Zhu, X.; Tsuji, H.; Nakabayashi, K.; Ohkoshi, S.-i.; Nakamura, E., Air- and Heat-Stable Planar Tri-p-quinodimethane with Distinct Biradical Characteristics. *J. Am. Chem. Soc.* 2011, 133, 16342-16345.

3. Goss, C. A.; Abruna, H. D., Spectral, electrochemical and electrocatalytic properties of 1,10-phenanthroline-5,6-dione complexes of transition metals. *Inorg. Chem.* 1985, 24, 4263-4267.

4. Sun, Y.; Collins, S. N.; Joyce, L. E.; Turro, C., Unusual Photophysical Properties of a Ruthenium(II) Complex Related to [Ru(bpy)2(dppz)]2+. *Inorg. Chem.* 2010, 49, 4257-4262.

5. Sun, Y.; Lutterman, D. A.; Turro, C., Role of Electronic Structure on DNA Light-Switch Behavior of Ru(II) Intercalators. *Inorg. Chem.* 2008, 47, 6427-6434.

6. Concepcion, J. J.; Brennaman, M. K.; Deyton, J. R.; Lebedeva, N. V.; Forbes, M. D. E.; Papanikolas, J. M.; Meyer, T. J., Excited-State Quenching by Proton-Coupled Electron Transfer. *J. Am. Chem. Soc.* 2007, 129, 6968-6969.

7. Lebedeva, N. V.; Schmidt, R. D.; Concepcion, J. J.; Brennaman, M. K.; Stanton, I. N.; Therien, M. J.; Meyer, T. J.; Forbes, M. D. E., Structural and pH Dependence of Excited State PCET Reactions Involving Reductive Quenching of the MLCT Excited State of [RuII(bpy)2(bpz)]2+ by Hydroquinones. *J. Phys. Chem. A* 2011, 115, 3346-3356.

8. Kober, E. M.; Caspar, J. V.; Lumpkin, R. S.; Meyer, T. J., Application of the energy gap law to excited-state decay of osmium(II)-polypyridine complexes: calculation of relative nonradiative decay rates from emission spectral profiles. *J. Phys. Chem.* 1986, 90, 3722-3734.

9. Lei, Y.; Anson, F. C., Hydration of the Carbonyl Groups in 1,10-Phenanthroline-5,6-dione Induced by Binding Protons or Metal Cations to the Pyridine Nitrogen Sites. *J. Am. Chem. Soc.* 1995, 117, 9849-9854.

10. Lei, Y.; Shi, C.; Anson, F. C., Effects of Coordination to Transition Metals on the Hydration and Electroactivity of the Chelating Ligand 1,10-Phenanthroline-5,6-dione. *Inorg. Chem.* 1996, 35, 3044-3049.

11. Fujihara, T.; Wada, T.; Tanaka, K., Acid-base equilibria of various oxidation states of aqua-ruthenium complexes with 1,10-phenanthroline-5,6-dione in aqueous media. *Dalton Trans.* 2004, 645-652.

12. Murphy, D. M.; McNamara, K.; Richardson, P.; Sanchez-Romaguera, V.; Winpenny, R. E. P.; Yellowlees, L. J., Electrochemical and spectroelectrochemical studies of complexes of 1,10-phenanthroline-5,6-dione. *Inorg. Chim. Acta* 2011, 374, 435-441.

13. Shukla, A. D.; Das, A., Redox responsive binuclear complexes using 5,6-dihydroxy-1,10-phenanthroline as a bridging ligand: synthesis, characterization and physicochemical studies. *Polyhedron* 2000, 19, 2605-2611.

14. Ghosh, T.; Maiya, B.; Samanta, A.; Shukla, A.; Jose, D.; Kumar, D.; Das, A., Mixed-ligand complexes of ruthenium(II) containing new photoactive or electroactive ligands: synthesis, spectral characterization and DNA interactions. *J. Biol. Inorg. Chem.* 2005, 10, 496-508.

15. Haga, M.; Dodsworth, E. S.; Lever, A. B. P., Catechol-quinone redox series involving bis(bipyridine)ruthenium(II) and tetrakis(pyridine)ruthenium(II). *Inorg. Chem.* 1986, 25, 447-453.

16. Lever, A. B. P.; Auburn, P. R.; Dodsworth, E. S.; Haga, M. A.; Liu, W.; Melnik, M.; Nevin, W. A., Bis(dioxolene)(bipyridine)ruthenium redox series. *J. Am. Chem. Soc.* 1988, 110, 8076-8084.

17. Bhattacharya, S.; Pierpont, C. G., Charge distribution in bis(quinone) complexes of ruthenium and osmium. Structural, spectral, and electrochemical properties of the Os(bpy)(Cat)2 (Cat = catecholate, 3,5-di-tert-butylcatecholate, tetrachlorocatecholate) series. *Inorg. Chem.* 1992, 31, 35-39.

18. Bhattacharya, S.; Pierpont, C. G., Structure and bonding in bis(quinone) complexes of ruthenium. Synthesis and characterization of the Ru(PPh3)2(SQ)2 (SQ = 3,5-tert-butylsemiquinone, tetrachloro-1,2-semiquinone) series. *Inorg. Chem.* 1991, 30, 1511-1516.

19. Boghaei, D. M.; Behzadian Asl, F., Synthesis, characterization and fluorescence spectra of mixed ligand Zn(II), Cd(II) and Hg(II) complexes with 1,10-phenanthroline-5,6-dione ligand. *J. Coord. Chem.* 2007, 60, 1629-1635.

20. Hoertz, P. G.; Staniszewski, A.; Marton, A.; Higgins, G. T.; Incarvito, C. D.; Rheingold, A. L.; Meyer, G. J., Toward exceeding the Shockley-Queisser limit:

Photoinduced interfacial charge transfer processes that store energy in excess of the equilibrated excited state. *Journal of the American Chemical Society* 2006, 128, 8234-8245.

21. M. J. Frisch, G. W. Trucks, H. B. Schlegel, G. E. Scuseria, M. A. Robb, J. R. Cheeseman, G. Scalmani, V. Barone, B. Mennucci, G. A. Petersson, H. Nakatsuji, M. Caricato, X. Li, H. P. Hratchian, A. F. Izmaylov, J. Bloino, G. Zheng, J. L. Sonnenberg, M. Hada, M. Ehara, K. Toyota, R. Fukuda, J. Hasegawa, M. Ishida, T. Nakajima, Y. Honda, O. Kitao, H. Nakai, T. Vreven, J. A. Montgomery, Jr., J. E. Peralta, F. Ogliaro, M. Bearpark, J. J. Heyd, E. Brothers, K. N. Kudin, V. N. Staroverov, R. Kobayashi, J. Normand, K. Raghavachari, A. Rendell, J. C. Burant, S. S. Iyengar, J. Tomasi, M. Cossi, N. Rega, J. M. Millam, M. Klene, J. E. Knox, J. B. Cross, V. Bakken, C. Adamo, J. Jaramillo, R. Gomperts, R. E. Stratmann, O. Yazyev, A. J. Austin, R. Cammi, C. Pomelli, J. W. Ochterski, R. L. Martin, K. Morokuma, V. G. Zakrzewski, G. A. Voth, P. Salvador, J. J. Dannenberg, S. Dapprich, A. D. Daniels, O. Farkas, J. B. Foresman, J. V. Ortiz, J. Cioslowski, and D. J. Fox, Gaussian, Inc., Wallingford CT, 2009.

22. Becke, A. D., Density-functional exchange-energy approximation with correct asymptotic behavior. *Phys. Rev. A Gen. Phys.* 1988, 38, 3098-100.

23. Becke, A. D., A new mixing of Hartree-Fock and local-density-functional theories. *J. Chem. Phys.* 1993, 98, 1372-7.

24. Becke, A. D., Density-functional thermochemistry. III. The role of exact exchange. *J. Chem. Phys.* 1993, 98, 5648-52.

25. Stephens, P. J.; Devlin, F. J.; Chabalowski, C. F.; Frisch, M. J., AB-INITIO CALCULATION OF VIBRATIONAL ABSORPTION AND CIRCULAR-DICHROISM SPECTRA USING DENSITY-FUNCTIONAL FORCE-FIELDS. *Journal of Physical Chemistry* 1994, 98, 11623-11627.

26. Lee, C.; Yang, W.; Parr, R. G., Development of the Colle-Salvetti correlation-energy formula into a functional of the electron density. *Phys. Rev. B Condens. Matter* 1988, 37, 785-9.